UNIVERSITY OF CALIFORNIA SAN DIEGO

Systems Analysis of Mechano-Sensitive Signaling Networks Regulating Gene Expression in Cardiomyocytes and Adventitial Fibroblasts

A dissertation submitted in partial satisfaction of the requirements for the degree

Doctor of Philosophy

in

Bioengineering

by

Shulin Cao

Committee in charge:

Professor Andrew McCulloch, Chair
Professor Kevin King
Professor Stephan Lange
Professor Jeffrey Omens
Professor Armin Schwartzman
Professor Daniela Valdez-Jasso

2021

The dissertation of Shulin Cao is approved, and it is acceptable in quality and form for publication on microfilm and electronically.

University of California San Diego

2021

DEDICATION

I dedicate this work to my parents, especially my mother, who have shown tireless love and support through my entire life and taught me to be grateful.

I also dedicate this work to Toby Chen for the constructive suggestions on many decisive moments in the last 5 years, which has been a significant part of my way to success.

TABLE OF CONTENTS

LIST OF ABBREVIATIONS

ECM	Extracellular matrix
RT-PCR	Quantitative reverse transcription polymerase chain reaction
AngII	Angiotensin II
AT1R	AngII type 1 receptor
TRP	Transient receptor potential
LV	Left ventricular
PAH	Pulmonary arterial hypertension
PAAF	Pulmonary artery adventitial fibroblast
ET1	Endothelin 1
ET1R	Endothelin 1 receptor
Gp130	Glycoprotein 130
LTCC	Left-type calcium channel
NHE	Sodium hydrogen exchanger
MuRF1	Muscle ring-finger protein 1
MuRF2	Muscle ring-finger protein 2
MLP	Muscle LIM protein
FHL1	Four-and-a-half LIM domains 1
RhoGEF	Rho guanine nucleotide exchange factor
RhoA	Ras homolog family member A
TF	Transcription factor
ROCK	Rho-associated protein kinase
MRTF	Myocardin-related transcription factor

FAK	Focal adhesion kinase
PI3K	Phosphatidylinositol 3 kinase
Akt	Protein kinase B
PDK1	Phosphoinositide-dependent kinase-1
NO	Nitric oxide
NOS	Nitric oxide synthase
PKG	cGMP-dependent protein kinase
mTOR	mammalian target of rapamycin
GSK3B	Glycogen synthase kinase-3 beta
IKB	Inhibitor of kappa B
eIF4E	eukaryotic translation initiation factor 4E
JAK	Janus kinase 1 or 2
STAT	Signal transducers and activators of transcription
MAPK	Mitogen-activated protein kinase
MEK	Mitogen-activated protein kinase kinase
MEKK	Mitogen-activated protein kinase kinase kinase
ERK1/2	Extracellular signal-regulated kinase 1/2
ERK5	Extracellular signal-regulated kinase 5
JNK	c-Jun N-terminal kinase
TAC	Transverse aortic Constriction
CAMK	Calmodulin dependent protein kinase
PKC	Protein kinase C
CaN	Calcineurin

DAG	Diacylglycerol
TGFβ	Transforming growth factor β 1
PDGF	Platelet derived growth factor
FGF	Fibroblast growth factor
TNFα	Tissue necrosis factor α
NFAT	Nuclear factor of activated T-cells
TIMP	Tissue inhibitor of metalloproteinase 1
SMAD	Small mother against decapentaplegic
KO	Knockout
NFκB	Nuclear factor kappa-light-chain-enhancer of activated B cells
MMP	Metalloproteinase
MST	Macrophage stimulating
miRNA	micro RNA
OCT4	Octamer binding transcription factor 4
YAP/TAZ	Yes associated protein/Tafazzin
PPAR	Peroxisome proliferator activated receptor
LRP8	LDL receptor related protein 8
αSMA	α smooth muscle actin
HIF1α	Hypoxia-inducible factor 1α
HERP	Homocysteine-responsive endoplasmic reticulum-resident
MSN	Mechanosignaling network
IKK	Inhibitor of kappa B kinase
MEF2	Myocyte enhancer factor 2

SRF	Serum response factor
HDAC	Histone deacetylase
CREB	Cyclic adenosine monophosphate response element-binding
cJun	Proto-oncogene c-Jun
cFos	Proto-oncogene c-Fos
cMyc	Proto-oncogene c-Myc
GATA4	GATA-binding protein 4
FoxO	Forkhead box O
ChIP	Chromatin immunoprecipitation
TFBS	TF binding site
DE	Differentially Expressed
CPM	Counts per million reads
TPM	Transcripts per million reads
RPKM	Reads per kilobase of exon per million reads mapped
FPKM	Fragments per kilobase of exon per million fragments mapped
ODE	Ordinary differential equations
UQ	Uncertainty Quantification
EC_{50}	Half-maximal effective concentration
MC	Monte Carlo
PCE	Polynomial chaos expansions
MCMC	Markov-Chain Monte Carlo
K-S	Kolmogorov-Smirnov
NC	No change
SC	Significant changed

BNP	Brain natriuretic peptide
β-MHC	β-myosin heavy chain
Cx43	Connexin 43
PrSynth	Protein synthesis
sACT	skeletal alpha actin
ANP	Atrial natriuretic protein
IP3	Inositol triphosphate
Ao	Angiotensinogen
FC	Fold change
KEGG	Kyoto Encyclopedia of Genes and Genomes
clOPN	cleaved osteopontin
ROS	reactive oxygen species
NICD	notch intracellular domain
Nox4	NADPH oxidase 4
ASK1	Apoptosis signal related kinase 1
TAK1	TGF- β –activated kinase
Eln	Elastin mRNA
Col1a1	Collagen I mRNA
Col3a1	Collagen III mRNA
Fn1	Fibronectin mRNA
Loxl1	Lysyl oxidase mRNA
Acta	αSMA mRNA
OT	Oxytocin

Rap	The Ras related GTPase
HSF	Heat Shock Factor

LIST OF SUPPLEMENTAL FILES

LIST OF FIGURES

LIST OF TABLES

ACKNOWLEDGEMENTS

First, I would like to acknowledge my advisor Dr. Andrew D. McCulloch as the chair of my committee. I appreciate him for providing me such a great platform to do research and guiding me towards an important project of human health. His constant support and encouragement, together with the insightful advice and independence he teaches me, have been a fundamental source of my perseverance to become an independent researcher.

I am also very grateful to Dr. Jeffrey H. Omens and Dr Daniela Valdez-Jasso for their continuous constructive suggestions in the academic projects I have been working and encouragement in keeping moving during this journey. I would like to thank Dr. Jeffrey J. Saucerman, Dr. Yasser Aboelkassam, Dr. Alexander C. Zambon, Dr. Philip Tan, and Dr. Kyle S. Buchholz for their instructions and suggestions during the collaborations.

Through the entire journey, I really appreciate all the help and support by my lab manager Jennifer C. Stowe and my lab mate Ariel Wang. Their expertise in experiments have been a significant part in this dissertation work. Besides, their kindness and continuous support have inspired me to be confident researcher. I would also like to thank the lab alumni and current lab mates, Dr. Kevin Vincent, Dr. Kim McCabe, Dr. Nick Forsch, Dr. Joseph Powers, Dr. Xiaoyan Zhang, Will Valdez, Ariel Wang, Sachin Govil, Abigail Teigen, and Marcus Hock, who have been providing support for me and making the lab a warm place.

I also want to express my gratitude to my friends, Dr. Yuhan Ling, Dr. Zhongqi Jia, Dr. Yanju Yang, Toby Chen, Chuqing Zhou, Zijue Wu, Junyi Jiang, Xingrong Wu, Erica Pursell, Haoting Chen, Tan Wang for their constant support on every important moment and the good memories of my life in the States.

Last but not the least, I would like to thank my parents and family, for their continuous love and care in my life. They teach me to be brave whenever I'm in difficulty and grateful for everything that I have.

Chapter 2, in full, is a reprint of the material as it appears in Philosophical Transactions of the Royal Society A 2020. Cao, Shulin; Aboelkassam, Yasser; Wang, Ariel; Valdez-Jasso, Daniela; Saucerman, Jeffery J.; Omens, Jeffery H. McCulloch, Andrew D. The dissertation author was the primary investigator and author of this paper.

Chapter 3, in part, is currently being prepared for submission for publication of the material. Cao, Shulin; Buchholz, Kyle S.; Tan, Philip; Stowe, Jennifer C.; Aboelkassam, Yasser; Wang, Ariel; Zambon, Alexander C.; Saucerman Jeffery J.; Omens, Jeffery H.; McCulloch, Andrew D. Reprinted with permission from all co-authors. The dissertation author was a primary investigator and author of this material.

Chapter 4, in full, is a reprint of the materials as it appears in the following publications: Philosophical Transactions of the Royal Society A 2020. Wang, Ariel; Cao, Shulin; Aboelkassam Yasser; Valdez-Jasso Daniela, Cells 2021. Wang, Ariel; Cao, Shulin; Stowe Jennifer C.; Valdez-Jasso Daniela. The dissertation author was the second author of these papers and developed all methodology and computational analysis.

VITA

2015 Bachelor of Science, Huazhong University of Science and Technology

2016-2017 Teaching Assistant, University of California San Diego

2021 Doctor of Philosophy, University of California San Diego

PUBLICATIONS

Wang, A., **Cao, S.**, Stowe, J.C. and Valdez-Jasso, D., 2021. Substrate Stiffness and Stretch Regulate Profibrotic Mechanosignaling in Pulmonary Arterial Adventitial Fibroblasts. Cells, 10(5), p.1000.

Cao, S., Aboelkassem, Y., Wang, A., Valdez-Jasso, D., Saucerman, J. J., Omens, J. H., & McCulloch, A. D. (2020). Quantification of model and data uncertainty in a network analysis of cardiac myocyte mechanosignalling. Philosophical Transactions of the Royal Society A, 378(2173), 20190336.

Wang, A., **Cao, S.**, Aboelkassem, Y., & Valdez-Jasso, D. (2020). Quantification of uncertainty in a new network model of pulmonary arterial adventitial fibroblast pro-fibrotic signalling. Philosophical Transactions of the Royal Society A, 378(2173), 20190338.

Cao S, Buchholz KS, Tan P, Stowe JC, Aboelkassem Y, Wang A, Zambon AC, Saucerman JJ, Omens JH, McCulloch AD. "Fiber and Transverse Stretch Mediate Differential Transcriptional Responses in Mouse Neonatal Ventricular Myocytes". *(In preparation).*

FIELDS OF STUDY

Major Field: Engineering

Studies in Bioengineering with a Specialization in Computational Biology and Bioinformatics

ABSTRACT OF THE DISSERTATION

Systems Analysis of Mechano-Sensitive Signaling Networks Regulating Gene Expression in Cardiomyocytes and Adventitial Fibroblasts

by

Shulin Cao

Doctor of Philosophy in Bioengineering

University of California San Diego, 2021

Professor Andrew McCulloch, Chair

Cells such as myocytes and adventitial fibroblasts are responsive to mechanical cues in their local environment. In response to mechanical loads, a variety of mechano-transduction mechanisms and signaling pathways are activated to regulate their response to the altered conditions.

In order to define mechano-signaling networks and their role in cellular function and remodeling, we have adapted and refined previously published systems models of myocyte

hypertrophy. Using uncertainty quantification, we first found that the model accuracy was robust to parameter changes over a wide range with model outputs being least sensitive to time constants and most affected by uncertainty in reaction weights. We also found epistemic uncertainty in the reaction logic of the model could greatly affect model accuracy while uncertainty in the validation data had a modest effect on model accuracy.

As a step forward toward understanding myocyte response to external loading, including direction-dependent pathways, we extended this previous network model to include the transcriptional regulatory networks controlling gene expression as well as protein translation, and introduce a mass-action method to model quantitative gene expression. By incorporating RNA-sequencing data, this new approach displayed high accuracy with 69% agreement overall and 72% agreement for predicted differentially expressed genes in response to longitudinal stretch. We further found that the difference between transverse and longitudinal stretch responses in cardiomyocytes could be related to the sensitivity of directional mechanotransduction, with the sensitivity of longitudinal stretch being greater than transverse. Upon analyzing genes regulated by multiple TFs, we found that expression of these genes didn't monotonically change with the number of TFs, which indicates TF regulation effects may saturate faster when multiple TFs coregulate gene expression. Moreover, we identified AT1 and ET1 receptors as main regulators of the stretch induced responses through receptor inhibition simulations and subsequent experiments.

A similar approach was used to study mechanical signaling and remodeling responses in PAAFs. In the current work, we have modified an existing systems model of cardiac fibroblast signaling to PAAFs and the cellular regulation of profibrotic signaling by combining both in-vitro and in-silico models of cell signaling in response to altered mechanical conditions. A UQ analysis on this model highlighted parameters to be optimized and network modules to be elucidated with

more experiments. The signaling model in PAAFs and the subsequent experiments identified that both stretch and increased substrate stiffness regulated profibrotic genes, while no interaction effect was found between stretch and stiffness for several key genes studied. In addition, the activation of fibronectin expression by stretch in PAAFs may be angiotensin-independent when the cells are adhered on stiff but not soft substrates.

While these signaling network models can help distinguish regulators and their sensitivity to different mechanical stimuli, it is not known how these regulators participate in gene regulation of in-vivo hypertrophy. In the future, these signaling network models can be used to identify key regulators of hypertrophy-related heart failure and tissue fibrosis and provide support for drug discovery.

Chapter 1: Introduction

1.1. Mechanotransduction in Cardiomyocytes and Adventitial Fibroblasts

Many heart diseases, including hypertrophic cardiomyopathy, are associated with cardiac hypertrophy [1]. Cardiac hypertrophy is the enlargement or thickening of the heart muscle, and in many cases, hemodynamic overload on the heart can induce different modes of ventricular hypertrophy and remodeling. Physiological hypertrophy, often a result of exercise, is an adaptive response to hemodynamic loading [2, 3]. This compensatory hypertrophic growth of the heart enhances cardiac performance and may diminish ventricular wall stress and oxygen consumption [3]. In many cases, prolonged hemodynamic overloads on the heart are pathologic, with a long-term response that is maladaptive and can result in pathological hypertrophy, characterized by maladaptive geometric remodeling and fibrosis, which ultimately can lead to heart failure [3-5]. Remodeling of myocardium, whether physiologic or pathologic, is typically associated with phenotypic changes such as growth of the resident muscle cells of the heart, and the remodeling of the constituents of the extracellular matrix (ECM) that interconnect these cells [6]. Many of these phenotypic changes have been related to alterations in the mechanical environment of these cells in heart, or dysregulation of the sensing or response to altered mechanical loads.

A major component of ventricular remodeling is governed by the changes in cardiomyocytes, due to the overwhelming volumetric proportion in this cell population of the heart. These cells have well characterized responses to multiple mechanical stimuli including compressive and tensile stresses and strains in their surrounding environment [7-9]. Cellular responses, such as myocyte hypertrophy, are regulated by mechanotransduction, which converts mechanical signals from the outside of the cells via internal structures such as the membrane and

cytoskeleton of these cells, into biochemical responses via the activation of mechanosensitive signaling pathways [8-11]. These mechanical signals then propagate to the nucleus, where they can alter the activities of transcription factors and further induce transcriptional responses leading to changes in proteins and hence cellular remodeling.

Although the exact mechanisms are unknown, evidence suggests that mechanical signals in the myocardium and other tissues are perceived by the resident cells and transmitted through many transmembrane complexes including proteins connecting the ECM with the cytoskeleton, transmembrane receptors, and the ion channel receptors on the membrane surface [12-18]. The ECM is a key player in these mechanosensitive pathways, as it can transmit mechanical loads via its structural components such as collagen and elastin, to myocardial cells via transmembrane protein structures such as integrins [13-15]. Hence, mechanosensing and transduction are fundamental to the normal functioning of these cells in response to environmental changes, and defects in these sensing and signaling pathways are likely involved in pathophysiology [13-15].

In addition to force transmission to a cell, internal sensing and subsequent changes in gene expression, mechanical loading can also trigger autocrine and paracrine mechanisms via transmembrane receptors [16-17]. Angiotensin II (AngII) is a peptide hormone converted from Angiotensin I and its levels have been reported to be elevated by mechanical stretch [16]. The locally produced AngII has both autocrine and paracrine properties that further activates hypertrophy and matrix remodeling via the AngII type 1 receptor (AT1R) [16]. AngII has also been reported to stimulate protein synthesis in the ECM, and this accumulation of ECM increases myocardial stiffness and results in impaired contractile behavior [17].

Many mechano-regulated responses have also been reported to be associated with mechanoelectric feedback via regulation of the cross-membrane fluxes of ions such as calcium

[18-19]. These transmembrane currents can go through mechanosensitive channels such as transient receptor potential (TRP) in response to acute stretch [19-20].

In addition to mechanically-linked left ventricular (LV) diseases such as LV hypertrophy and LV hypertrophic cardiomyopathies, pulmonary arterial hypertension (PAH) is another common disease with implications in the right ventricle as well as remodeling in the pulmonary arteries themselves [21-22]. During the progression of PAH, the pulmonary arteries and veins undergo many structural alterations, commonly referred to as pulmonary vascular remodeling [23-24]. Pulmonary artery adventitial fibroblasts (PAAFs), the principal cell type in the adventitial layer, are important mediators of pulmonary vascular remodeling in response to mechanical stimuli [25-26]. Like cardiomyocytes, the response of these cells is also mediated by many mechanosensitive signaling pathways. In the following subsections, both mechanosensors and the associated signaling pathways in cardiomyocytes and PAAFs will be introduced in detail.

1.1.1. Mechanosensors and Associated Signaling Pathways in Cardiomyocytes

Cardiomyocytes sense mechanical stimuli by transmitting forces from their external environment to to mechanosensors that are likely located at the cell membrane or in internal structural components of the cytoskeleton. Various structural mechanisms have been proposed in the transmission and sensing of external forces, including structural proteins that bind to the ECM, transmembrane receptors, and the release of small molecules through autocrine or paracrine mechanisms, and ion channel receptors [12-19]. Some mechanosensors are thought to be located in the sarcolemma, the cell membrane of cardiomyocytes, which contains many structural protein complexes that connect ECM ligands with the cytoskeleton, including the integrin complex and the dystroglycan complex [13-15,27-28]. Integrins are heterodimeric cell-surface receptors with α and β subunits that link the ECM and the intracellular cytoskeleton and function as

mechanotransducers by binding to ECM proteins, including fibronectin, laminin, and collagen [13-15,29-30]. The main integrin heterodimers expressed in cardiomyocytes are $\alpha_5\beta_1$ and $\alpha_v\beta_3$, where the deletion of either βsubunits disrupt pressure-induced hypertrophic signaling [15]. The role of integrins in connection with laminin can be compensated by the dystroglycan complex, a glycoprotein that can attach to the actin cytoskeleton via dystrophin [27-28].

In addition to force transmitted via the cytoskeleton or other structural components of the myocyte, mechanical signals may be sensed directly by transmembrane receptors in response to altered molecular environment. The release of AngII and ET1 induced by mechanical stress can activate AT1R and ET1 receptor (ET1R), respectively [31-33]. AT1R was also found to be directly activated under mechanical stretch independent of AngII [31,33]. Similar to AT1R, gp130, a transmembrane protein, is a founding member of the class of many cytokine receptors [34-36]. Reduced compensatory hypertrophy was found in gp130-KO mice during pressure overload [36], possibly indicating a load sensing mechanism through this receptor.

Another pathway that may be involved in mechanotransduction in cardiomyocytes is the regulation of intracellular calcium, which has been reported to be elevated in cardiomyocytes in response to acute stretch [18-20]. Many mechanosensitive channels, such as the left-type calcium channel (LTCC) and TRP, can be activated through this process. Compared with LTCC and TRP which directly affect the calcium influx, sodium hydrogen exchanger (NHE) mediates calcium oscillation by adjusting the sodium concentration and pH of the extracellular environment [37].

In the following subsections, the signaling pathways following the activation of these mechanosensors will be introduced.

1.1.1.1. The Cytoskeleton-Related Complexes and the Associated Signaling Pathways

The myofibril is the major force-generating functional components of the cardiomyocyte [14,38-40]. It contains repeated contractile units, also known as sarcomeres, and is crucial to maintaining the normal function of cardiac muscles in response to mechanical loading [14,38-40]. The primary components that form the sarcomere are actin and myosin [14,40]. Myosin binding to actin can generate cross-bridge tension leading to the movement on the actin filament, which results in myofibrill contraction and force transmission [41-42]. Titin, also known as connectin, is a giant protein complex that connects the z-disc with the M-line of the sarcomere and is critical to contractile function of the cell [43-44]. Its interaction with actin promotes the stiffening of cardiac muscle [43]. Titin kinase couples the ubiquitin kinases Muscle Ring-Finger protein 1 (MuRF1) and MuRF2, which further coordinate myofibril trophicity [45]. Mechanosignaling may be regulated via the connection of titin with many cytoskeletal proteins, including the Muscle LIM Protein (MLP) and the four-and-a-half domains (FHL) [46-47]. These proteins then propagate the signals between myofibrils and the cytoskeleton to many downstream signaling pathways, which will be discussed later.

Integrins connect the actin cytoskeleton to the cell membrane via sub-membranous structures including the costamere, which contains proteins such as talin and vinculin [48-51]. Talin is a large dimeric cytoskeletal protein that activates the binding of integrin with actin [49]. Like talin, vinculin is one of the major cytoplasmic actin-binding proteins enriched in focal adhesions [50]. The binding of actin with integrin can be strengthened via the binding of talin to vinculin [49]. Similar to how integrin functions, the dystroglycan complex is a compensatory role to integrin that alternatively connects the cardiomyocyte cytoskeleton with laminin in the ECM via dystrophin [28]. As a result of force transmission via integrin or dystroglycan to the

cytoskeleton, Rho guanine nucleotide exchange factor (RhoGEF) is activated and recruited to the adhesion complex [52]. This further stimulates RhoA, a small GTPase protein, and its binding to Rho-associated protein kinase (ROCK), which prevents actin depolymerization and the normal function of titin [53-57]. RhoA also mediates nuclear translocation of myocardin-related transcription factor (MRTF), which usually acts as a coactivator of many TFs [58]. Rapid phosphorylation of the focal adhesion kinase (FAK) can be induced by the activation of β(1D)-integrin by α(1)-adrenergic stimulation, which then alters the Src binding and stimulates the signaling cascade of phosphatidylinositol 3 kinase (PI3K) [59-60]. PI3Ks are heterodimeric enzymes consisting of an adapter regulatory subunit and a catalytic subunit tightly bound to the regulatory subunit [61]. Activated PI3K can phosphorylate and activate protein kinase B (also known as Akt) by recruiting phosphoinositide-dependent kinase-1 (PDK1) to the sarcolemma [61-63]. Akt can further regulate the activity of many ion channel receptors via the activation of the nitric oxide synthase (NOS) [64-65]. Nitric oxide, through the activation of soluble guanylyl and the cGMP formation, can enhance the phosphorylation of cGMP-dependent protein kinase (PKG), which has an antihypertrophic effect through inhibiting intracellular release of calcium via blocking the normal functions of the ion channel receptors [64-67]. Akt also enhances protein synthesis and regulates myocyte size through the activation of the mammalian target of rapamycin (mTOR) dependent pro-growth pathways [62-63, 68-69]. mTOR can regulate gene expression by relieving transcription from the repression of glycogen synthase kinase-3 beta (GSK3B) and inhibitor of kappa B (IKB) [70-72]. GSK3B is a negative regulator of many TFs associated with cardiac hypertrophy and is normally active [70]. Phosphorylation of Akt can inactivate GSK3B and this inhibition can dephosphorylate the TFs and allow the TFs to translocate to the nucleus and initiate transcription process [70,73-75]. As is reported, mTOR can directly regulate protein

translation by activating the S6 kinases and eukaryotic translation initiation factor 4E (eIF4E) [62, 76-77]. More details regarding transcription regulation will be discussed in later subsections.

1.1.1.2. Transmembrane Receptors and Associated Signaling Pathways

Autocrine and paracrine mechanisms, generally mentioned previously, can be triggered by mechanical strain that leads to myocardial hypertrophy through the release of AngII and ET1 [16-17, 31-33]. The JAK/STAT signaling pathway mentioned above is also activated directly by AT1R, indicating these G-protein coupled receptors may also pass the signal through canonical pathways triggered by cytokines [81].

Many transmembrane receptors have acted as signal transducers in response to changes, such as the elevated levels of cytokines and growth factors, in the micro-environment surrounding the cardiomyocytes [20]. For example, glycoprotein (gp) 130 is a common receptor subunit of interleukin (IL)-6-related cytokines and a founding member of cytokine signaling in mechanotransduction [35-36, 78]. Transmembrane gp130 activates protein tyrosine kinases JAKs, which phosphorylate STATs and cause STATs to dimerize and then translocate to the nucleus and initiate gene transcription [78-80].

The major signaling pathway regulated by these G-protein coupled receptors include the mitogen-activated protein kinase (MAPK) signaling pathway [82-83]. MAPKs are serine/threonine kinases that are downstream of the mitogen-activated protein kinase kinases (MEKs) and mitogen-activated protein kinase kinase kinases (MEKKs). These MAPKs mainly include the extracellular signal-regulated kinase 1/2 (ERK1/2), the extracellular signal-regulated kinase 5 (ERK5), the c-Jun N-terminal protein kinase (JNK) and the p38 MAPK [82-84]. These MAPKs have been reported to be quickly activated by mechanical stimuli within a time span of 15 minutes [79,85]. While these MAPKs are mainly regulated by the MEKs and MEKKs,

deficiency in FHL1 results in a loss of ERK1/2 phosphorylation in the pressure overload induced hypertrophy following TAC [86]. This indicates the potential interaction between the quickly activated MAPKs and the cytoskeleton. More importantly, these MAPKs can phosphorylate and activate TFs and promote gene expression [84].

1.1.1.3. The Mechanosensitive Channels and Calcium Signaling Pathways

Cardiac hypertrophy is also associated with marked changes in myocardial contractility that peak active tension increases and the rates of both tension development and relaxation are slowed, which is also associated with alterations in calcium transients [87]. Many of these ion channels are mechanosensitive and have been reported to regulate transmembrane fluxes of calcium [19, 88-89]. Two mechanosensitive channels regulating the calcium transients have been widely discussed, including LTCC and members of TRP channel [90-91]. Studies have shown that LTCC was expressed transiently and the current through this channel was highly sensitive to the flow-induced shear force [90,92]. Further, the α_{1c} subunit of LTCC was directly associated with the mechanical regulation of calcium entry [92]. Similar to LTCC, the TRP family also plays a vital role in regulating the calcium influx. It has also been shown that TRPC6 activity was greatly reduced by a specific inhibitor of mechanosensitive channels, GsMTx-4 [93]. TRPV4, another highly expressed ion channel, was found to be activated in response to increased mechanical loading [94]. Apart from these calcium channels, alterations of other ions have also been stimulated, including sodium. NHE is an ATP-independent membrane glycoprotein transporter that takes Na^+ into the cell and transports H^+ out of the cell and is thus involved in the regulation of intracellular pH [95-96]. The change of the intracellular pH can in turn affect the normal functioning of the calcium influx [96]. Besides, the influx of calcium can also be inhibited by cGMP-dependent protein kinase (PKG) signaling [64-67].

Changes in intracellular calcium levels can regulate many signaling pathways associated with cardiac hypertrophy, including protein kinase C (PKC), calcineurin (CaN), and calcium-calmodulin dependent protein kinase (CaMK) signaling [97-99]. PKC is a serine/threonine kinase that can be activated by mechanical stretch via secondary messengers, such as calcium or diacylglycerol (DAG) [97]. PKC can activate the ERK signaling pathway and regulate the gene expression via the phosphorylation of Raf [100-101]. Activation of PKC further leads to phosphorylation of histone deacetylase 5 (HDAC5), which causes nuclear export of HDAC5, thus can relieve the transcriptional activity of many TFs from the repression of HDAC5 [102-103]. In contrast with PKC, enhanced CaMK activity, especially CaMKII, can translocate HDAC4 out of the nucleus and promote gene expression [104-105]. While CaMK doesn't bind to HDAC5 directly, CaMK can bind the subunit of HDAC4, then disassemble the heterodimer formed by HDAC4 and HDAC5, and facilitate the export of the HDACs out of the nucleus [105].

1.1.2. Mechanosensors and Associated Signaling Pathways in Pulmonary Artery Adventitial Fibroblasts

Another example of mechano-sensing and transduction is in fibroblasts, which regulate ECM in most tissues. A typical response found in many tissues is excess fibroblast-mediated fibrosis under abnormally high mechanical loads. PAAFs are important mediators of fibrotic vascular remodeling during the progression of pulmonary hypertension (PAH) and have been sown to mediate ECM remodeling in response to pathological strains and stresses [106-109]. Increased vascular stiffness and stress are thought to be mediators of PAAF function during PAH [107-109]. PAAFs can bind to ECM ligands such as fibronectin and collagen, sense mechanical signals, and respond to the stimuli via transmembrane receptors [107]. This response is mainly regulated by the interaction of the integrin complex with the ECM [110-112]. Syndecan-4, a heparan sulfate-

carrying protein on the cell surface, can also bind to fibronectin and collagens in the ECM via its glucosaminoglycan chains, and regulate ECM production [112-113].

Similar to cardiomyocytes, many autocrine and paracrine related signaling pathways are also activated in PAAFs [26, 114-121]. AngII is another regulator of ECM production, and increased levels of AngII can regulate collagen expression via the activation of AT1R [115-116]. This is reported to be mediated by TGFβ signaling and other paracrine mechanisms [107, 116, 120-121]. Many other autocrine or paracrine factors such as PDGF, FGF and TNFα, have also been reported to regulate the response of fibroblasts under altered mechanical environments [117-121].

Apart from the canonical pathways in fibrosis, mechanical loading also affects the oxygen consumption within these tissues [3, 26, 75, 122]. Hypoxia, a well-known feature in many pathological disorders, was found to contribute to the pathogenesis of fibrotic disease [24, 26, 122]. Alterations of NO levels in the pulmonary artery and elevated expression of NADPH oxidase 4 (Nox4) were found in PAH rats [116, 122]. Notch signaling, a major pathway involved in the angiogenesis and vascular remodeling, can increase the vessel wall thickness of pulmonary arteries of rats subjected to hypoxia [123-124].

In the following subsections, the downstream signaling pathways associated with these mechanosensors in PAAFs will be introduced.

1.1.2.1. The Cytoskeleton-Related Complexes and the Associated Signaling Pathways

In contrast with cardiomyocytes, where the force transmission along the cytoskeleton is relatively well studied, how mechanical stimuli affects PAAFs via its cytoskeleton is still poorly understood. In response to these mechanical stimuli, the levels of ECM proteins were found to be upregulated, including collagen and fibronectin [23, 25, 107]. Integrins on the fibroblast surface

can bind to laminin via the interaction of the β_3 unit of integrin and further regulate the migration of the cells [107, 118]. Like integrin, syndecan-4 is another signal transducer that can connect to the ECM and interact with the fibronectin on the membrane surface [112, 113]. Reduced calcineurin dependent NFAT activity was found in syndecan-4 KO mice [113]. An NFAT blocker effectively A-285222 prevented the induction of collagen I and III, which are ECM proteins [113]. These results suggest the crucial role of syndecan-4 in mechanical stress induced responses of PAAFs.

1.1.2.2. The Transmembrane Receptors and the Associated Signaling Pathways

Increased production of AngII during cardiac remodeling can induce fibroblast proliferation via AT1R on the cell surface in fibroblasts [115-116]. The AngII induced responses independently activate the MAPK signaling pathways, including ERK1/2 and JNK1/2 via the activation of Ras signaling [126-134]. The phosphorylation of ERK1/2 was found to promote the AngII induced phenotypic differentiation and matrix metalloproteinase 2 (MMP-2) expression in adventitial fibroblasts [134]. JNK1/2 inhibitions blocked AngII-induced gene expression by significantly reducing the phosphorylation of c-Jun and c-Fos that are dimerized to form the transcription complex AP1 [135-136]. This regulation, however, was not affected by the ERK1/2 inhibitor PD98059 [135]. AP1 was involved in the balance between matrix metalloproteinases and their inhibitors metalloproteinases (TIMPs) in the remodeling of ECM [136-142].

Many profibrotic effects on PAAFs differentiation and proliferation may be regulated via autocrine or paracrine mechanisms [26, 114-121]. TGF β induced adventitial fibroblast transformation is mainly regulated by SMAD proteins, which are TFs that the translocation of SMAD proteins into the nucleus regulate gene expression, including αSMA, collagen and elastin [129, 143-146]. TGFβ was shown to be activated by AngII via a feedback program that encodes

latent TGFβ and its release to ECM and binding to the TGFβ receptor (TGFβR) [147-148]. TGFβ can also regulate MAPK signaling of p38 via the activation of TGFβ activated kinase 1 (TAK1) [130, 147]. p38 is found to involved in the regulation of many genes via the NFκB and AP1 transcription factor. NFκB is an important regulator of the gene expression encoding for fibronectin and the MMPs [147, 149-150].

Similar to TGFβ, increased PDGF binding to PDGF receptor (PDGFR) was found in induced fibrosis [117]. This factor is an important regulator of the transformation, proliferation and the collagen secretion of fibroblasts via the PI3K/Akt signaling pathway [151-152]. MMP-2 responses were significantly reduced in Akt deficient cells, suggesting that the NFκB signaling is dependent on PI3K/Akt signaling [153]. Exogenous fibroblast growth factor (FGF) is another growth factor that have been reported to regulate the adventitial fibroblast migration [118]. FGF stimulated the expression of OPN and significantly upregulated the MAPK signaling activities such as ERK1/2 and JNK1/2 [111, 129, 154].

Reports showed that the stimulated MAPK signaling pathways and PI3K/Akt could turn on the Hippo kinase core, including MST1/2 [155-157]. Though these pathways are not well explored in fibroblasts, it has been suggested that the Hippo signaling may regulate several miRNAs including miRNA-130/301, which are critical in collagen deposition and remodeling [157-158]. ECM remodeling was shown to promote the pulmonary hypertension via the feedback mechanoactivation of the miRNA-130/301 [158]. The induction of miR-130/301 was found to be regulated by the TF OCT4, which was inhibited by YAP/TAZ in stiff matrices [158]. The activation of YAP/TAZ was induced by the phosphorylation of LATS1/2 regulated by MST1/2 [157-158]. The collagen deposition and remodeling regulated by the miRNAs was found disrupted by the PPARγ and LRP8 axis [159].

1.1.2.3. The Mechanosensitive channels and the calcium signaling pathway

Compared with cardiomyocytes where the roles of mechanosensitive channels are well defined, the role of these channels in fibroblasts such as PAAFs are not well-characterized. Many non-sensitive ion channels, including K_{ATP}, CAV3.1 and BK_{C_a}, were found to be expressed in fibroblasts but it is reported that the mechanosensitive channel TRPV4 plays a more important role in the mechanoelectric feedback of fibroblasts [159-162]. The elevated calcium further activates PKC signaling, which was found to be crucial in the expression of αSMA and elastin [162-164].

1.1.2.4. Hypoxia Associated Signaling Pathways

Exposure to hypoxia is associated with the PAAF remodeling process [123-124]. Hypoxia-induced pulmonary hypertension was mainly regulated by endothelial nitric oxide (NO), Notch signaling, and stimulated activity of the NADPH oxidase 4 (Nox4), which further activates ROS [120, 123-124]. Hypoxia-inducible factor 1α (HIF1 α), an intracellular mediator of ROS, interacts with the Notch receptors and stabilize the Notch intracellular domain (NICD), which then translocates to the nucleus and regulate the gene expression αSMA via the progressive expression and regulation of HERP [124].

1.2. Signaling Network Models

Computational signaling network models represent a powerful tool to better understand the function of biological signals and how they can be represented as a mathematical model, incorporating experimental data and functional outcomes [165-166]. These models are typically developed for an individual cell type, and usually are limited to a single or related groups of cellular functions. For example, cardiac hypertrophy (growth of cardiomyocytes [165, 167]) has been extensively investigated with experiments to quantify the protein synthesis and resulting cellular growth patterns, and the underlying mechanical and receptor-mediated signals that induce the

cellular growth [167]. These mechano-sensitive pathways can be remodeled via systems-type approaches that start with mechanical or chemical signals and results in cellular growth and remodeling. Similar approaches can be used in a fibroblast, for example, systems-based approaches can model the functions of a fibroblast that result in tissue fibrosis due to mechanical or other input stimuli.

Two main approaches in modeling such systems have been widely discussed, including the logic-based models and the continuous models [165-166]. Many biological processes show 'ON/OFF' switch-like behaviors, where 'ON' may represent 'active' and 'OFF' for 'inactive'. Boolean network models, representing the regulatory functions as logic gates, are some of the most commonly used logic-based models that can describe this behavior. Sanchez et al. used this approach to model the qualitative gap in gene expression patterns between wild type and mutant *Drosophila* [168]. Such Boolean network models are very simple and efficient since they usually require only a small number of parameters in the simulation. This characteristic, however, also has the drawback that many temporal dynamics will not be present. The differential equations approach, representing the regulatory functions as a set of differential equations, has been widely used to present evolving dynamics continuously. A well-known application of this approach is the bacterial operons such as lac and tryptophan [169-171]. In order to present more details regarding the evolving dynamics, more parameters are required, thus increase the computational complexity significantly [165-166].

A recent signaling network was formulated by integrating the mechanosensitive pathways in cardiomyocytes described in Section 1.1 [172]. This signaling network was modeled using a combination approach of Boolean network model and Continuous model approaches [172-173].

In the following subsections, the approaches that are used to model biological signaling networks are outlined accordingly.

1.2.1. Boolean Network Approach

The states of nodes in the biological processes are often synchronous and updated according to the regulating functions. The regulation functions are either activation or inhibition, which is represented as 'NOT'. Within these regulation functions, there may exist interactions between nodes in these processes. Thus, the regulatory functions can be further refined with co-regulation using two logical operators: 'AND', representing where the activation requires the activity of multiple upstream nodes; "OR", representing a reaction in which the node can be activated by multiple inputs independently.

$$f_{AND}(Q) = f(AB)$$

$$f_{OR}(Q) = f(A) + f(B) - f(AB)$$

Q is a node regulated by A, B.

To describe these behaviors, Logic-based models such as Boolean Models are used to define the structure of the nodes and the relationships between them in the network, and to represent the regulatory functions with the use of logic gates. These models often define the local state of each node at any time as a discrete level. The logic-based model is a relatively simple approach to allow the species to remain in one of the two states: **ON** or **OFF**, representing activated and inhibited states, respectively. The states may evolve into dynamic progress as nodes in the network switched states between **ON** or **OFF** until the steady state is achieved. These characteristics have made logical models efficient in terms of time and convenient in terms of model complexity.

1.2.2. Differential Equations Approach

Continuous models are usually deterministic and used to summarize experimental results with real-valued data. In contrast with the basic logic-based models discussed in the previous subsection, continuous models allow the direct quantitative comparison between different states and thus are more accurate. Among continuous models, differential equation models are widely used in modeling gene expression.

For many biological systems with high-quality measurements, differential equations can capture the dynamics nature of these systems. These equations describe the levels of each node as a function of other components in the network. In the context of biological signaling models, the change of each node (presence of a particular biological species) is defined as a result of rates of production and decay of the species, where production is defined by the activation or inhibition by the rules related to the node and decay is determined by the node degradation (see the equation below). Differential equation models usually include two groups: ordinary differential equations (ODE) and partial differential equations (PDE). Both systems usually have time-dependent variables while the latter may include spatial variables. Compared with PDE, ODEs are usually simpler in terms of formulations and more efficient in terms of computation complexity.

$$\frac{dNode}{dt} = Rate_{production} - Rate_{dacay}$$

1.2.3. Normalized-Hill Equations Approach

A normalized-Hill differential equation approach based on logical operators, as described previously [172-173], was used to model the interactions between species within the mechanosignaling network (MSN). The activity of each species was normalized and varies

between 0 and 1. The interactions between species within the cardiomyocyte mechanosignaling network were modeled using Hill-type equations based on logical operators [173]. The activity of each species in the network is represented by a state variable normalized to vary between 0 and 1, and reactions are represented by the logic-based differential equations developed for modeling biochemical networks [174] in which the activation of each species varies according to a sigmoidal Hill function. The state variable y_i for species i in the network regulated by species j is governed by:

$$\frac{dy_i}{dt} = \frac{1}{\tau}\left[\omega_{ji} f_j y_{i,max} - y_i\right]$$

where τ_{ji} is the reaction time constant determining the rate of change of species i, ω_{ji} is the general reaction weight that can vary between 0 and 1, and $y_{i,max}$ is defined as the maximal activation of species i in the network. Typically, $\omega_{ji}$is 1 or close to one unless the node is being pharmacologically or genetically inhibited or knocked down. The Hill function f_{ji}, can be activating (*act*) or inhibitory (*in*):

$$f_{ji} = \begin{cases} f_{act}(y_j) = \dfrac{By_j^n}{K^n + y_j^n} & if\ activating \\ f_{in}(y_j) = 1 - \dfrac{By_j^n}{K^n + y_j^n} & if\ inhibitory \end{cases}$$

where B is a function of the Hill coefficient n and the half-maximal activation EC_{50}:

$$B = \frac{EC_{50}^n - 1}{2EC_{50}^n - 1}$$

$$K = (B-1)^{\frac{1}{n}}$$

1.3. Transcriptional Regulatory Network and Model

Cardiomyocytes alter gene expression patterns via the transcriptional regulatory network in order to adapt to mechanical stimuli [3, 5]. Transcriptional regulatory networks are used to illustrate and assess gene expression regulation as a result of interplay between transcription factors and DNA [3, 5, 174-176]. A transcription factor (TF) is a protein that can control the rate of transcription by binding to a specific site on the DNA sequence, including enhancers that boost the activation of gene expression and repressor that decrease the gene expression [175-176]. When TFs are bound to these sites, it may become easier or harder for the RNA polymerase to bind to the promoter of the genes [175-176]. TFs are composed to two functional regions, including the recognition and the binding of the DNA sequences. These regions may interact with coregulators and connect to the transcription complexes and thus recruit or prevent the RNA polymerase binding to the promoter regions [175-176].

Many genes have multiple binding sites upstream of their sequences. Individual TFs adapt their conformation and functions to assemble a protein-DNA complex [175-177]. The further alteration in the structure of the complex will then mediate the activity of the transcriptional machinery. These combinatory regulations, commonly represented as 'AND' mechanism, can describe the transcription of the genes. The gene is only expressed when all activators are present otherwise the gene is partially transcribed. When a repressor is present, the gene transcription is thus blocked. When both activator and repressor are present, there are two main mechanisms proposed. The activator and repressor bind to the different regions, which results in total block of gene expression, or competitive binding wherein the activator and repressor competitively bind to the sequence. Rather than blocking gene expression, the gene can still be transcribed but the expression level may be limited.

Many TFs have been shown to be associated with the remodeling of cardiomyocytes in hypertrophic diseases.

1.3.1. Mechanosensitive Transcription Factors

The mechanosensitive pathway sends signals from transmembrane receptors and channels to the cytoplasm and then to the nucleus, where the activation of TFs is mediated [3, 5, 174]. Many TFs have been found to be upregulated as well as the expression of some marker genes in cardiac hypertrophy [178-180]. For example, Nuclear factor kappa-light-chain-enhancer of activated B cells (NFκB) is a major transcription factor regulating multiple cellular functions including cell growth related to cardiac hypertrophy [3]. NFκB transcriptional activity is mainly regulated by inhibitor of kappa B (IkB) and inhibitor of kappa B kinase (IKK). IKB is normally turned on that NFκB is bound to the inhibitor protein IkB in the cytosol. Activated IKK can phosphorylates IkB, which can dissociate IKB from NFκB and further allow NFκB to translocate to the nucleus and bind to its DNA response element [181]. It is also reported that inhibitors of p38 and ERK can partially block the dependent gene expression [182].

Nuclear factor of activated T-cells (NFAT) is a family of TFs that was first discovered to activate the transcription of genes [73, 183-184]. Increased expression of FHL2 can suppress the stress-induced activation of CaN, which further leads to the inhibition of NFAT dependent gene expression [73, 183-184]. The phosphorylation of GSK3b promotes the nuclear exit of NFAT while NFκB can directly interact with NFAT on NFAT-dependent transcription [73, 183].

Signal transducer and activator of transcription (STAT) is a transcription factor phosphorylated and activated by JAK that translocates into the nucleus to induce gene expression [185-186]. In the nucleus, STATs can cooperatively bind with other TFs, such as NFκB and

NFAT, then form a mediator complex and locate to promoter regions of their target genes and activate gene transcription [187-189].

Myocyte enhancer factor-2 (MEF2) and Serum response factor (SRF) are both MADS-box TFs and reported to form a mediator complex as mentioned above [190-191]. MEF2 can regulate cardiac gene expression through the direct phosphorylation of p38 and ERK5 [192-193]. Translocation of class II HDACs out of the nucleus have been shown to relieve the repression of MEF2 target genes transcription [102-105]. Compared with MEF2, SRF can regulate many immediate early genes and the SRF induced gene transcriptional activity can also be attenuated by the translocation of HDACs [178, 194-196]. The muscle ring-finger (MuRF) family of proteins interacts with SRF and inhibits SRF transcriptional activity [195]. Myocardin-related transcription factors (MRTFs) are key coactivators of SRF that link actin dynamics to SRF-mediated gene transcription [196]. FHL2 binds to the promoters of SRF-response genes and competes with MRTF on SRF-binding [195-196].

The cyclic adenosine monophosphate response element-binding (CREB) is a cellular TF that has been found to be elevated in the nucleus by cyclic mechanical stretch [197-198]. CREB were also found involved in the cooperative regulation of gene expression by binding with the NF κ B/STAT and SRF/MEF2 [191, 199]. Elevated GSK3b activity resulting in the de-phosphorylation of CREB was found in hypoxia induced hypertrophy while p38 was shown to induce the phosphorylation of CREB [75].

cJun and cFos are TFs that also combine to form the early response transcription factor AP-1 through heterodimerization [180, 200-201]. Both c-Jun and c-Fos transcription are autoregulated by their own protein products [180, 200-201]. The up-regulation of these immediate early genes have also involved in the adaptational response of cardiac hypertrophy [202]. Their

activities have also been found to be regulated by ERK1/2 while c-Jun is further regulated by JNK signaling [203-205].

Cellular Myc (cMyc) is one of most frequently activated member of Myc family transcription factors and promotes compensated cardiac hypertrophy [206-207]. cMyc gene expression was found to be rapidly upregulated and its activation was sufficient to reproduce the characteristic changes in myocyte size and protein synthesis in the induction of cardiac myocyte hypertrophy [206-207].

It is suggested that GATA4 might play an important role in regulating cardiac development since many cardiac muscle-specific promoters and enhancers including the cardiac troponin C enhancer, the α-myosin heavy chain (α-MHC), and the artial naturietic factor (ANF) have GATA4 binding sites [208-211]. And the overexpression of GATA4 can transactivate these promoters, however, its role in regulating gene expression in response to mechanical stimuli remains unclear [212].

All TFs discussed so far are pro-hypertrophic that the elevated TF activitis can lead to cardiac hypertrophy. In contrast to these TFs, Forkhead box O (FoxO) was found to be a negative regulator of hypertrophy where it prevents cell growth of cardiomyocytes [213-214]. The phosphorylation of FoxO by PI3K/Akt signaling pathway results in the translocation of FoxO out of the nucleus [213-214].

1.3.2. Target Genes of Mechanosensitive Transcription Factors

Past studies have used inhibitors of certain transcription factors or a knock-out model to identify the interactions with genes by measuring the gene expressions through PCR. However, these approaches can only measure a limited number of genes concurrently and are less specific and accurate since interactions between the regulations are not considered [215].

Chromatin immunoprecipitation (ChIP), commonly used to analyze protein interactions with DNA in large scale, can determine whether a TF can bind to the promoter region of a gene [216-218]. In combination with sequencing technology, ChIP-Seq can identify direct interactions between TFs and target genes by probing all genomic regions for potential binding by the TF [216-218]. The direction of the interactions is often determined by observing the measurement if a gene is significantly upregulated or downregulated when a TF is perturbed.

Typically, these experimentally based techniques have been used to construct transcriptional regulatory networks. When the data is insufficient, many computational methods have been proposed to predict the binding activities between TFs and genes of interest [218-226]. One approach is to identify the TF binding sites (TFBS) on gene sequence through the analysis of the predicted binding sites for genes of interest since many genes co-regulated by the same TF share same binding sequences [219-223]. These TFBS, however, are usually short and variable within large non-coding regions, and the determination of these TFBS requires large amounts of experimental measurements and complicated algorithms, which is currently not computationally efficient [223-224]. Some approaches implement a genome-wide ranking-and-recovery approach using cis-regulatory sequence analysis to detect enriched transcription factor motifs and their optimal sets of direct targets [224]. Other approaches, like deep learning techniques, have widely taken advantage of the large number of Chip-Seq datasets to predict co-regulated genes and the corresponding TFs [225-226]. The emergence of these computational methods has greatly reduced the experimental workload while achieving high accuracy.

To better understand what genes are involved in the regulation of cardiac hypertrophy, genes that are targets of the 11 TFs mentioned previously were collected and categorized thusly:

- The TF-gene interaction was identified from experiments conducted in mouse or rat.
- The TF-gene interaction was identified through published ChIP-seq datasets and verified using computational approaches.

For each TF, a list of target genes and the TF's effect on the expression direction of the target genes were compiled. Each reaction was substantiated with both co-expression evidence and DNA binding evidence as discussed in Section 1.3.1. Co-expression evidence was identified using studies, preferably in myocytes, where a TF was perturbed, and whole genomic changes were measured by microarray or RNA-Seq.

The gene regulatory network is constructed based on TF-gene regulations where at least 1 of these criteria was met. Candidate genes were validated as having a binding site for the TF using iRegulon [224]. iRegulon is a binding motif analysis tool that utilizes position weight matrices from TRANSFAC [227], JASPAR [228], and UNIPROBE [229] to identify the TFs that can bind to a set of genes. Once the target gene list was finalized, reactions were added to the model to simulate their gene transcription by the TFs. Furthermore, the target gene list was cross-referenced against the nodes in the mechanosignaling network in order to implement feedback loops. Reactions were added to the model to simulate protein translation from gene product to the upstream protein node.

1.3.3. Extension of the Regulatory Network with Genes

Previously, a combinatory approach combining the Boolean network model and the differential equations was shown that could capture the dynamics of the changes of the signaling nodes in response to altered stimuli when the data is not sufficient. However, this approach is incapable of predicting exacting gene expression changes when quantitative data is present. To

allow the model to quantitatively describe gene expression, a mass-action method based on the Mass Conservation Law was introduced for the interactions between transcription factor and gene. The rate of gene expression change depends on the regulation by the corresponding TFs and its natural decay rate. which is adapted from Hill equation and modeled as followed:

$$\frac{dGene_i}{dt} = \frac{\omega_i N_i Hill(TF_i)}{\tau} - \frac{Gene_i}{\tau}$$

where the transcription rate N_i are defined as followed:

$$N_i = \frac{Gene_{i,control}}{\omega_i Hill(TF_{i,control})\tau_i}$$

To numerically simulate the effects of stretch, a small stretch stimulus is first used by running the Hill model and mass-action method to a numerical steady-state in order to mimic cellular steady state, which generates the control values of signaling molecules and the gene normalization constants. A fixed-intercept (0) linear regression is then conducted by comparing the experimental measurements with model simulation. The closer to the unity line, the better the effect was at mimicking the steady state. Using this method, a new stretch input will be determined and then applied to the system to simulate gene expression with a time course of interest.

Default parameter values (ω= 1, n = 1.4, and EC_{50} = 0.5) except τ were used for all reactions unless specified. Kinetic parameters for target genes were determined using an mRNA half-life (HL) database [230]. HL was converted to the time constant τ using the formula:

$$\tau = \frac{HL}{ln2}$$

For all other nodes, τ = 30 seconds was used. This time constant will allow nodes such as ERK1/2 and p38 MAPK to reach peak activation by 10 minutes of stretch, which matches previous data that maximal phosphorylation of ERK1/2 and p38 MAPK is induced by 10 minutes of stretch [231].

1.4. RNA Sequencing and Data Analysis

Quantitative reverse transcription polymerase chain reaction (RT-PCR) is one approach for measuring mRNA abundance. This technique can also be used quantify the expression of hundreds of genes simultaneously for expression profiling [215]. This method, though less expensive, requires intensive labor and may generate a small bunch of genes [215]. Microarray, a single chip or array containing probes to determine transcripts levels for all genes, has replaced PCR for when gene expression needs to be measured at a much larger scale [215]. A more robust and accurate approach based on next generation sequencing (NGS), also known as RNA-Seq, can identify gene expression and even the splicing information when little information is available [216, 232]. RNA Sequencing has become the new standard approach for probing gene expression changes in response to an experimental stimulus especially since the cost has dropped significantly in recent years [216, 232].

The RNA samples are sequenced, and raw read files are generated that contain the nucleotide sequence of each read. The read files are often stored in formats such as fastq and fasta. In single-end reading, the sequencer reads a fragment from only one end to the other, generating the sequence of base pairs. Then as the technology advanced, paired-end reading was invented to improve the sequencing quality [233-234]. In paired-end reading, it starts at one read, finishes this direction at the specified read length, and then starts another round of reading from the opposite end of the fragment. Compared with single-end reading, paired-end reading improves the ability to identify the relative positions of various reads in the genome, making it much more effective than single-end reading in resolving structural rearrangements such as gene insertions, deletions, or inversions [233-234]. It can also improve the assembly of repetitive regions. However, paired-end reads are more expensive and time-consuming. In some cases, samples using single-end

technology can be combined with those of paired-end for data analysis but may require further understanding [235].

1.4.1. Quality Control and Sequence Alignment

Raw RNA-Seq data may have quality issues, which significantly distort analytical results and lead to erroneous conclusions. Therefore, the raw data may be subjected to vigorous quality control (QC) procedures before downstream analysis. After the quality control is performed, an optional step is data trimming, which aims at removing unnecessary sequences of bad quality [236-237]. If the data are used for variant analyses, genome annotation or genome or transcriptome assembly purposes, it is strongly recommended that read trimming should be performed, including both adapter and quality trimming. For differential gene expression (DGE) RNA-seq analysis and ChIP-seq, however, read trimming is generally not required anymore when using modern aligners, which will "soft-clip" non-matching sequences [236, 238].

Following quality control, the next step is to align the RNA-Seq reads with the reference genome to identify the correct genomic loci from which the read originated. Read alignment is one of the first steps required for many different types of analysis. In RNA-seq, alignment is a major step for the calculation of transcript or gene expression levels; several splice aware alignment methods have been developed for RNA-seq experiments such as STAR, HISAT2 [239-240]. These aligners are designed to specifically address many of the challenges of RNA-seq data mapping using a strategy to account for spliced alignments [239-240].

1.4.2. Data Normalization

After sequence alignment, the next step is to estimate the reads count of each genomic feature. This process uses a reference transcriptome and counts the number of reads that uniquely maps to the transcripts. Common tools such as HTseq and featurecounts have been used to count

the reads [241-242]. Both methods ignore reads that are mapped to multiple transcripts since any single fragment must originate from only one of the target genes, but the identity of the true target gene cannot be confidently determined [241-242]. Feature captures more read counts compared with HTSeq while being more efficient in terms of memory and running time [242-243].

A naive comparison of read counts for a given gene under the different conditions is problematic for two reasons. First, the number of reads aligned to a given gene in each sample is generally considered a random variable (though non-random events, such as inconsistent fragment amplification or poor amplification of certain sequences, can impact the final read count), and thus read count comparisons must take into account the variability of these random variables [244-245]. Second, the total number of reads can vary across samples, and a large difference in a gene's read count between different conditions may simply be the result of differential coverage, rather than of differential expression [244-245]. It is the second problem that necessitates normalization of read counts before differential expression analysis can be performed. The main factors often considered during data normalization include sequencing depth, gene length, RNA composition [244-246]. Samples with larger sequencing depth usually have larger number to total gene reads. This may result in higher expression for any individual genes. Similarly, more reads can map to genes with bigger length. Besides, a few highly differentially expressed genes between samples, differences in the number of genes expressed between samples, or presence of contamination can skew some types of normalization methods [244-246].

Many normalization methods have been proposed to minimize the variance and used to normalize the gene counts in order to make gene expression across samples comparable [246-253]. Counts per million (CPM), counts scaled by the total number of reads in a given sample, have been used to analyze the gene count comparisons between replicates of the samples within the same

group. Similarly, transcripts per kilo million (TPM), a method based on CPM, further scale the CPM over gene length. On the basis of TPM, reads/fragments per kilobase of exon per million reads/fragments mapped (RPKM, FPKM) normalize the raw gene counts over sequencing depth and gene length but in a different order. The two other approaches further involve sequencing depth and RNA composition during the normalization of data, including DESeq2 and EdgeR [248-249]. DESeq2's median of ratios are computed where raw counts are divided by sample-specific size factors determined by median ratio of gene counts relative to geometric mean per gene [248]. EdgeR computes trimmed mean of M values using a weighted trimmed mean of the log expression ratios between samples [249]. FPKM/RPKM are less popular now since the total number of normalized counts are different between samples where large sequencing depth usually caused large variance in terms of the total counts [247, 250].

For data comprised of multiple repeated experiments, these normalization approaches may not be appropriate when samples are more likely to be grouped by individual experiments rather than experimental treatments. For example, these methods are unable to handle data composed of both single-end and paired-end samples. In our work, DESeq2 will be used for data normalization and differential analysis of gene expressions.

1.4.3. Statistical Testing

After data normalization, the final step is to perform differential analysis. Since variance in RNA-Seq data is much higher than the mean due to the technical difference in the biological replicates, a negative binomial distribution is applied to account this overdispersion. Both DESeq2 and edgeR calculate the overdispersion by utilizing empirical Bayesian model on each gene and then deriving the average variance from all genes [248-249]. Following the variance calculation, a statistical test is conducted to determine if a gene has significant change in expression between

treatment group and control group. DESeq2 uses Wald test while edgeR uses an exact test similar to Fisher's exact test [248-249]. Other tools may use tests such as the Wilcoxon signed-rank test, an alternative to the paired Student's t-test when the distribution of the difference between the mean of two samples cannot be assumed to be normally distributed.

Since RNA-Seq data from mammalian cells usually has more than ten thousand genes, it is often required to conduct the Benjamini-Hochberg correction for multiple comparison after calculating the p-values. This procedure can reduce false positives and control the false discovery rate (FDR) [254]. Additionally, many researchers may also apply a minimum fold change check along with statistical test to determine DE gene.

1.4.4. Statistical Analysis of RNA-Sequencing Data

Modeling biological systems has been a basic and critical challenge in systems biology. The regulatory network is commonly shaped as a diagram/graph with each species representing a node and the corresponding regulation acting as an edge connecting two nodes [165, 255]. Klamt *et al* proposed a formatting methodology for the structural and functional analysis of these regulatory networks which includes the structure definition and verification, mathematical formulation, prediction and validation analysis of the network [255]. To understand the functions of such a given network, the logic-based models and continuous models have been introduced in section 1.2 to illustrate the corresponding biological phenomena of interest. These approaches based on existing knowledge, however, are unable to predict the gene regulation patterns that are not known yet. Rapid development of data such as multi-omics and imaging provides a unique perspective to analyze the regulation patterns from the data directly without knowing any prior information. Multi-omics data including transcriptomics and proteomics is the most-commonly used data type in analyzing regulatory network. Statistical approaches have thusly been commonly

used to uncover such gene regulation patterns and their relationships with specific diseases [256-260]. The goal of this approach is to discern regulatory patterns or regulatory networks underlying in the data.

These statistical approaches can be highly effective for data comprised of large-scale expression profiles such as transcriptome data. Among the statistical models, identifying the difference between conditions through multiple testing is a straightforward approach to extract unknown regulating patterns. By analyzing the differential expression, it can be easy to determine a subset of genes induced under a given experimental condition.

Statistical correlations can cluster genes with similar expression patterns under different experimental conditions and unveil important functions and regulatory patterns [256-258]. Clustering, an unsupervised learning technique, have been used to group genes in the gene expression profile data with different expression patterns. The two most-commonly used clustering methods for analyzing gene expression profiles and protein activities are hierarchical clustering and k-means clustering [256-258]. The most common form of hierarchical clustering is a bottom-up agglomerative approach that organizes the data into a tree structure without user input by starting with each data point as its own cluster and iteratively combining them into larger clusters or ‘clades’ [257]. In contrast, k-means clustering requires the investigator to define the number of clusters (k) a priori, and data are then sorted into the cluster with the nearest mean [258]. Prior to applying these clustering methods on gene expression data, data transformations are often conducted on the RNA-seq count data that usually follows negative binomial distribution [253]. Logarithmic transformation can reduce the variability and make the data closer to normal distribution while variance stabilizing transformation can stabilize the asymptotic variance over the full range of the data. Depending on the data types, different distancing functions may be

applied to calculate the similarity between any two given genes. Many pathway analysis tools have relied on clustering methods to correlate genes with similar expression profiles and highlight the potential functionalities, such as the KEGG enrichment analysis tool [261].

Other statistical models such as machine learning or graph-based models using neural networks are more advanced approaches that have been applied to infer disease-related patterns [259-260]. Such approaches have become more important and commonly-used and will be discussed in the future.

1.5. Current Open Questions in Cardiac Systems Biology and the Motivation for the Dissertation

1.5.1. Uncertainty Quantification of Model and Data

In the original report of the MSN [172], the robustness of model accuracy was evaluated by a simple general sampling of parameters such as weights and Hill coefficients, assuming such parameters share the same default values. Realizing that parameters may be different for each reaction used to formulate the model, it is appropriate to extend the analysis by a system of uncertainty quantification of parameters for each reaction. Through this type of analysis, we explored which network modules and outputs are most sensitive to parameter uncertainty and which parameters propagate the most error. In addition, the original study did not discuss how network modules cooperate in the regulation of the model. A goal of the current work is to use uncertainty quantification (UQ) to investigate the consequences of epistemic uncertainty in the model logic. As a step forward, the likelihood of errors produced by biological experiments will be estimated, which are almost invariably under-powered. The details of this study are described in Chapter 2.

1.5.2. Stretch-Induced Response in Cardiomyocytes

The internal organization of the sarcomere and cytoskeleton suggests that myocytes may respond differentially to mechanical loading applied either parallel or transverse to the long axis of the cell. When cultured on micropatterned substrates, previous studies showed elongated neonatal rat cardiac myocytes exhibited different phenotypic responses to 24 hr of static stretch when the stretch was applied primarily along the cell axis compared with transverse to it [262-263].

Previous studies have also shown that longitudinal uniaxial stretch of aligned neonatal rat ventricular myocytes induced the addition of new sarcomeres in series so that by six hours the original unstretched sarcomere length had been restored [264]. Hence, the hypertrophic signaling and remodeling responses to stretch in neonatal myocytes *in-vitro* are likely quite rapid. Many studies have also shown evidence of paracrine and autocrine responses to stretch that act over short and longer-term time scales [265]. Also, longitudinal stretch induced both cardiomyocyte elongation in the longitudinal axis and lateral extension, while transverse stretch only caused lateral extension [266]. Therefore, the main goal of the current study is to examine differential gene expression profiles after up to 4 hr of stretch in micropatterned neonatal mouse cardiac myocytes, and compare responses when the cells are stretched primarily along or transverse to their long axes. This work is discussed in detail in Chapter 3.

1.5.3. Pro-Fibrotic PAAF Cell Signaling

PAH is a vasculopathy manifested by sustained elevation of pulmonary arterial pressures, vascular constriction, and irreversible vascular remodeling, which is mediated in part by PAAFs in response to pathological mechanical overload and hypoxia [23-26]. As another application of systems modeling to help uncover mechanisms of cellular mechanotransduction, we extended our

previous work in the PAAFs to study the interplay between the effects of signaling cytokines, hypoxia, and the mechanical stimuli that are activated in PAH using the same computational approach as described previously in section 1.2 and 1.3 for cardiomyocytes. Using systems modeling approaches, we aim to elucidate signaling pathway interactions and identify the key regulators in vascular adventitial remodeling as the result of changes in stretch and matrix stiffness that occur during the progression of PAH. Chapter 4 discusses this work in detail.

Chapter 2: Quantification of Model and Data Uncertainty in a Network Analysis of Cardiac Myocyte Mechanosignaling

2.1. Introduction

Increased hemodynamic loads acting on the heart can result in ventricular hypertrophy and remodeling. In response to altered mechanical loading, a variety of mechanotransduction mechanisms and mechanosensitive cell signaling pathways are activated in cardiomyocytes [267]. A mechanosignaling network model that our groups developed earlier [172] successfully predicted 134 qualitative results of 172 input-output (9/9), input-intermediate (43/43) and inhibitor (82/120) experiments that had been reported in 55 published papers not used for the initial model formulation. The model was represented as a Boolean network and implemented as a system of logic-based ordinary differential equations in which 94 normalized state variables represent upstream stimuli and ligands, cell surface receptors, signaling molecules, transcriptional regulators and cardiomyocyte marker genes and phenotypes. The parameters of the 125 activating and inhibitory reactions linking the species of the network included the Hill coefficient n (set to a constant of 1.4) and half-maximal effective concentration EC_{50} (set everywhere to 0.5). Each state variable had an initial activation of 0, maximal activation of 1, and a time constant τ of 1.

While our original report did investigate the robustness of the model accuracy to parameter uncertainty [172], here we extend the analysis by exploring which network modules and outputs are most sensitive to parameter uncertainty and which parameters propagate the most error. We also use uncertainty quantification (UQ) to investigate the consequences of epistemic uncertainty in the model logic, and finally we quantify how data uncertainty in the experimental results used to validate the model affects the estimated accuracy of the model. Of particular interest regarding

this type of data uncertainty is the greater likelihood of type II than type I errors in cell biological experiments, which are almost invariably under-powered.

For deterministic systems of ordinary differential equations with known initial conditions, parameter values are usually chosen based on reported models or experiments, or they are optimized to fit observations. However, these parameters are typically uncertain owing to limitations in the availability, reproducibility or accuracy of experimental measurements [268]. Uncertainty quantification (UQ) has been widely used to identify statistical estimates of model outputs where parameters, such as the reaction weights and Hill coefficients in our network model, are approximations or a consensus of differing estimates [269]. A variety of UQ methods have been used including Monte Carlo (MC) methods [270] and polynomial chaos expansions (PCEs) [271], which can be more computationally efficient. Here we used both approaches to quantify the effects of uncertainty in model parameters, model logic and validation data on estimated model accuracy. We used these findings to identify specific model parameters, sub-networks and data limitations that should be the focus of further experimental investigation for model improvement.

2.2. Methods

We performed UQ analysis of the mathematical model of the cardiac myocyte mechanosignaling network described by us earlier [172] to assess the effects of uncertainty in model parameters, model logic and the experimental validation data on assessments of model prediction accuracy.

2.2.1. Model Formulation

The interactions between species within the cardiac myocyte mechanosignaling network were modeled using Hill-type equations based on logical operators [172] described in section 1.2. The model [172] has 125 reactions and 94 species derived from published experimental reports.

The default parameter values were $\omega = 0.9$, n = 1.4, $EC_{50} = 0.5$, $\tau = 1$ min, and $y_{i,max} = 1$ for all species and reactions. Applying a stretch input of 0.7 to the system stimulates output responses similar to those observed in response to an *in-vitro* strain of ~ 20%. The constant input and parameter values of stretch (0.7), weights (0.9), Hill coefficient (1.4), EC_{50} (0.5) and time constant (1 minute) selected in the original model study [172] were used here as default values with no formal attempt at parameter optimization. The default input stretch and weight values were chosen manually in the original study to achieve steady-state activation of between 50% and 95% of network nodes [172]. The default Hill coefficient and EC_{50} were chosen in the original paper based on typical values commonly reported in biochemical literature [172-173, 272]. The resulting system of ordinary differential equations that describe the regulatory network dynamics is integrated numerically using the LSODA algorithm for stiff ODEs that automatically switches between the Adams' method and the Backward Differentiation Formulae (BDF) method. Our numerical implementation of this network has been customized and released as a Jupyter notebook available to the public (Refer to the example folder in the Github repository for simulated data).

2.2.2. Model Validation

To validate the predictions of the mathematical model in the original study, experimental data were set aside from 55 papers that had not been used during the initial model formulation [172]. These studies contained 172 experimental results collected from *in-vitro* experiments comprising 52 input-output or input-intermediate experiments and 120 inhibition experiments. Using the reported statistical threshold, the result of each published experiment was classified as the output node being increased, decreased or unchanged. For comparison, a change in the magnitude of the model-computed output of greater than or equal to a threshold of 0.05 was classified as an increase or decrease, while responses of less than 0.05 were classified as

unchanged. A mathematical definition of this metric for model accuracy is summarized in supplement S2.1. Applying these criteria to the model with default parameters, the model correctly predicted 100% of input-output and input-intermediate observations and 68% of the 120 inhibition results. In this study, we examined the effects of parameter, structural and data uncertainties on these validation metrics (figure 2.1).

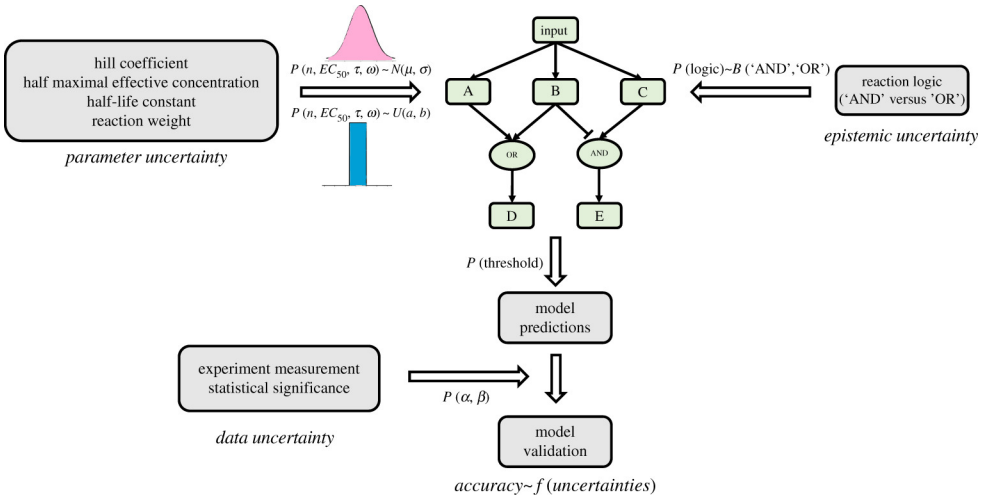

Figure 2.1| Sources of uncertainty in validating the accuracy of logic-based network models of cell signaling. An example network with five nodes that includes examples of 'NOT', 'AND' and 'OR' reaction logic. Uncertainty in model-predicted results arises from parameter uncertainty and epistemic uncertainty in model structure and logic. Validation requires comparison of model results with experimental data that are subject to statistical uncertainty. (Online version in color.)

2.2.3. Sources of Uncertainty

We investigate the effects of parameter uncertainty in model reaction coefficients, epistemic uncertainty in pathway logic, and data uncertainty in validation measurements on estimates of overall model prediction accuracy. In the original analysis, the parameters n, ω, EC_{50} and τ were set to be constant for every reaction, but here we allow every parameter to be assigned to a different random value for every ODE. Moreover, while the molecules and basic structure of the signaling network are in general clearly reported in the experimental literature, the choice of

reaction logic that best reflects the literature is more often subject to interpretation. Finally, there is statistical uncertainty in the conclusions from the experimental studies. While all the input-output and input-intermediate validation results were based on statistically significantly increased or decreased measurements that were subject to type I error, the inhibition experiments also included findings that were not significantly changed. They are subject to a greater likelihood of type II errors in cell biological experiments, which are typically under-powered. Hence, data uncertainty represents a potential source of bias in model validation.

2.2.3.1. Parameter Uncertainty

We quantified the effects of uncertainty in the magnitudes of the model reaction parameters (n, ω, EC_{50} and τ) on the assessment of model accuracy. We repeated the model validation by randomly sampling each of these parameters for each ODE from uniform distributions with mean values that were not necessarily the same as the constant values used in the original validation analysis. Since K and B in the model are nonlinear functions of EC_{50} and n, it was necessary during the sampling process of these two particular parameters to ensure that B>1 so that K is represented by a real number that satisfies the following inequality:

$$\frac{EC_{50}^{n} - 1}{2EC_{50}^{n} - 1} > 1$$

which leads to the following restrictions on these two parameters:

$$n > \frac{ln\frac{1}{2}}{lnEC_{50}}, EC_{50} < 2^{-\frac{1}{n}}$$

Using these constraints, the default Hill coefficient of n=1.4 requires EC_{50}<0.61, and the default half-maximal activation of EC_{50}=0.5 requires n>1.0.

Similarly, the values of both ω and τ were sampled from uniform distributions in the ranges [0.2, 1] and [0.5, 10], respectively. To allow for comparison between uniform and Gaussian

distributions, we calculated the mean and standard deviations of the Gaussian distribution such that ± 2 standard deviations spanned 95% of the range in the uniform distribution.

As in the original report, a threshold change of 0.05 in a network intermediate or output variable was used when comparing between model predictions and experimental results. Parameter perturbations, particularly in ω, that affected the overall input-output gain of the system predictably affected validation accuracy reciprocally with a change in threshold. Therefore, we also analyzed the effects of simultaneously sampling the stretch input and the threshold from uniform random distributions ranging from 0.1 to 0.9 and 0.01 to 0.09, respectively. For each calculation, the analysis of the input stimulus and reaction weight ω were drawn from the same uniform random distributions used above with ranges of [0.4, 1] and [0.2, 1], respectively.

2.2.3.2. Epistemic Uncertainty

Epistemic uncertainty is the uncertainty caused by incomplete of knowledge of the system. Compared with the network components and structure, which are readily appreciated from the experimental literature, the choice of logic that best represents reactions with multiple inputs is more prone to errors of interpretation and the limitations on the ability of a logic-based formulation to properly represent biochemical processes. In this study, 52 of 94 signaling components were regulated by multiple upstream nodes, and these interactions were approximated in the mathematical model using 19 "AND" and 33 "OR" logic gates. To explore the effects of epistemic uncertainty in the model logic, we performed three UQ analyses: First, each "AND" reactions was randomly changed to "OR" with a probability of 0.5; similarly, each "OR" reaction was randomly changed to "OR" with a probability of 0.5; and lastly, we randomly switched the logic sampling from a binomial distribution with a mean probability of 0.5.

2.2.3.3. Data Uncertainty

Finally, we also analyzed the effects of the data uncertainty inherent in all biological experiments on the validation accuracy obtained by comparing the model with the subset of 120 inhibition experiments used for validation. Cell biology studies invariably rely on the conventional statistical threshold (P-value) of $P<0.05$, which corresponds to the risk of making a type I error. But these studies rarely have large enough sample sizes to achieve a comparably low risk β of making a type II error. We reviewed the papers from which the 120 inhibition validation experiments were drawn; they included 106 significantly down-regulated, 10 unchanged and 4 up-regulated responses. Statistical power was rarely reported, so we made use of webplotdigitizer [273-274] and recalculated power from the published inhibition experiments that reported no significant change. Power was in the range of 0.6~0.8 so we chose a value for β of 0.4. UQ was used to measure the effects of statistical uncertainty on model validation accuracy by testing how the model accuracy changed when the published experimental conclusions were randomly overturned. For each of the 110 experiments that showed significantly changed stretch response to an inhibitor, we randomly reassigned each result with a 5% probability of overturning the significant change. We randomly resampled the remaining 10 experiments reporting no significant change, with a 40% probability of reclassifying them to be significantly up- or down-regulated. Since the ratio of decrease vs. increase in the experiments was 106:4, the conditional probabilities of the overturned non-significant experiments being classified as up-regulated was set to 4/110 and down-regulated was set to 106/110.

2.2.4. Uncertainty Quantification Methods

For UQ analysis, we used Monte Carlo (MC) [275] or polynomial chaos expansion (PCE) [271] simulations. PCE is an approximate method that makes use of polynomial expansions to

reduce calculation time significantly over MC simulations provided the number of parameters is not too large [275]. Therefore, here we performed preliminary analyses comparing computed accuracy distributions and computational performance of PCE with MC simulations to determine when PCE could be reliably used to save on computation time without significantly affecting the resulting distribution. We also tested the Markov-Chain Monte Carlo (MCMC) method, an exact Monte Carlo Method that samples the distribution via a stochastic process, to test whether MCMC sampling had any effect on computational cost. While MC simulations typically require a large sample size to account adequately for all possibilities, PCE methods are an efficient and mathematically rigorous strategy for UQ and sensitivity analysis [276] that are typically faster than MC methods when the number of sampled parameters is fewer than 20 and the output has smooth behavior with respect to the input parameters [275].

Previous studies have reported that PCE simulations achieve comparable accuracy to MC simulations and are significantly faster when the number of parameters is fewer than 20 [275, 277-278]. We therefore compared the distributions of simulated model accuracy distributions using PCE, MC and Markov-Chain MC simulations to quantify the effects of parameter uncertainty for different numbers of parameters. Randomly sampling the stretch input variable with all three methods achieved very similar distributions of model accuracy (figure 2.2A) that were not significantly different by Kolmogorov-Smirnov (K-S) test ($P>0.99$ for PCE vs. MC and PCE vs. MCMC). Simulations varying 15 weight parameters also produced distributions of accuracy that were not significantly different by K-S test ($P>0.99$) between order 3 PCE simulation and MC simulations with sample sizes of 3000 and similar computation times for each method (figure. 2.2B). Simulation using order 2 PCE also resulted in distributions that were not significantly different from those with 3000 MC samples ($P>0.95$) but with run times that were 1/5th as long

on average. For more than 20 parameters, PCE simulations took an average of over 3 times as long to compute as comparably accurate MC simulations. K-S tests comparing the accuracy distributions obtained using MCMC simulations showed no significant differences with the results of PCE ($P>0.99$) or MC ($P>0.30$) simulations, though the required number of MCMC model evaluations was slightly lower than for the standard MC approach yet still more than the PCE method required to achieve comparable accuracy. Thus, for all the parameter UQ simulations reported here, we used order 2~4 PCE simulations when the uncertain component size was fewer than 20, otherwise we used MC simulations. We conducted initial simulations sampling from both uniform and Gaussian distributions (figure 2.2D). Since there were no statistically significant differences between the predicted accuracy distributions ($P>0.65$ by K-S test), we used a Uniform distribution as the default statistical sampling distribution for all the UQ simulations reported here, except where specified otherwise (Fig 2.2).

For reaction parameters n, EC_{50}, ω and τ of all 125 reactions, we used MC simulations to sample from uniform random distributions in the following ranges:

$n \sim U(1,3)$,

$EC50 \sim U(0.4, 0.6)$,

$\omega \sim U(0.2,1)$, $\omega \sim U(0.8,1)$,

$\tau \sim U(0.5, 10)$.

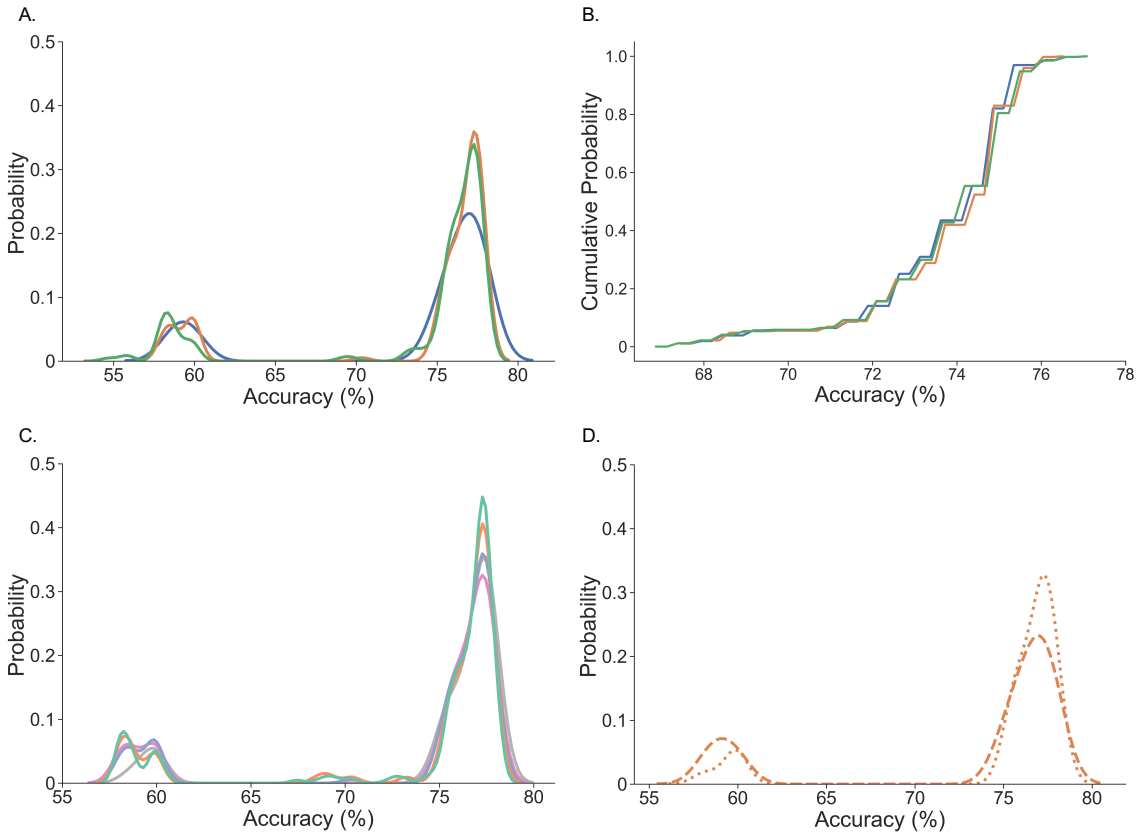

Figure 2.2| Methods and parameters of UQ. (A) Model predictive accuracy distributions computed for univariate sampling of the input stretch using MC (150 samples, in orange), MCMC (150 samples, in green) and PCE (order = 4, in blue) (arrows from top to bottom). (B) Cumulative accuracy distribution due to uncertainty in 20 weight parameters using different UQ methods and a comparable number of model evaluations (green: MCMC with 3000; blue: order 3 PCE; orange: MC with 3000 samples; arrows from top to bottom). (C) Model prediction accuracy distributions computed by MC sampling the input stretch with different sample sizes (sea green: 1000; orange: 400; steel blue: 200; grey: 50; pink: 100; arrows from top to bottom). (D) Model prediction accuracy distributions computed by MC sampling of the input stretch from different random distributions (dotted line: Gaussian distribution; dashed line: uniform distribution; arrows from top to bottom) with a sample size of 40. (Online version in color.)

The ranges of n, EC_{50} and τ sampled for parameter UQ were determined based on values commonly reported in the biochemical literature [172-173] together with mathematical constraints imposed by the model equations to prevent negative function values. Ordinarily, the reaction weights ω would be set at or close to 1 (the original default value was 0.9) unless the effects of an inhibitor, knockout or knockdown were being simulated. Therefore, we sampled ω from U(0.8, 1). Recognizing that this is a narrow range, we repeated the analysis for ω in the range U(0.2, 1). As expected, sampling from a wider range of ω that included lower node weights decreased average model accuracy when maintaining the same threshold. We therefore investigated the extent to which this effect was dependent on the chosen threshold. MC sampling was also used for analyzing uncertainty in the validation data and the model threshold in the range (0.01,0.09). We used MC sampling to quantify the epistemic uncertainty due to the choice of interaction logic by switching AND and OR logic with a random probability of 0.5.

To test whether sufficient parameter combinations were sampled, we increased the sample size in the UQ analysis of ω from 2,500 samples to 100,000. The resulting distributions of model accuracy were not significantly different ($P>0.05$ using Student's t-test).

2.3. Results

2.3.1. Parameter Uncertainty

The effects of uncertainty in the parameters of all 125 reactions on computed model validation accuracy were quantified separately for ω, n, EC_{50}, and τ as shown in Fig. 2.3. Accuracy was generally robust to parameter variation, but most sensitive to uncertainty in ω (Fig. 2.3C) and insensitive to uncertainty in τ (not shown). Most perturbations decreased model accuracy, but some increased it marginally suggesting some potential for model improvement. Uncertainty in the Hill coefficient n and half activation parameter EC_{50} had similar effects on the distribution of

model accuracy. These two parameters of the activation function are coupled numerically and only

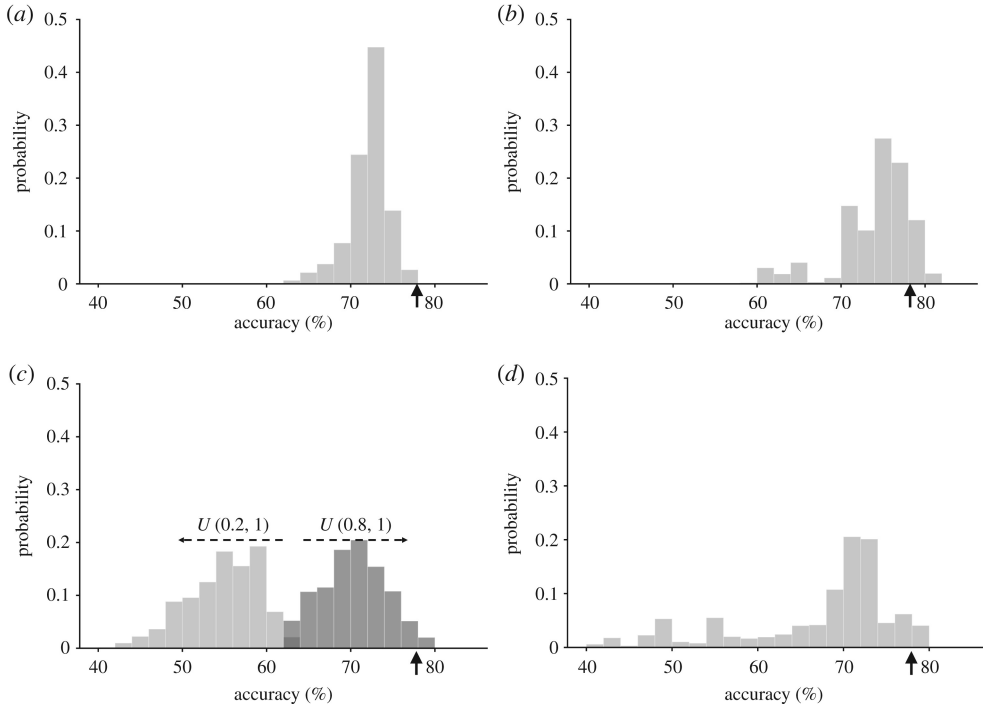

Figure 2.3| Parameter uncertainty quantification. Model predictive accuracy distributions computed for univariate random sampling of uncertainty in reaction parameters: Hill coefficient n (A), half-activation EC50 (B), reaction weight ω (C) and all model parameters combined (D). Vertical arrows indicate original default model accuracy. See text for details.

affect the speed at which signaling molecules reach steady state. Perturbations in τ were not large enough relative to the four-hour time-course of the simulation to affect the steady state results. A global UQ analysis of all the model parameters led to a flatter accuracy distribution than that of the distributions obtained by sampling individual parameters. This distribution was similar to the sum of the individual parameter distributions suggesting that the impact of uncertainty in each individual parameter may be a good indicator of its contribution to the impact of parameter uncertainty in all parameters (Fig. 2.3D).

In assessing the effects of uncertainty in n, EC_{50} and ω, we found that the loss of accuracy was mainly due to changes in the ability of the model to correctly predict the results of inhibition experiments rather than input-output experiments. In the analysis of parameter uncertainty in EC_{50},

the average accuracy of the input-output and input-intermediate validation decreased from 100% to 92% while the average accuracy of inhibitor experiment validations fell from 68% to 33%. For ω sampled in U(0.8,1), mean input-output accuracy only fell to 98% whereas mean inhibition experiment prediction accuracy fell to 29%. This conclusion was also consistent in the global UQ analysis on all parameters where the corresponding decreases were 100% to 60% and 68% to 15%, respectively. It is not surprising that inhibition experiments represent a more stringent test of model accuracy than input-output experiments, but they are also more likely to be subject to experimental error and more sensitive to model perturbations.

Taken together, the importance of the effects of perturbations in the reaction parameters on accuracy (Fig. 2.4A) as estimated by Pearson correlation analysis was not significantly different between the seven major modules of the network: cell surface receptors; the phosphoinositide 3-kinase/protein kinase B (PI3K/Akt) pathway; the mitogen-activated protein kinase (MAPK) pathway; cytoskeletal signaling; calcium signaling; transcription factors; and outputs. For this purpose, reactions were assigned to modules based on the module containing the target of the reaction, not the inputs.

Lower inputs or reaction weights may have reduced validation accuracy by reducing overall system gain causing more responses to fall below the fixed threshold. To test this, we allowed the input to vary randomly from 0.1-0.9 and simultaneously allowed the threshold to vary randomly from 0.01-0.09. The contours of constant accuracy on the input-*vs.*-threshold plane (Fig. 2.4B) show that decreases in model accuracy due to decreased input stretch could be partially offset by decreasing the threshold for categorizing an output of the model as significantly changed. Consequently lowering the threshold increased mean accuracy (Fig. 2.4C).

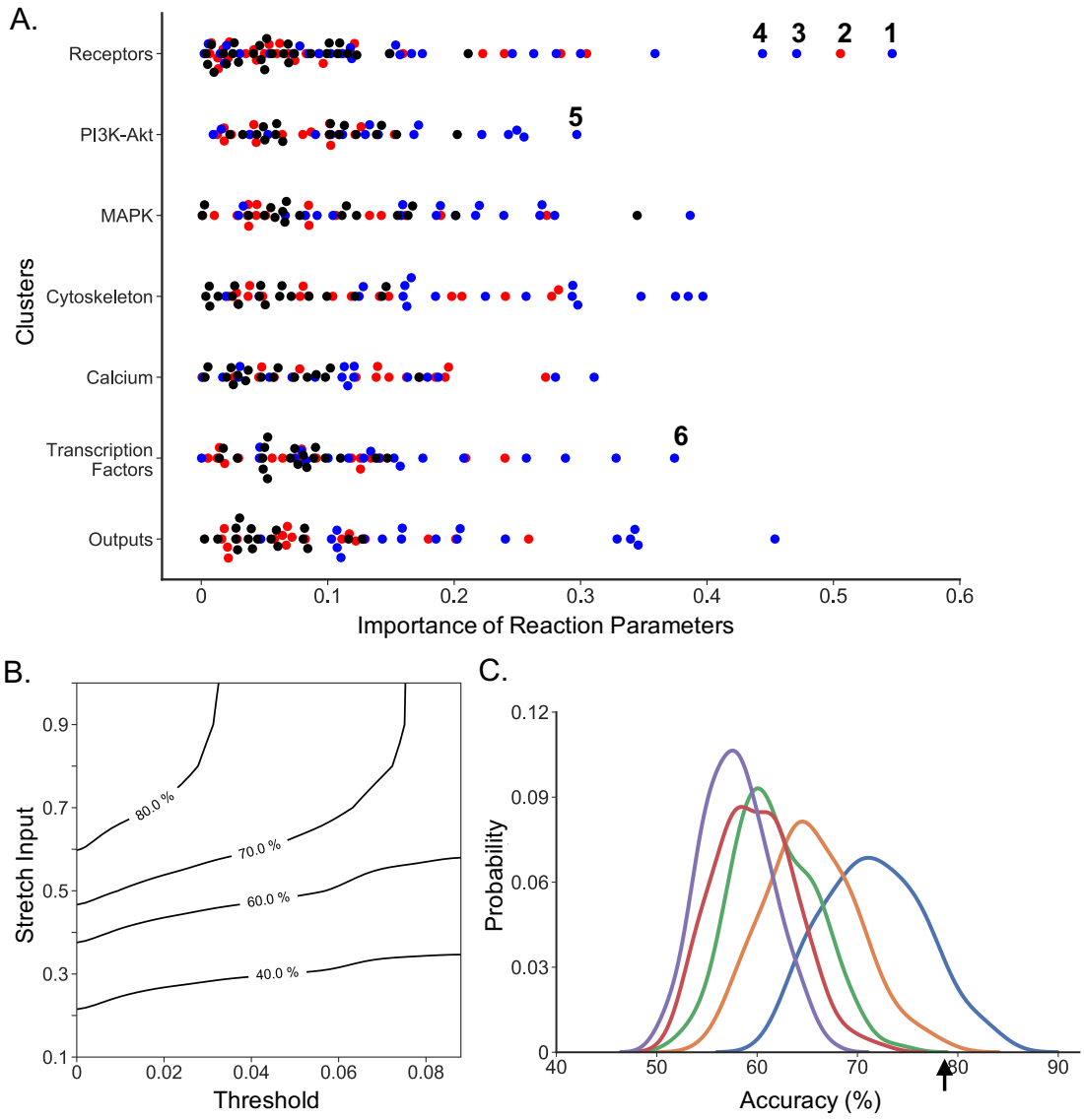

Figure 2.4| Analysis of parameter importance and the effects of model threshold. (A) Importance analysis of reaction parameters ω (light grey), EC50 (dark grey) and n (black) by network module calculated using Pearson correlation of parameter variations with accuracy. Outlying reactions with the highest importance tended to be input or output reactions and included the reactions that activate endothelin-1 (1) and the endothelin-1 receptor (2), integrins (3), angiotensin II (4), phosphoinositide 3-kinase (5) and the skeletal α-actin gene (6). (B) Relationship between the effects of input and weight uncertainty and threshold uncertainty on accuracy contours. (C)Effects of varying model prediction threshold (between 0.09 purple, 0.07 red, 0.05 green, 0.03 orange and 0.01 blue, arrows from left to right) on accuracy distributions due to uncertainty in input and reaction weights. Vertical arrow indicates original default model accuracy. (Online version in color.)

2.3.2. Model Logic Uncertainty

We examined the individual impact of model logic uncertainty for the 19 reaction combinations with "AND" logic and 33 interactions with "OR" logic on validation accuracy. As seen in Fig. 2.5A, switching model logic could greatly reduce accuracy, with changing "OR" to "AND" interactions causing much larger reductions that switching "AND" reactions to "OR" logic.

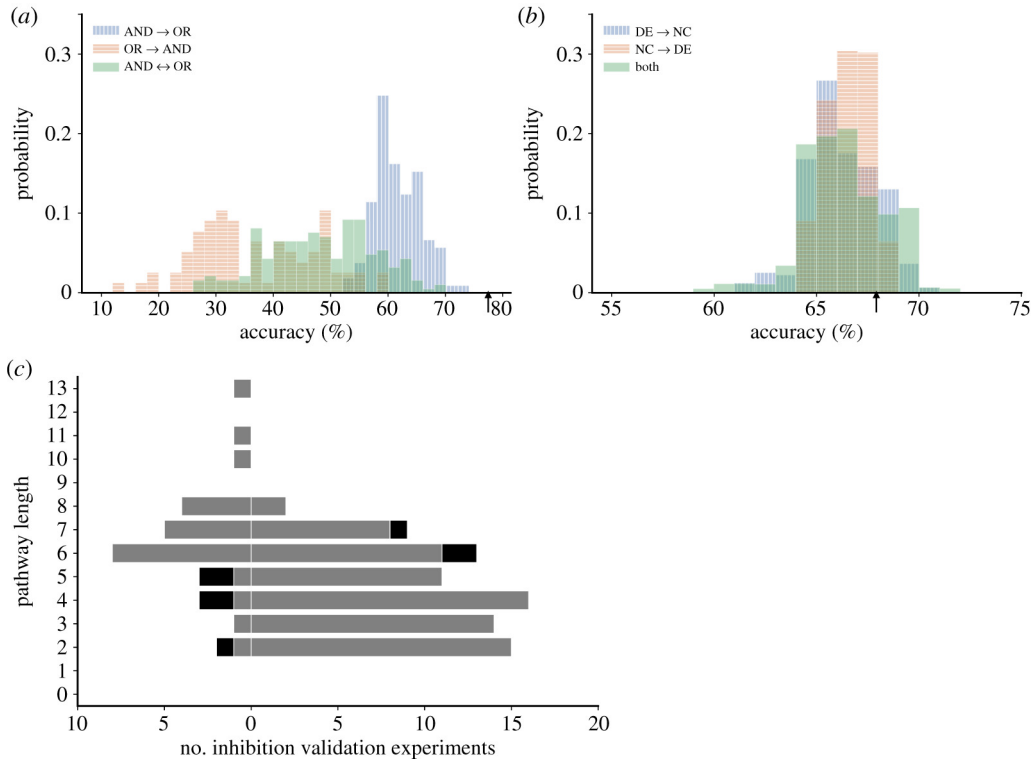

Figure 2.5| Analysis of uncertainty in reaction logic and validation. (A) Effects on model validation accuracy of randomly changing 'AND' logic to 'OR' logic (blue |), 'OR' reactions to 'AND' logic (orange -) or both (green), all with a probability of 0.5. (B) Effects of data uncertainty on model validation accuracy assessed only using reported inhibition experiments [12], for which the original accuracy was 67%. Effects on accuracy of changing significantly changed (SC) validation measurements to no change (NC) with a probability α of 0.05 (blue |). Effects of changing NC to SC with a probability β of 0.4 (orange -). Combined effects of both random changes (green). (Vertical arrows indicate original default model accuracy). (C) Effects on model accuracy of the length of the pathway between the inhibited node and the measured response node in the inhibition validation experiment [2]. Values to the left represent incorrect model predictions and values to the right represent correct predictions. Light grey represents model predictions of no change and black represents model predictions of significant change. (Online version in color.)

A step-wise regression analysis of all the "AND" logic interactions and a statistical analysis correcting for multiple comparisons (Benjamin-Hochberg false discovery rate) showed that predictive accuracy was significantly affected ($P<0.05$) by the logic choice of 12 of the 19 "AND" interactions (Table 2.1). Switching all 12 interactions from "AND" to "OR" would decrease model accuracy from 77.9% to 56.4%. Eight interactions were highly significant ($P<0.01$); they are all either output nodes of the system such as B-type natriuretic peptide (BNP), cell area, β-MHC, connexin 43 (Cx43) or particularly well-known regulators of mechanotransduction signaling such as focal adhesion kinase (FAK), protein kinase C (PKC), extracellular-regulated kinases (ERK1/2), and calcineurin (CAN). The "AND" interaction between the reactions activating the muscle LIM-domain protein (MLP) was the only one to have a negative coefficient in the regression analysis suggesting that switching this "AND" logic to "OR" resulted in a slight improvement in accuracy. Reformulating the network by changing the interaction logic of the reactions activating MLP increased model accuracy by 1%. For the inhibition validation experiments, the original model predicted that MEF2 gene expression was only reduced by 8% when PKC was inhibited compared with approximately 100% block in published experiments [102, 104]. Changing the logic by which PKC and calcium-calmodulin kinase (CaMK) regulate histone deacetylase 4 (HDAC4) from "AND" to "OR" increased the inhibitory effect of PKC blockade on MEF2 to >20% and significantly improved model accuracy by >5%.

Table 2.1| Regression analysis on perturbation of reaction interaction logic

Output node	Estimate	s.e	Pr(>|t|)
BNP	0.095	0.025	0.0003
β-MHC	0.093	0.025	0.0004
CaN	0.093	0.027	0.0008
Cx43	0.085	0.025	0.0012
CellArea	0.086	0.027	0.0017
FAK	0.084	0.026	0.0018
PKC	0.080	0.026	0.003
ERK12	0.075	0.026	0.005
HDAC	0.067	0.025	0.010
PrSynth	0.062	0.026	0.019
CREB	0.060	0.025	0.019
sACT	0.059	0.025	0.022
ANP	0.049	0.025	0.054
SRF	0.052	0.027	0.056
IP3	0.045	0.028	0.107
Ao	0.039	0.025	0.127
FHL2	0.040	0.027	0.131
MuRF	0.016	0.026	0.538
MLP	-0.002	0.028	0.932

2.3.3. Data Uncertainty

The final source of uncertainty we investigated was statistical uncertainty in the experimental results of the inhibitor studies used to validate the model. In particular, while 110/120 of the published validation experiments reported a significant change in intermediate or output due to inhibitor treatment, 10/120 reported no change. However, the uncertainty inherent in the unchanged responses was 4-8 times higher than the uncertainty in significantly changed responses because the conventional choice of α ($P < 0.05$) is much lower than β in the cell biological experiments, which are invariably under-powered owing to small sample sizes. Overall, data uncertainty had a limited impact on model accuracy; the original baseline inhibition accuracy was 68% and accuracy in almost all the UQ simulations was between 60% and 70% (Fig. 2.5B). The

number of validation comparisons that would have been reversed by switching validation results from significant to unchanged was approximately the same as if the validation finding had been switched from unchanged to significant. Overall though, switching unchanged findings to changed led to a higher mean accuracy. This suggests that better powered experimental studies may be justified for experiments designed to test significant model-predicted responses to inhibitors that had no observed statistical effect in published experimental studies.

The accuracy with which the model correctly predicted the results of inhibitor experiments depended on the length of the pathway between the inhibited node and the readout node. For pathway lengths exceeding five, prediction accuracy decreased markedly (Fig. 2.5C).

Pathway analysis of the 120 inhibition experiment node pairs revealed 11 node pairs that were not connected in the network with the result that only 2 of these 11 experiments, ET1R/STAT and PI3K/JNK, could possibly have been correctly predicted by our model. For the other 9 node pairs, we examined the original experimental studies and found there was either a lack of corroborating data [279-282], evidence of pathway crosstalk (e.g. between PI3K and Ras or Src and FAK) that was not represented in the original model [283-285] or contradictory data in subsequent publications [1]. In the other 109 node pairs, pathway analysis suggested that the longer the pathway (above 6 steps) between inhibited node and readout node, the higher the probability that the model would predict no change. This difference was mainly caused by the accumulated loss of activity values and a consequent decrease in likelihood that the model would reach the threshold for significant change with a consequent decrease in model accuracy.

[1] This exercise also caused us to identify a typographical error in Fig. 3 of our original model paper [172], which should have indicated that stretch decreased rather than increased MuRF translocation to the nucleus both in the experimental study and the model. This error did not affect the model results or accuracy

2.4. Discussion

In this study, we explored the effects of uncertainty in parameters, model logic and experimental validation data on estimates of prediction accuracy by a published network model of mechanosignaling pathways in ventricular myocytes [172]. Model prediction accuracy was fairly robust to moderate uncertainty in network reaction parameters, but large decreases in model reaction weight did significantly impair accuracy. However, this was largely attributable to a reduction in overall system gain that could be compensated by a corresponding decrease in the threshold used to classify a particular model output as changed or unchanged for the purposes of comparison with experimental observations.

In contrast to parameter uncertainty, epistemic uncertainty analysis showed that model accuracy is more vulnerable to uncertainty in the choice of reaction logic. Randomly replacing "AND" logic reactions with OR logic had modest effects on accuracy, but the converse greatly reduced it. In the original publication, it was concluded that changing all logic to "OR" type lowered the model performance if effects of varying stretch input and reaction weights were kept unchanged as studied in the original paper. Thus, there may be opportunities to improve model predictive accuracy and reliability by performing new experiments that can more confidently identify the most appropriate reaction logic. For example, we found that changing the interaction logic by which PKC and CaMK regulate HDAC4 from "AND" to "OR" increased the inhibitory effect of PKC blockade on MEF2 and significantly improved model accuracy. However, neither choice resulted in close quantitative agreement with experiments. The mechanisms by which different kinases and phosphatases regulate nuclear translocation of HDACs where they alter chromatin structure and gene expression are complex. They involve the successive phosphorylation of multiple residues that are targets of multiple kinases and phosphatases and

could be cooperative [286]. A more complete investigation of uncertainty in the network structure could have been achieved by also completely removing reactions or adding new ones. However, determining which new reactions to be added to the model requires developing an improved model with more reactions. The effects of removing nodes were approximated when we sampled from a wider range of reaction weights since lower weights had the effect of rendering reactions ineffective at changing downstream node values enough to exceed the threshold for classifying them as significantly changed. Hence, it is not surprising that the resulting biochemical interactions may not be accurately approximated by a single logic gate. Therefore, improving quantitative model predictive accuracy and reliability may require a combination of reaction parameter and logic or the inclusion of additional types of reaction equations that more accurately approximate biochemical mechanisms.

Most combinations of parameter, data or logic perturbations tended to decrease the prediction accuracy compared with the default model accuracy. This is not unexpected given that the data and logic choices by default in the original model were based on published experimental literature that we expect to be correct substantially more often than not. Similarly, while the original default model parameters were not optimized, they were based on prior published knowledge and hand tuned to give expected levels of network activity. Given this, a more rigorous approach to determining the distributions in Section 2.2 could be to compute posteriors for the parameters and the model in a Bayesian setting and use those posteriors in place of the distributions described. Perturbations to parameters and reaction logic more often caused decreases than increases in output values. This difference was mainly due to the accumulated loss of activity values and thus a decrease in likelihood that the model would reach the threshold for significant change leading to a decrease in model accuracy. Particularly for ω, large variations could cause

large decreases in accuracy. However, these parameters are normally set to 1 or close to 1 (0.9 by default) unless the reaction is being pharmacologically or genetically inhibited. Moreover, some of this loss of accuracy could be offset by a corresponding adjustment of the threshold for categorizing a model output as changed or unchanged. For realistic ranges of ω and all other model parameters the accuracy of model predictions was generally robust.

Finally, data uncertainty due to the risk of type I and type II errors in experimental data did not significantly affect estimated model accuracy. Interestingly, the higher uncertainty due to low power in the small fraction of inhibitor experiments with no significant change was less likely to decrease model accuracy than the much lower uncertainty associated with the larger number of experiments resulting in a statistically significant change. False positive model predictions could be worth investigating further by repeating previously reported experiments with larger sample sizes and statistical power.

In this study, we use two different UQ sampling methods: Monte Carlo simulations and polynomial chaos expansions. The latter method produced equivalent distributions of accuracy with less computational cost than the former when fewer than 20 parameters were being sampled and was over ten times faster for ten or fewer parameters. We also found that sampling reaction parameters from uniform distributions yielded very similar findings to those obtained when the uncertainty was Gaussian. In our analysis, we found a numerical error rate of up to ~10% because some extreme combinations of parameters could force the system to limit and increase the stiffness of the system of ODEs.

2.5. Conclusion

Quantification of the effects of uncertainty in model parameters, logic and validation data on the estimated accuracy of an ODE network model of the ventricular myocyte mechano-

signaling network showed that the model was robust to parameter and data uncertainty but more vulnerable to errors in the choice of logic used to represent biochemical interactions between interacting biochemical species. In particular, incorrect interpretation of experimental data to represent "AND" reaction logic can significantly decrease prediction accuracy. The findings of this UQ analysis point to opportunities for model parameter refinement and extension of model pathway structure and logic, and for new experimental measurements that improve the power of statistical conclusions.

2.6. Acknowledgements

We appreciate the help of Dr. Kevin Vincent in testing the python implementations.

Chapter 2, in full, is a reprint of the material as it appears in Philosophical Transactions of the Royal Society A 2020. Cao, Shulin; Aboelkassam, Yasser; Wang, Ariel; Valdez-Jasso, Daniela; Saucerman, Jeffery J.; Omens, Jeffery H. McCulloch, Andrew D. The dissertation author was the primary investigator and author of this paper.

Chapter 3: Fiber and Transverse Stretch Mediate Differential Transcriptional Responses in Mouse Neonatal Ventricular Myocytes

3.1. Introduction

In the heart, hemodynamic overload can induce different modes of ventricular hypertrophy and remodeling, and may be associated with distinct multiaxial mechanical stimuli [11, 287-288]. Several cell signaling pathways and mechanisms have been implicated in the myocyte hypertrophic response to mechanical loading and stretch [8, 10, 289], but little is known about the specific pathways and mechanical stimuli that mediate direction-dependent responses, for example, predominant myocyte lengthening during ventricular volume overload [290]. The internal organization of the sarcomere and cytoskeleton suggests that myocytes may respond differentially to loading applied either parallel or transverse to the long axis of the cell. In micropatterned, elongated neonatal rat cardiac myocytes, phenotypic responses to 24 hr of static stretch differed significantly when stretch was applied primarily along the cell axis compared with transverse to it [262-263].

Previous studies have shown that longitudinal (along the myofilament axis) uniaxial stretch of aligned neonatal rat ventricular myocytes induced the addition of new sarcomeres in series, so that by six hours the original unstretched sarcomere length had been restored [264]. Hence, the hypertrophic signaling and remodeling responses to stretch in neonatal myocytes in vitro are likely quite rapid. Many studies have also shown evidence of paracrine and autocrine responses to stretch that act over short and longer-term time scales [265]. Therefore, the first goal of this study was to examine differential gene expression profiles following up to 4 hr of stretch in micropatterned

neonatal mouse cardiac myocytes and compare responses when the cells are stretched primarily along or transverse to their long axes.

To elucidate the differential transcriptomic responses to longitudinal vs. transverse stretch, we expanded a previous logic-based computational model of the cardiac myocyte mechanosignaling network [172] by incorporating transcriptional control of 772 genes shown to be regulated by the 11 transcription factors (TFs) in the signaling model. In the signaling model, stretch can modulate pathways downstream of mechanically sensitive membrane receptors and channels. Differential gene expression predicted by the model showed 69% agreement with the gene expression measurements after 4 hr of longitudinal stretch and 72% agreement with genes that were significantly different. To further examine axis-dependent genetic signaling pathways, we used the signaling model to detect axis-dependent receptor-mediated pathways, and then performed receptor blocking studies in culture to validate those findings, implicating AT1 and ET1 receptors and their downstream signals to be important in the response to both transverse stretch and longitudinal stretch. The model results did not indicate different signaling pathway activation to different directions of stretch, but we found that the main difference between transverse and longitudinal stretch responses may be due to sensitivity differences to the direction of stretch. Finally, pathway analysis applied to the systems network found a key subnetwork of the genes, which are targets of 9 TFs, and are regulated by stretch via 16 signaling molecules including the MAPK signaling pathway.

3.2. Methods

3.2.1. Micropatterning, Isolation and Culture

Cardiac myocytes were cultured on flexible, micropatterned elastomeric substrates and subjected to a static mechanical load using methods described previously [291]. Briefly, Sylgard

186 polydimethylsiloxane (PDMS) membranes were spin-coated on silicon wafer master molds micropatterned with SU-8 2005 negative photoresist using a custom photomask, degassed, and cured at 70°C for 30 minutes and then at room temperature overnight. The resulting 10 μm wide microgrooves were 5 μm deep and 10 μm apart. The micropatterned membranes were mounted in custom elliptical cell stretchers and coated with murine laminin at 10 μg/ml in phosphate buffered saline (PBS). Excess protein was removed by rinsing twice in 1X PBS prior to plating cells.

Cardiac myocytes were isolated from 1–2 day old C57BL/6 mouse hearts as described previously [292]. Cells were plated on the PDMS membranes in the stretchers at a density of 1.5-2 million cardiac myocytes in an area of approximately 600 square mm per stretcher. The cell media consisted of Dulbecco's Modified Eagle Medium and Medium 199 supplemented with 10% horse serum, 5% fetal bovine serum, 100 units/mL penicillin, and 100 μg/mL streptomycin, and incubated at 37°C with 10% CO_2. At 72 hr after plating, media was changed to a serum-free media, and the cells were cultured for another 24 hr prior to stretch, taking on an aligned, rod-like morphology.

3.2.2. Stretch and RNA-Seq

The elliptical stretchers applied an anisotropic, biaxial strain to the membrane of 14% along the minor axis of the ellipse and 3.6% along the major axis [291]. Membranes were oriented during assembly into the stretcher so that cell alignment would be parallel to either the minor (longitudinal stretch) or the major axis (transverse stretch). Two stretch durations, 30 min and 4 hr, and both axes of major stretch were studied with unstretched cells on similar engineered substrates used as a control, for a total of five groups. Three stretchers for each condition served as biological replicates. Total RNA was extracted using an RNeasy Mini Kit.

Total RNA samples were tested for quality using an Agilent Technologies 2100 Bioanalyzer. RNA samples were prepared for sequencing with the TruSeq RNA Sample Prep Kit v2 according to manufacturer's instructions and then sequenced with an Illumina HiSeq 2000. Quality analysis was performed using FastQC [293]. Low quality reads and adapter sequences were trimmed with FASTQ trimmer in the FASTX-Toolkit (supplement S3.1) [293], aligned to mm9 mouse genome with HiSat2 [240]. Featurecounts was used to count aligned reads, and DESeq2 was used to perform the differential expression testing by comparing abundance of gene expression in each stretch condition to the control condition [242, 248]. The adjustments for multiple comparisons were then performed using the method described by Benjamini and Hochberg [254]. Genes with a false discovery rate (FDR) < 0.05 and a minimum $\log_2$ fold change ($\log_2$ FC) of 0.5 with respect to control were defined as differentially expressed (DE). The RNA-Seq data was deposited at the GEO website, accession number GSE83655.

Power analysis was conducted on the RNA-Seq data. To filter out genes with low expression, only genes with greater than 1 count for each sample were kept. The average number of counts per gene and the biological coefficient of variation for all genes were calculated in edgeR [249]. These values along with an FDR of 0.05 and a minimum $\log_2$ FC of 0.5 were taken as inputs into the R package rnaPower, which was used to calculate power [295].

3.2.3. Gene and Pathway Enrichment Analysis

Functional and pathway enrichment analyses was performed by comparing DE genes with the Kyoto Encyclopedia of Genes and Genomes (KEGG) databases. DE genes were categorized into lists of genes for each stretch condition. These lists were analyzed by David, which identified enrichment of genes in pathways [296]. The criteria for classifying a term as enriched were P-value < 0.05 and number of DE genes > 2.

3.2.4. Reverse Transcription Polymerase Chain Reaction

RT-PCR was used to validate representative RNA-seq results and in receptor blocking studies. RNA was quantified using Qubit 2.0 and the Qubit Broad-Range RNA Kit. cDNA synthesis was performed using an RNA input of 500 ng per reaction and a ProtoScript First Strand cDNA Synthesis Kit. Reverse Transcription Polymerase Chain Reaction (RT-PCR) was performed on a Life Technologies StepOnePlus Real-Time PCR System using a KAPA SYBR Fast Universal qPCR Kit. Glyceraldehyde 3-phosphate dehydrogenase (GAPDH) or 18s ribosomal RNA are both housekeeping genes used as the reference gene for fold change normalization. Primers for RT-PCR were listed in supplement S3.2.

3.2.5. Inhibitor Studies of Mechano-Sensitive Receptors

In order to test the predictions from the network model, cell stretch experiments in the presence of pharmacological inhibitor combinations were performed. Cells were divided into three treatment groups: Group 1 inhibited AT1 and ET1 receptors with 1 μM Losartan/100 μM BQ123/10 μM BQ788, 30 min before stretch, Group 2 blocked L-Type Calcium Channels (LTCC), Sodium Hydrogen Exchangers (NHE), and Transient Receptor Potential (TRP) channels with 1 μM Ruthenium Red/5 μM Nifedipine/10 μM HOE642 (Cariporide), 10 minutes before stretch. Group 3 served as a vehicle control for 4 hr for both Groups 1 & 2 4 before stretch and were treated with vehicle controls for each compound as follow: 4 hr before stretch Group 3 was given 2 μL DMSO, 30 minutes before stretch Group 3 received 50 μL dd H_2O and 2 μL DMSO, 10 minutes before stretch Group 3 was given 2 μL dd H_2O and 4 μL DMSO. Half the cultures in each group were stretched in a primarily transverse direction (14% transverse stretch, 3.6% longitudinal stretch) and half were not stretched (unstretched control). All stretchers were then incubated for 4 hr at 37^{o}C, 10% CO_2 and 100% humidity. All compounds remained in culture

during stretch. Cells were then rinsed with room temperature 1X PBS and lysed using Qiagen's RNeasy Mini Kit (# 74104) protocol, using beta-mercaptoethanol in the RLT Buffer.

3.2.6. Computational Mechanosignaling Network

To investigate the roles of mechanosignaling pathways in regulating changes in gene expression in response to anisotropic stretch of ventricular myocytes, we extended the MSN model to include transcriptional regulation and expression of genes downstream of the 11 transcription factors in the previous model [172-173, 297]. We classified 772 putative target genes [224, 228-229, 298-299] that were also detected in our RNA-seq measurements according to three criteria corresponding to different levels of experimental validation: (I) 288 genes for which transcriptional regulation has been confirmed in experiments in mice or rats; and (II) 561 genes for which regulation of the target gene by the transcription factor has been predicted using bioinformatics based on DNA binding sites from published ChIP-seq datasets or confirmed in experiments in mice or rats (supplement S3.3). Of the 772 target genes, 14 encode for an upstream protein in the signaling network. Therefore, the feedback pathways were included to represent protein translation for each of these nodes (supplement S3.3). Seven distinct classes of nodes are seen in this expanded network model (Fig. 3.1), which were rendered with the aid of Cytoscape [300]: membrane mechanoreceptors or mechanosensitive nodes are at the top; four different canonical signaling pathways are activated by the mechanoreceptors (calcium signaling, MAPK, PI3K-Akt, and cytoskeletal-related); these pathways converge onto 11 TFs which regulate the expression of the target genes, of which only the 14 genes that feed back into the network are displayed in Fig. 3.1. These foundational pathways were also found to be the enriched KEGG pathways under the 4 hr stretch.

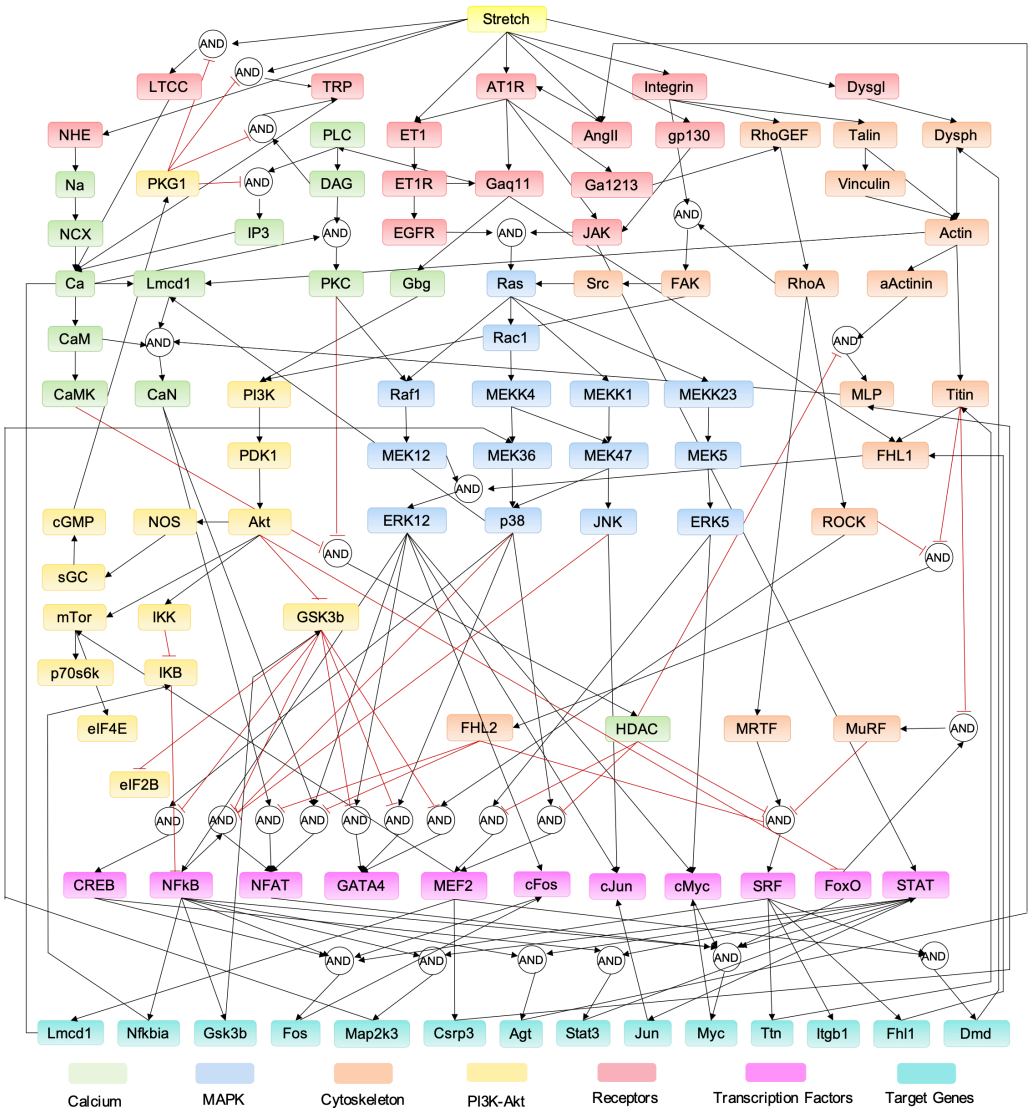

Figure 3.1| Reconstruction of the mechano-signaling network in cardiomyocytes. The model comprises 921 activating or inhibitory reactions linking 84 signaling nodes with 772 genes, beginning with 9 mechano-sensors (NHE, LTCC, TRP, ET1, AT1R, AngII, gp130, Integrin, and Dysgl) and proceeding through multiple signaling cascades and 11 transcription factors (in pink) to 772 gene products including 14 translation feedback paths. Complete lists of genes, model reactions and abbreviations for node names are provided in supplement S3.3.

To numerically simulate the effects of stretch on cardiomyocyte, a small stretch stimulus (0.315) was first used by running the Hill model and mass-action method as described in section 1.2 and 1.3 [173] to a numerical steady-state in order to mimic cellular steady state, which generated the control values of signaling molecules and the gene normalization constants. Then, a

stretch input of 0.7 was applied to the system to simulate gene expression with a time course of 4 hr. A linear regression with a fixed intercept of 0 was conducted by comparing RNA-Seq measurements and model simulation at 4 hr.

Default parameter values (specified in supplement S3.3, weight = 0.9, n = 1.4, and EC_{50} = 0.5) except τ were used for all reactions. Initial gene expression values were derived from the control group of the RNA-Seq data without stretch. Kinetic parameters for target genes were determined using an mRNA half-life (HL) database [230]. HL was converted to the time constant τ using the formula:

$$\tau = \frac{HL}{ln2}$$

For all other nodes, τ = 30 seconds was used. This time constant allows ERK1/2 and p38 MAPK to reach peak activation by 10 minutes of stretch, which matches previous data that maximal phosphorylation of ERK1/2 and p38 MAPK is induced by 10 minutes of stretching [230].

3.2.7. Network Centrality Analysis

In biological network systems, centrality analysis has been used to find the most important biological nodes based on network topology [301]. For a given network composed of multiple signaling nodes and pathways, a sub-network can be formed between any two nodes of interest (starting point is defined as 's' and ending defined as 'e'). The betweenness centrality is a function which assigns a numerical value to every node (m) in this sub-network that monitors the communications between 's' and 'e' [301-302]. Let σ_{se} denote the number of shortest paths from 's' to 'e', then $b_{se} = \sigma_{se}(m)/\sigma_{se}$ is the probability of this node m falls on the randomly selected shorted path between 's' and 'e' [301]. The overall betweenness centrality of this node m in this network will be: $C_B(m) = \sum b_{se}(m)$. This value ranges between 0 and 1; the higher the value, the greater the importance of this node in the sub-network. For example, in a regulatory network

starting from stretch and ending at a gene, if the betweenness centrality of a node in this network is greater than 0.5, more than half of the pathway flows will go through this node and suggests that the node is important in the regulation of the gene.

3.3. Results

3.3.1. Transcriptome and Pathway Enrichment Analysis

The principal stretch axis was aligned either parallel, representing longitudinal stretch, or perpendicular, representing transverse stretch, to the cardiac myocyte orientation on the micro-grooved substrates. A total number of 562 genes with significant changes in expression ($FDR \leq 0.05$ & $|\log_2 FC| \geq 0.5$), as measured by RNA-Seq, were identified from all stretch conditions supplement S3.4. Of these differentially expressed (DE) genes, 557 were significantly changed after longitudinal stretch (40 at 30 min and 527 at 4 hr), 30 were differentially expressed after transverse stretch (17 at 30 min and 13 at 4 hr) (Fig. 3.2A). By far the greatest response was due to longitudinal stretch, which accounted for 99% of all differentially expressed genes in the

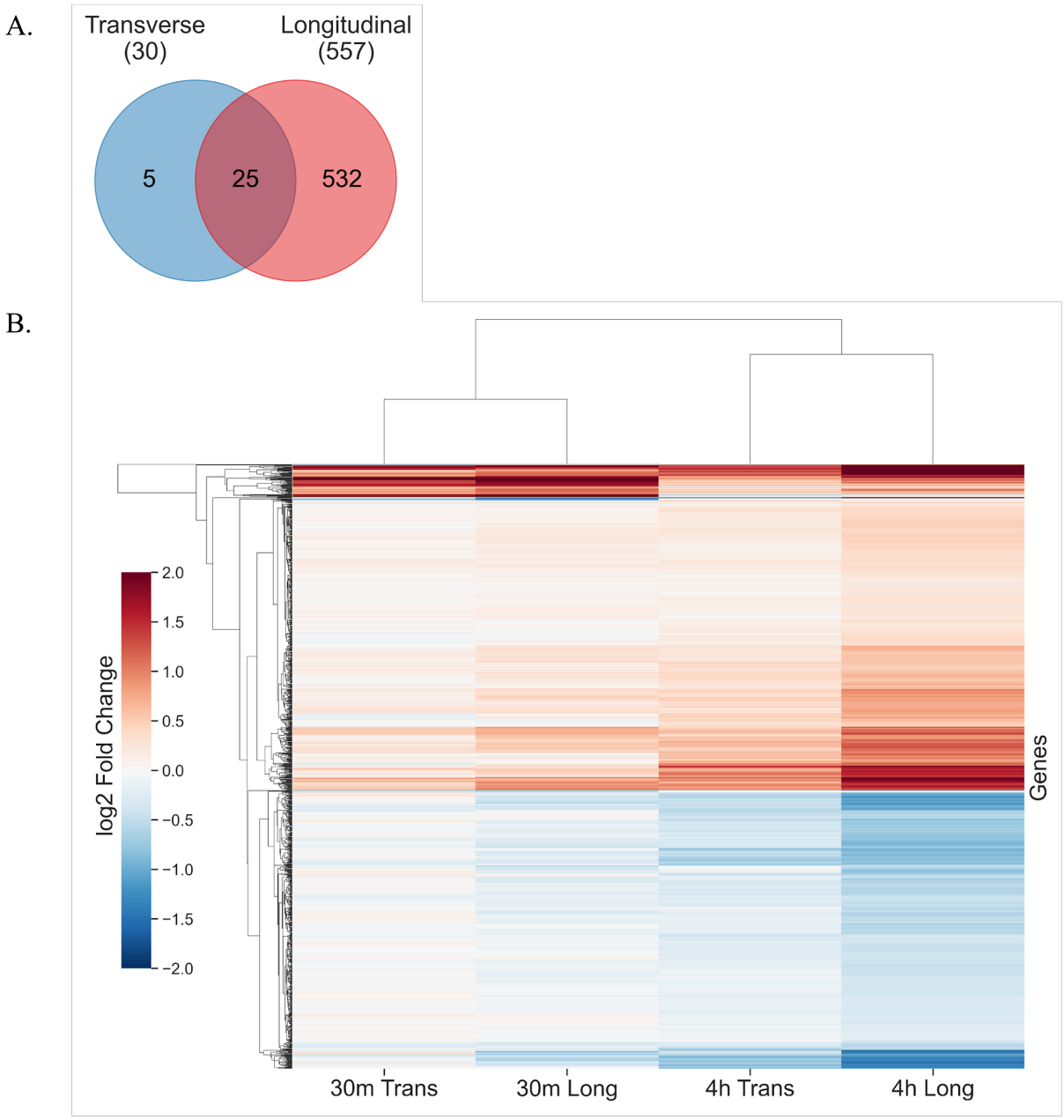

Figure 3.2| An overview of DE genes from RNA-Seq measurements. (A). Venn diagram showing the number of DE genes across multiple stretch conditions: 30 min stretch (Blue); 4 hr stretch (Red). Longitudinal stretch induced ~20 times more genes than transverse stretch. (B). Clustering dendrogram of DE genes based on expression profiles (log_2 FC) using Pearson Correlation under longitudinal stretch. Most genes follow a monotonic change with time while some 10% and 5% of genes perform higher order dynamics respectively under transverse stretch and longitudinal stretch.

experiment compared with the response to transverse stretch which induced only 5% of the differentially expressed genes.

A clustering analysis was performed on the RNA-Seq data (FDR≤0.05 under either stretch condition, on a total number of 1042 genes) and showed several different expression patterns in Fig. 3.2B. These patterns mainly include genes that were highly stimulated at 30 min then returned to control at 4 hr and genes that were stimulated at 30 min and remained stimulated at 4 hr for both types of stretch. The condition-wise clustering suggests that transverse stretch induced similar regulation patterns to longitudinal stretch from 30 min to 4 hr, while longitudinal stretch induced a larger response in gene expression compared with transverse stretch at both 30 min and 4 hr. Among these 1042 genes, sixty genes were induced at 30 min but then dropped at 4 hr under transverse stretch while these genes were further stimulated under longitudinal stretch. Another 33 genes were activated at 30 min and then reversed at 4 hr for both types of stretch. These genes with these higher-order dynamics were further verified as immediate early genes (IEGs).

The expression of representative genes from six of these clusters was validated at 30 min and 4 hr using RT-PCR (Fig. 3.3). The measurements agreed closely, with a Pearson correlation coefficient of 0.97.

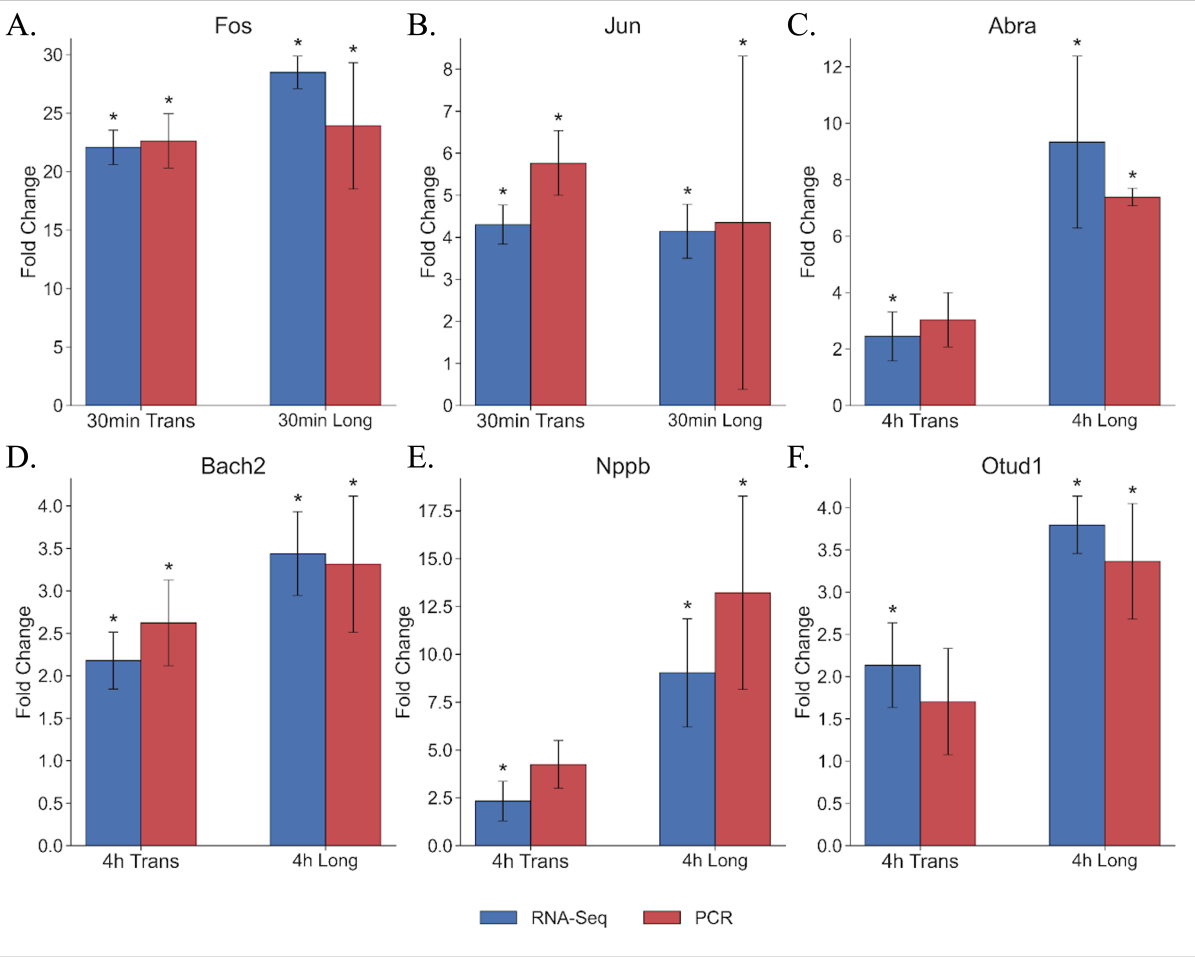

Figure 3.3| PCR Validation of 6 DE Genes in comparison of RNA-Seq Measurements. PCR measurement is represented with color read and RNA-Seq measurement is represented with color blue. Fos and Jun displayed more than 20 and 4 fold changes at 30 min stretch but fell back to near control at 4 hr. Abra, Bach2 and Otud1 showed steady increase in activity along with time from 30 min to 4 hr. Nppb underwent steady increase under longitudinal stretch, which was first highly activated but dropped back to control level under transverse stretch.

Fig. 3.4 shows a subset of the enriched pathways from the KEGG database. It is notable that far more pathways were enriched at 4 hr stretch compared with 30 min. Among all the enriched pathways, the MAPK signaling pathway was activated as early as 30 min. Among the genes that enriched the MAPK signaling pathway, a few genes were IEGs as clustered in the previous clustering analysis. Other pathways, such as the Ras signaling pathway, the PI3K-Akt signaling pathway, the calcium signaling pathways and regulation of actin skeleton, were mainly enriched

at 4 hr. These results also validate our previously published cardiac MSN model [172] that most foundational pathways used to build the model were also enriched in this analysis.

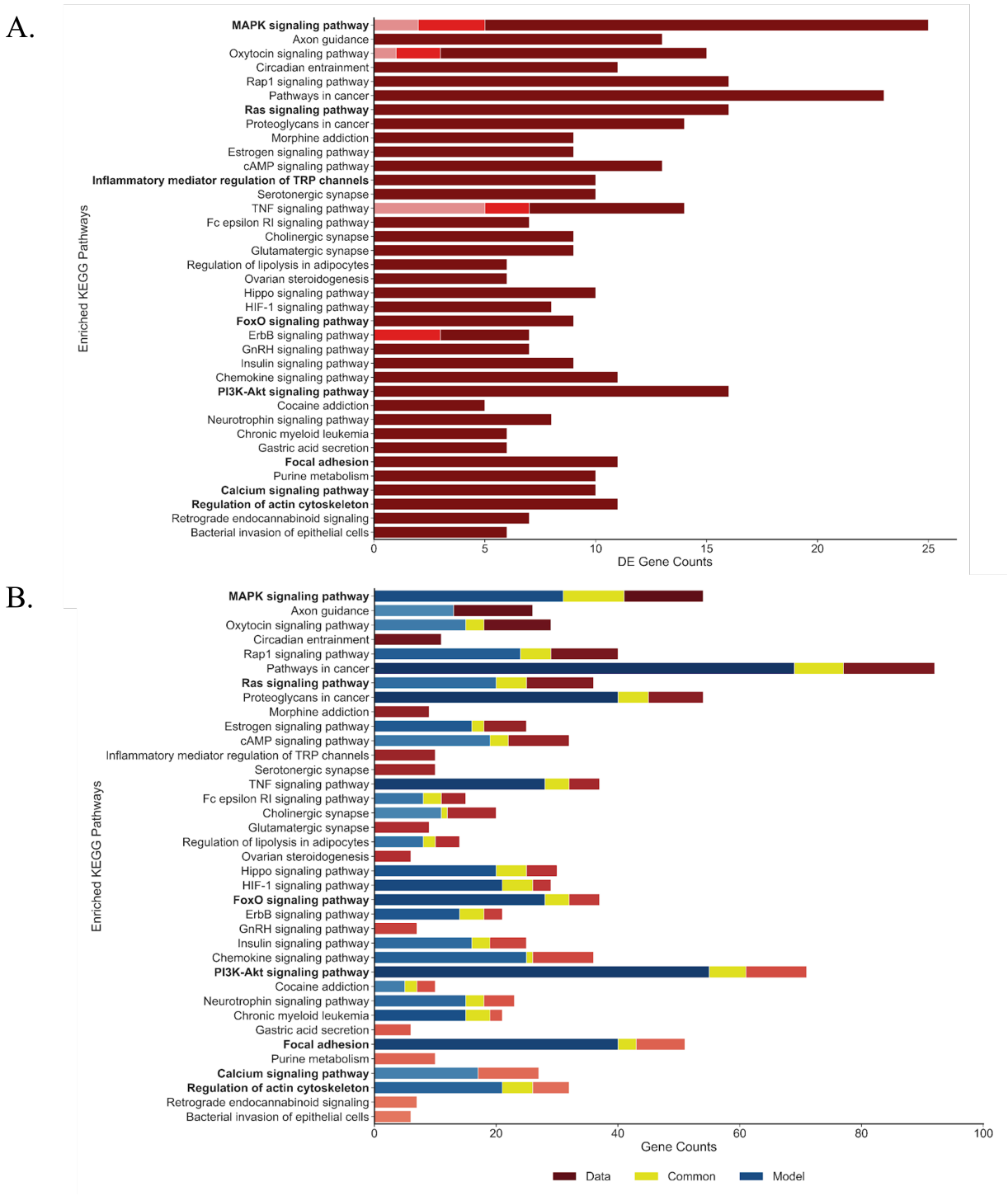

Figure 3.4| KEGG Pathway Enrichment Analysis. (A) KEGG enrichment analysis from DE genes in RNA-Seq measurements in the following categories: pathways enriched at 30 min stretch (light red); pathways enriched at both 30 min and 4 hr stretch (red); pathways enriched at 4 hr stretch (dark red). Pathways are ordered by p-value. (B) KEGG enriched common pathways as A from model genes. Pathways are colored from deep to light based on p-value. All pathways in bold are also components of the signaling network model.)

While the response to transverse stretch was predominantly a subset of the longitudinal stretch response based on the statistical analysis, we observed that the numerical difference of gene expressions was mainly due to the larger response induced by longitudinal stretch. To illustrate the numerical relationship of the gene expression induced by transverse and longitudinal stretch, a linear regression was performed on the gene expression ($\log_2$FC) of genes (FDR$\leq$0.05) at both 30 min and 4 hr. This analysis showed significant correlation of gene expression between transverse stretch and longitudinal stretch displayed in Fig. 3.5. At 30 min, gene responses were significantly larger under longitudinal stretch than transverse stretch with the coefficient as 1.17 ($p<=0.05$, $R^2=0.98$). At 4 hr, we observed even greater difference of gene responses between transverse stretch and longitudinal stretch with the coefficient as 1.71 ($p<=0.05$, $R^2=0.90$). To further examine the difference of gene responses between transverse and longitudinal stretch at 30 min and 4 hr, we examined the two sets of DE genes and found that DE genes at 30 min were IEGs. As we showed in the clustering analysis, these genes were quickly stimulated at 30 min but returned to control at 4 hr. Other studies show that 2.5% cyclic stretch can trigger the transient response of the IEGs [303]. These results suggest that the difference between transverse and longitudinal stretch induced gene expression may be due to the effects of the magnitude of mechanical stretch applied on cardiomyocytes.

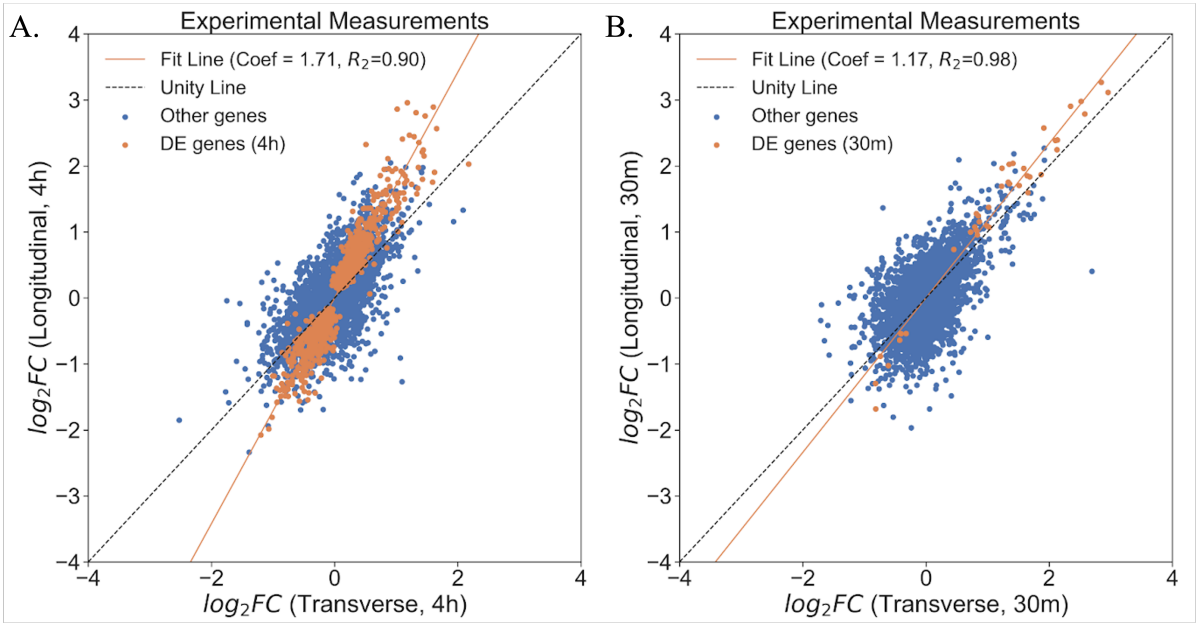

Figure 3.5| Comparison of gene expression induced between longitudinal stretch and transverse stretch. A regression was performed on the gene expression (log_2FC) between longitudinal stretch and transverse stretch at 4 hr (A, left) and 30 min (B, right) for DE genes ($p<0.05$).

3.3.2. Dynamics of the Mechanosignaling Network

To allow for the comparison between measured and model-predicted gene expression, we determined the baseline constitutive activation of the network model, as well as the threshold for a significant change in gene expression. The baseline activation of the network was varied by changing the initial weight of the stretch stimulus variable until the dynamics of the system corresponded to unstretched control conditions. Higher values of this initial constitutive stimulus resulted in higher steady-state baseline activation of the transcription factor variables, therefore requiring lower mRNA synthesis rates to match measured control mRNA levels. An initial value of 0.315 was used to simulate the (quasi-) steady state for the unstretched condition. An average gain for all genes in the network was found to be 0.32 (-1.91~5.07 on a log_2 scale) after 4 hr of stimulation compared with the measured mean for 4 hr longitudinal stretch of 0.11 (-1.98~2.76 on

a $\log_2$ scale) when the network was activated with a stretch stimulus of 0.7. Similarly for transverse stretch, the average gain was 0.18 (-0.83~2.95 on a $\log_2$ scale) after 4 hr of stimulation compared with the mean for 4 hr transverse stretch of 0.04 (-2.52~1.47 on a $\log_2$ scale). The threshold for considering a gene in the model to be differentially expressed was chosen to be ±0.5 ($\log_2$ scale) based on the threshold chosen in the measured transcriptome for significantly up- and down-regulated genes and FDR<0.05.

Fig. 3.6 shows the change in expression of all 772 target genes after 12 hr of model simulation, along with the time course of the activating stretch. Each row in Fig. 3.6 corresponds to the expression profile of a different target gene, and the rows are organized by the activity change at 12 hr. A total number of 266 target genes increase in activity with stretch, which are located at the top of Fig. 3.4A. At the bottom of Fig. 3.6, only 46 targets decrease in activity with stretch stimulus. In between these two groups of genes, a group of 460 genes changed by less than 0.5 ($\log_2$ scale). These genes were subject to both positive and negative transcription factor regulation. Among the 266 genes that were upregulated, 101 genes displayed higher-order dynamics which was activated at a short time but then dropped as time went on. Similarly, of the 46 genes that were downregulated, 28 genes were found to have higher-order dynamics. To further investigate whether the model is capable of capturing such higher-order dynamics, we found that varying feedback from protein products back to the signaling network could change the model dynamics. The model oversimplified the feedback of gene expression to the network by mapping mRNA levels directly to protein activity in the network. Varying the gain of this feedback from 0.33 to 1.3 showed the ability of the model to demonstrate more complex dynamics supplement S3.5. In this case, lowering feedback activity from a translational process is an efficient approach to mimic the sharp shift of gene activity within a short period of time. Considering that only a

small portion of DE genes appear in the MSN, there may be more regulation between mechanosignaling and gene activity that has not yet been verified (See Discussion).

3.3.3. Comparing the Mechanosignaling Network Results to Experimental Data

In order to compare model predictions with experimental gene expression changes, a

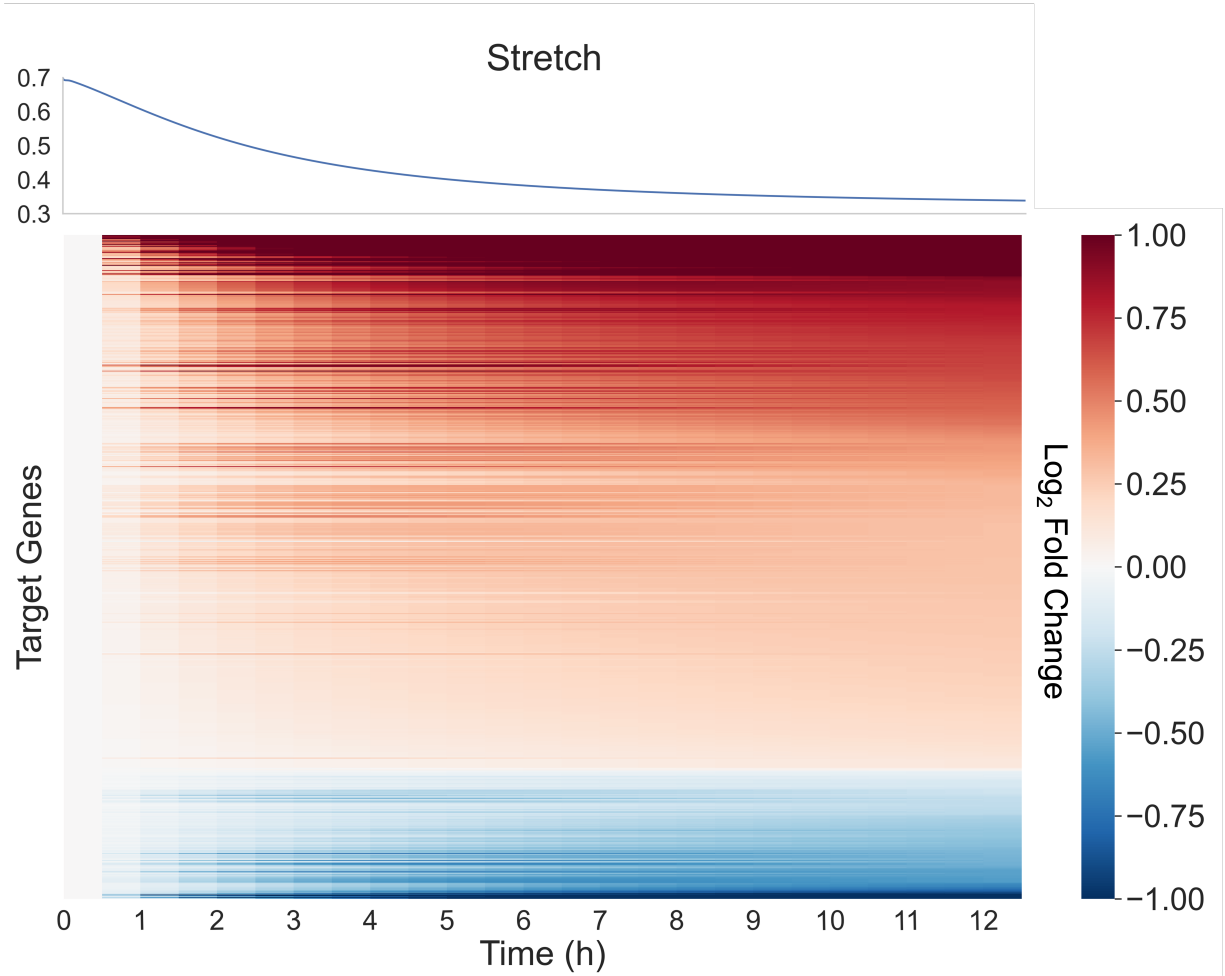

Figure 3.6| Dynamics of stretch and all 772 genes in the model of myocytes. The changes (log_2 FC) in expression of all 772 target genes in model simulation with 12-hour time course along with change in stretch. Most genes were predicted to show monotonic up- or down-regulation, but ~4% of the genes showed non-monotonic time-courses.

stretch stimulus was applied by increasing the input weight for the stretch node to 0.7 to simulate gene response induced by longitudinal stretch and 0.4 for transverse stretch as described. The overall prediction accuracy for gene expression by longitudinal stretch at 4 hr was 69% with a true

positive rate (TPR) of 29% and accurate predicted DE genes of 72%. Using the same criteria, the model predicted 63% of the genes with 54% TPR and 90% accuracy of predicted DE genes (Table 3.1). To validate the comparison, we used two extra datasets from the literature, 2-day data from the transverse aortic constriction (TAC) [304] and 1 hour data from the cyclic stretch [305]. The model predicted 91% of the genes overall with 94% accuracy of the predicted genes in the 1hr cyclic stretch dataset, and 63% of the genes overall with 90% accuracy of the predicted genes in

Table 3.1| Comparison of Model Prediction vs. Experiment Measurements

	Longitudinal Stretch, 4 hr		Cyclic Stretch, 1 hr		TAC, 2-Day		Combined
	n	accuracy	n	accuracy	n	accuracy	accuracy
All Model Genes	772	69%	697	91%	740	63%	74%
Experimentally Verified Genes	288	77%	262	87%	269	76%	80%
Predicted-DEG	22	72%	15	94%	49	90%	86%

the 2-day TAC dataset. We then used a less stringent criterial for model threshold and found more DE genes were predicted correctly, but this led to a reduction in the general accuracy.

3.3.4. Differential Responses of Transverse and Longitudinal Stretch

RNA sequencing experimental results showed that not only more genes were DE after 4 hr of longitudinal stretch compared with transverse stretch, but also that longitudinal stretch induced nearly twice as large a change in expression as transverse stretch. A linear regression was performed on model simulations between transverse stretch and longitudinal stretch at 4 hr and showed significant correlation with a coefficient of 1.93 (Fig. 3.7), which is quite close to the ratio we found in the data displayed in Fig 3.5. This result suggests that the differential response to the stretches was mainly due to the larger sensitivity of cardiomyocytes to longitudinal stretch. The

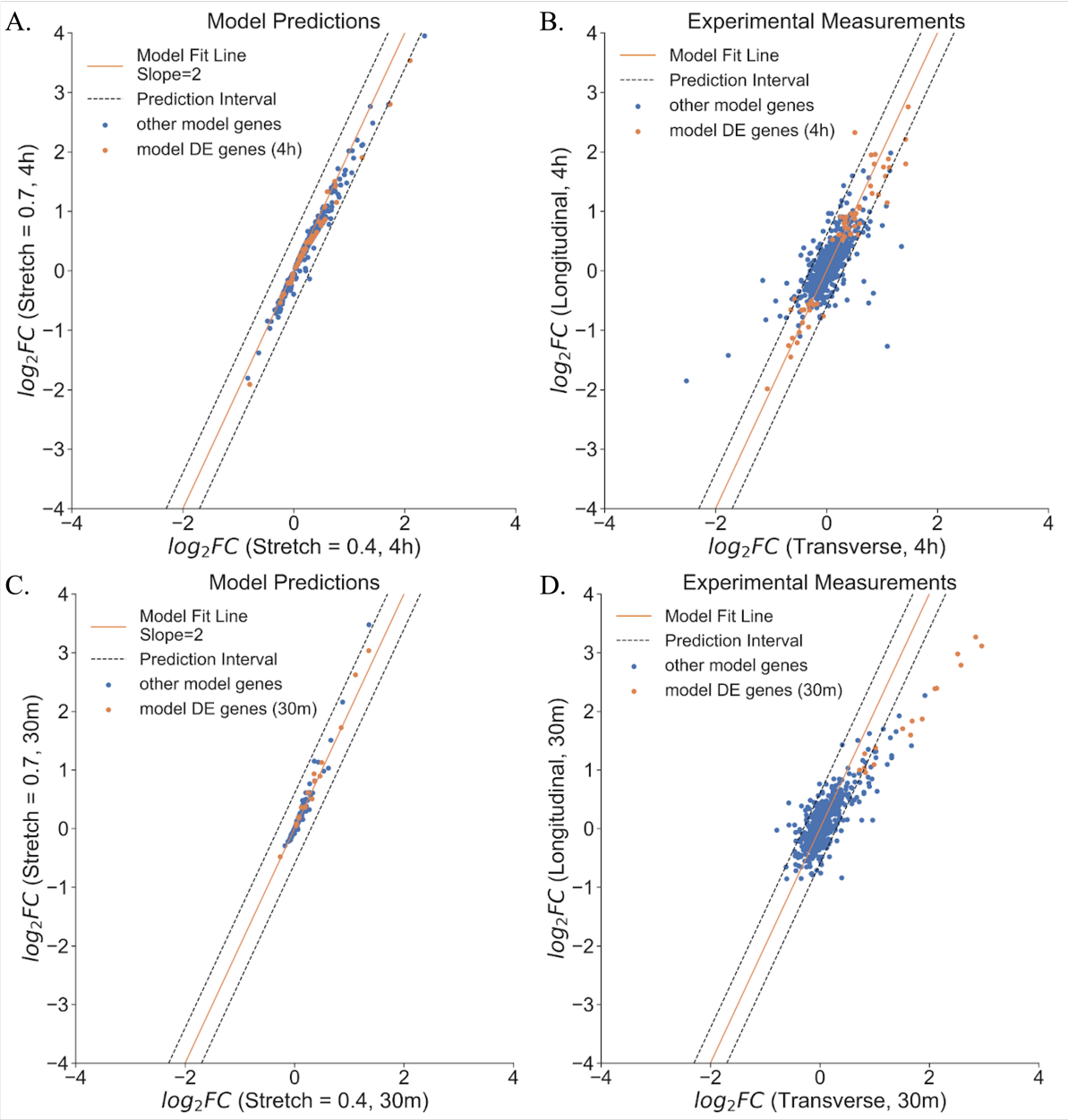

Figure 3.7| Comparison of gene expression between longitudinal stretch and transverse stretch. (A). The comparison of log_2FC of model predictions at 4 hr between transverse stretch and longitudinal stretch (top left). (B). The comparison of log_2FC of RNA-Seq measurements at 4 hr between transverse stretch and longitudinal stretch (top right). (C). The comparison of log_2FC of model predictions at 30m between transverse stretch and longitudinal stretch (bottom left). (D). The comparison of log_2FC of RNA-Seq measurements at 30m between transverse stretch and longitudinal stretch (bottom right).

linear regression of the model simulation at 30 min, however, suggested that the coefficient was 2 which is much higher than the coefficient at 30 min. This disagreement also suggests that IEGs

may follow a different expression regulation pattern from the model prediction.

3.3.5. Expression Saturation of Genes Regulated by Multiple TFs

Genes in the network are typically regulated by multiple TFs. By looking into gene expression, we found that expression of genes regulated by more than 3 and 4 TFs did not maintain the increasing trend as we observed in genes with 1 and 2 TFs (Fig 3.8).

Our model formulation assumes multiple TFs co-regulate gene expression. Literature suggests that such coregulation may exist for some TFs while others are not supplement S3.6 [306-307]. There is also evidence that the dynamics of gene expression could vary with the number of controlling TFs. Thus, by adjusting parameters such as EC_{50}, our model now is capable of predicting the dynamics of genes regulated by multiple TFs as has observed in several studies [306-307].

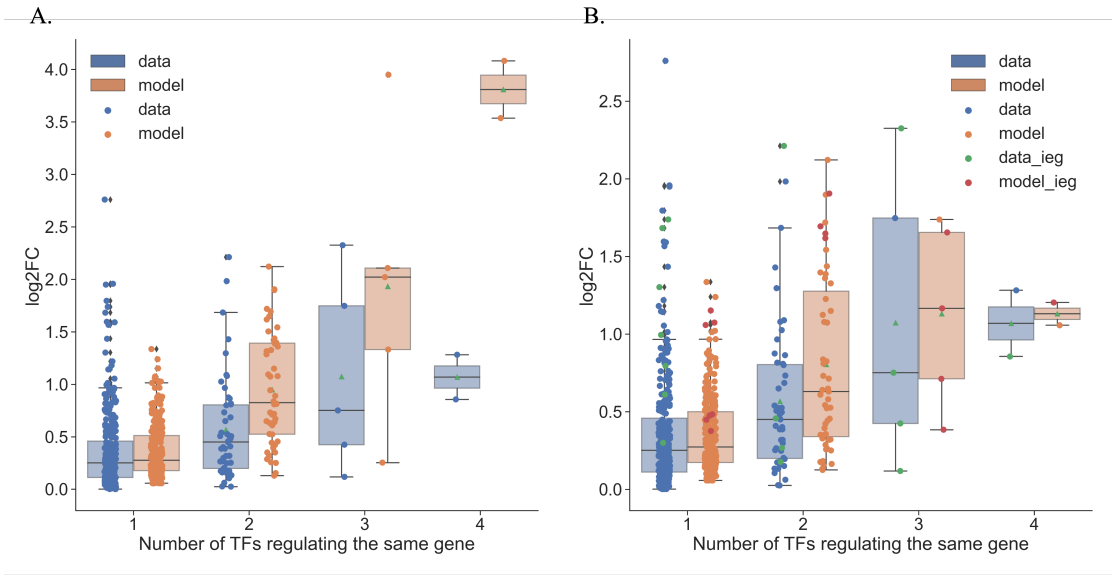

Figure 3.8| Gene Expression Dynamics with Number of Regulators. (A). Gene expression dynamics change with number of regulators with default settings. (B). Gene expression dynamics change with number of regulators after adjustment on reaction logics and parameters. (Data in blue and model simulation in orange.)

3.3.6. AT1 and ET1 Receptors are the Key Regulators in the Sensitivity of Stretch in Cardiomyocytes

To investigate if certain nodes or pathways are key components related to the differential sensitivity of stretch, a sensitivity analysis was performed, in which certain nodes were blocked in a subset of model genes which displayed at least 0.5 $\log_2$FC at either stretch conditions. As the first step to discriminate these pathways, we looked at gene activity with receptor blocking simulations. By simulating inhibition of the receptors that have been associated with mechanical signaling, the model predicted the greatest inhibition of genes when AT1 and ET1 receptors were blocked under stretch while NHE and LTCC showed the least (Fig. 3.9). We further found that AT1 and ET1 receptors, which are well studied G-protein coupled receptors, govern the regulation of the MAPK signaling pathway while NHE, LTCC and TRP, commonly known as ion channel

receptors, control the activity of the calcium signaling pathway. Then we simulated the effect of inhibition by blocking a combination of these two groups of receptors respectively. To validate the impact of AT1 and ET1 receptors, we then performed multiple receptor blockade experiments and analyzed the results with RT-PCR to test how gene activity responds to blocking AT1/ET1 receptors and LTCC/NHE/TRP receptors under transverse stretch. The experiment result confirmed our hypothesis that AT1 and ET1 receptors are key nodes in response to stretch. These predictions were confirmed by experiments that showed a significantly greater inhibition (48%) in the transverse-stretch induced expression of Ctgf, Fosl2, Mafk and Nuak1 by combined inhibition of AT1 and ET1 receptors, as opposed to combined inhibition of the LTCC, NHE and TRP channels which resulted in 18% inhibition (Fig. 3.10). Based on the model predictions and the

subsequent experiments, we hereby proposed a key subnetwork regulating gene expression in response to both stretches using network centrality analysis. This subnetwork transduces the the

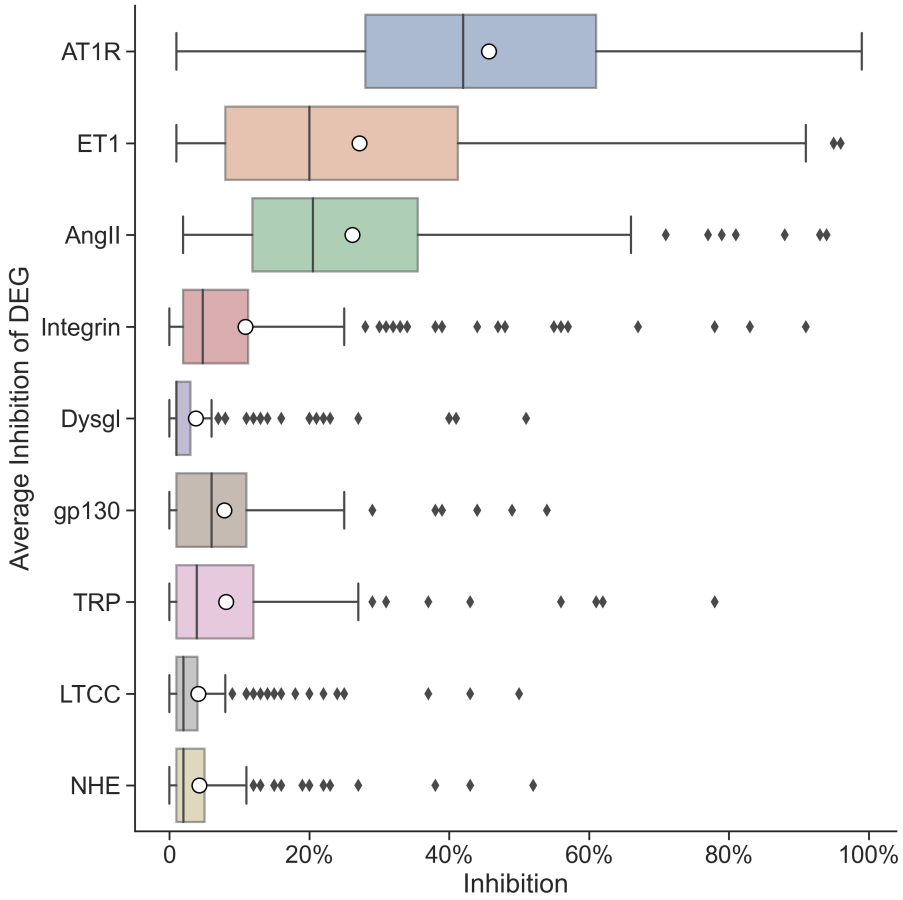

Figure 3.9| Average Inhibition of Gene Expression on Receptor Inhibition. Average inhibition of expression for genes with $|\log_2 FC| > 0.5$ when each of the receptors was inhibited. Empty circles and straight lines in the boxplot represent the mean and median of each distribution respectively.

mechanical signal via AT1 and ET1 receptors to 12 signaling molecules (including the MAPK signaling pathway) and then gene expression regulation via the stimulation of 9 TFs (Fig. 3.11).

Figure 3.10| Receptor blockade effects on stretch-induced gene responses. (A). Inhibition distribution of genes with more than 0.5 log_2FC when top 3 receptors from Table 3.2 were blocked compared with the condition when other receptors were blocked as negative control (we chose three ion-channel receptors for easier prepared experiment). (B). Gene expression changes of both experimental measurements and model predictions of the 4 genes with highest inhibition and 2 negative control genes were displayed. Ctgf, Fosl2, Mafk and Nuak1 were blocked to a greater extent near baseline level or below when AT1R/AngII/ET1 were blocked. In addition, two negative control genes namely Hbegf and Tgfb2 were also displayed.

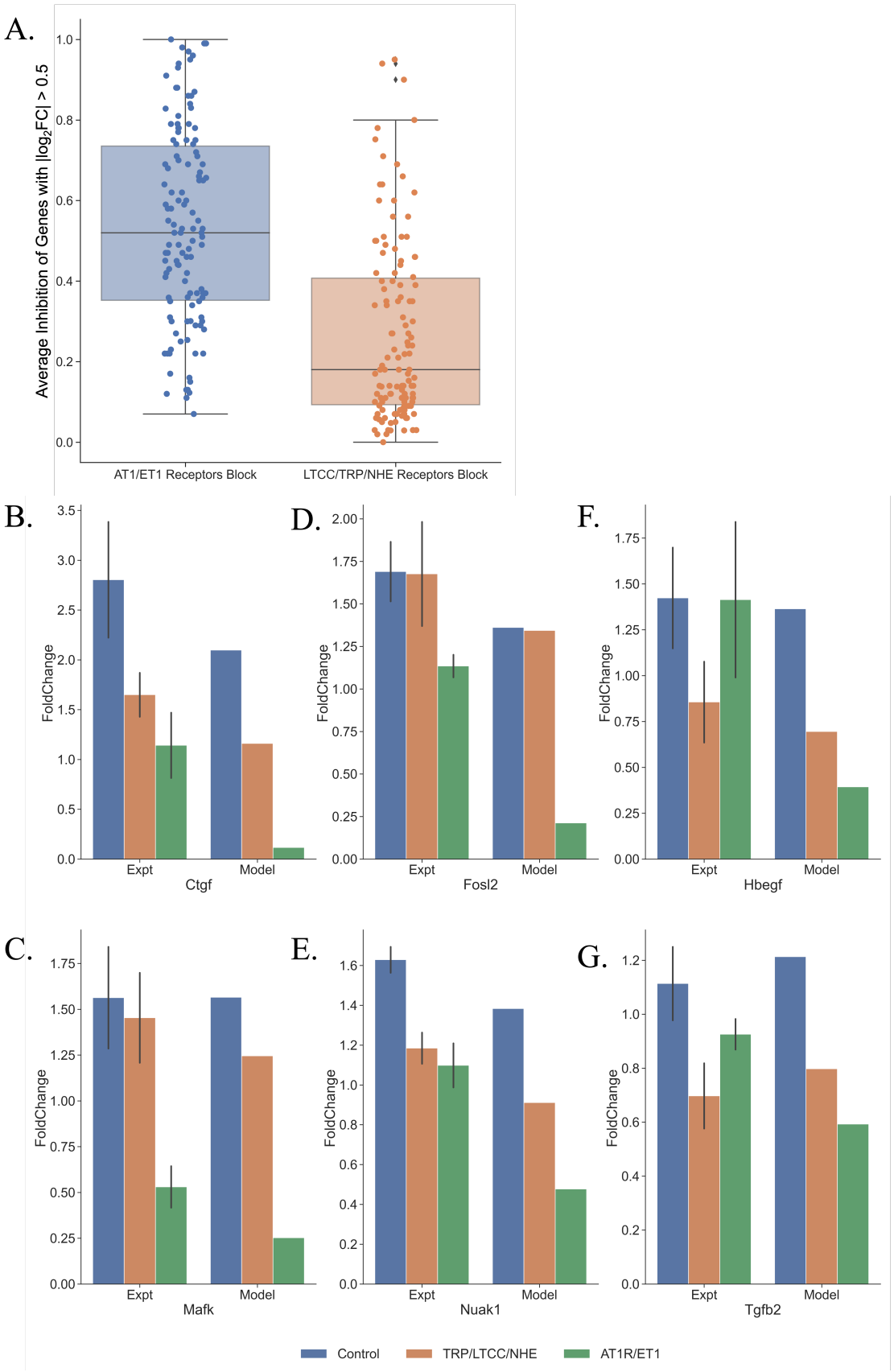
A.
Average Inhibition of Genes with |log2FC| > 0.5
1.0
0.8
0.6
0.4
0.2
0.0
AT1/ET1 Receptors Block
LTCC/TRP/NHE Receptors Block
B.
Ctgf
D.
Fosl2
F.
Hbegf
C.
Mafk
E.
Nuak1
G.
Tgfb2
FoldChange
Expt
Model
Control
TRP/LTCC/NHE
AT1R/ET1

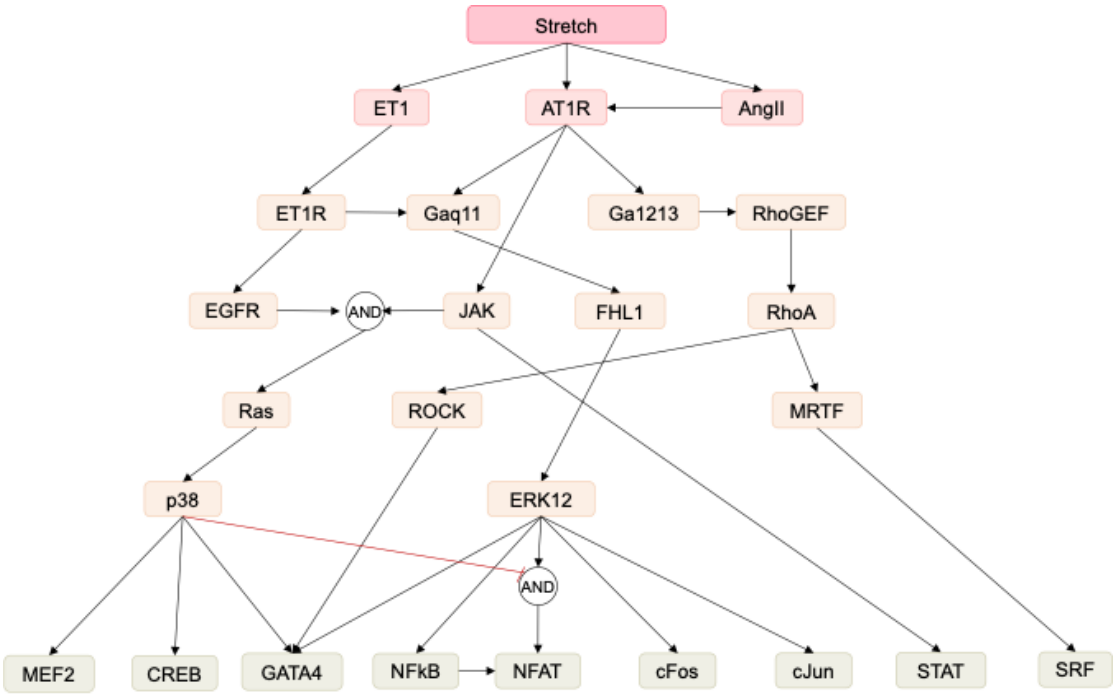

Figure 3.11| A subnetwork regulating gene expression in response to stretch. A subnetwork was extracted for regulating gene expression in response to stretch using network centrality analysis described in section 3.2.7. The subnetwork includes 16 signaling molecules and 9 transcription factors.

3.4. Discussion

3.4.1. Summary

Hypertrophic remodeling of cardiomyocytes is regulated by a variety of mechanical stimuli. We and others have shown that cardiac myocyte gene expression is regulated differently by stretch that is primarily parallel to the myofilament axis than by stretch in the transverse direction [308]. The anisotropy of myocardial strain *in vivo* varies with external hemodynamic loading and location in the ventricular wall. To identify the mechanosensitive signaling pathways and gene expression programs regulated by axis-specific cell strain, we subjected micropatterned mouse neonatal cardiomyocytes to 30 min or 4 hr of static non-equibiaxial stretch that was predominantly parallel to or transverse to the myocyte long axis. Four hours of static longitudinal

stretch *in vitro* induced differential expression of 557 genes, compared with only 30 for the same duration of transverse stretch, and only one of those was also an output of the network model. This may be a consequence of the elliptical design of our stretch apparatus that actually applies stretch in two directions at once, in a ~4:1 ratio. The numerical differences between gene expression profiles in response to transverse and longitudinal stretch suggest that longitudinal stretch-induced responses are nearly twice as large as those from transverse stretch. To help interpret these measured transcriptional responses to stretch, we extended our earlier logic-based computational model of the cardiac myocyte mechanosignaling network to incorporate transcriptional control of 772 genes shown to be regulated by 11 transcriptional factors in the signaling model [172]. This novel analysis predicted observed changes in expression of these 772 genes after 4 hr of longitudinal stretch with an accuracy of 69% and 72% for DE genes. By setting a lower weight for transverse stretch, we further found model consistency with numerical data from transverse stretch. More importantly, the comparison of model predictions between transverse and longitudinal stretch also showed a similar trend to what we observed in the experimental data. To help define the key nodes that determines this different sensitivity, we simulated inhibition of all the mechano-sensitive receptors in the model and predicted that gene responses induced by either transverse or longitudinal stretch were inhibited most when the AT1 and ET1 receptors were blocked. These predictions were confirmed by experiments, which showed a 48% inhibition of the transverse-stretch induced expression of Ctgf, Fosl2, Mafk and Nuak1 by combined inhibition of AT1 and ET1 receptors, compared with 18% by combination pharmacological blockade of the ion channel receptors including LTCC, NHE and TRP. Thus, we propose that a subnetwork of gene expression by stretch could be transduced by 16 signaling molecules, which includes AT1 and ET1 receptors and the MAPK signaling pathway.

To our knowledge, this is the first model analysis of its kind to predict genome-scale transcriptional responses to mechanical stimulation in any cell type. While the immediate early transcriptional response was slightly greater to longitudinal than transverse stretch, it was transient, and it was surprising that by four hours, an order of magnitude more genes were differentially expressed in the longitudinally stretched cultures. Several previous studies in cultured rat neonatal ventricular myocytes have reported a more robust response to transverse than longitudinal stretch, typically after 24 hr [262]. Gopalan *et al.* observed that 24 hr of static longitudinal strain in rat neonatal ventricular myocytes did not significantly alter myofibril accumulation or protein expression of hypertrophic markers, but transverse principal strain significantly increased myocyte staining of actin filaments, atrial natriuretic peptide, connexin-43 and N-cadherin [262]. The duration of stretch is likely to be important in these experiments. We limited our stretch duration to 4 hr based on the observation that cultured micropatterned rodent neonatal ventricular myocytes hypertrophied longitudinally in response to 10% static longitudinal strain fast enough that unstretched sarcomere length was fully restored in 4 hr [264]. This suggests that after 4 hr, myocytes would no longer "feel" a static longitudinal stretch of 10%. This assembly of new sarcomeres in series was inhibited by blocking PKC and FAK signaling [264]. To account for this observation, our analysis used the "cell area" phenotype output of the model as a feedback variable that reduced the effective applied stretch proportionately over the 4-hour duration of mechanical stimulation. The robust 4 hr transcriptional response to longitudinal stretch that we observed may reflect the possibility that ventricular myocytes are primed to respond to increased load and grow longitudinally after birth. The principal mode of neonatal ventricular growth is an increase in chamber diameter due to faster postnatal myocyte lengthening than thickening [264].

3.4.2. Biological Significance of the Transcriptional Responses to Anisotropic Stretch in Cardiomyocytes

The alignment of cardiac myocytes and extracellular matrix in myocardium, and the highly organized cytoskeleton of cardiac myocytes, make their biophysics, mechanotransmission and mechanosensing dependent on the localization and axes of physical interactions. The z-disc and costamere, both are aligned transverse to the myofilament axis, and are both signaling centers for mechano-transduction [309], though it is by no means clear which specific physical stimuli these structures are more sensitive to. By far, most genes in this study were induced by 4 hr of longitudinal strain, though after 30 min, transverse and longitudinal stretch both induced a significant number of immediate early genes, such as Fos and Jun, as well as regulators of cell growth, cell cycle and cell death [31, 306-307, 310-311]. The few genes in our measurements that were activated by transverse stretch but not longitudinal stretch was too small to identify any significantly enriched pathways. In contrast, the great majority of stretch-induced genes were regulated by longitudinal but not transverse strain. Genes significantly upregulated by longitudinal stretch were strongly associated with sarcomeric, adherans junction and focal adhesion compartments, cytoskeletal protein binding and organization, and MAP kinase signaling. Notably, the 772 gene outputs of the model were also enriched for the same KEGG pathways as the transcripts found to be induced by RNA-seq, suggesting that the measurements were consistent with the published literature used to create the model. In contrast, many genes that were significantly induced by longitudinal stretch were not represented in the model and included significant clusters associated with sarcomeric ion channels and electrical activity. This suggests that more studies are needed to identify the regulators of this previously unreported cardiomyocyte stretch response.

Longitudinal stretch induced a much broader transcriptional program compared to transverse stretch after 4 hr. While the expression of very few genes was changed by transverse and not longitudinal stretch (including on one in our model), the majority of differentially regulated transcripts were induced by longitudinal but not transverse strain. Comparing model predictions with experimental results suggests that calcium influx and gene regulation by SRF may be specifically activated by longitudinal stretch. Longitudinal stretch has previously been shown to increase in intracellular calcium in cardiac myocytes, and inhibition of the transient receptor potential cation channel, subfamily V, member 4 (TRPV4) prevented this increase [91]. TRP channels are calcium-permeable cation non-selective channels that are physically linked to the costamere via Homer proteins [312] and mechanosensitive.

To examine the key nodes regulating the major transcriptional responses that were activated by either transverse or longitudinal stretch in more detail, we inhibited each receptor in the model and compared the effects to the list of genes that were induced by both transverse and longitudinal stretch. This analysis predicted that blocking AT1 and ET1 receptors would have a significantly greater effect on transverse-stretch induced gene expression than combination blockade of the three ion channels and transporters in the model, and this prediction was confirmed experimentally. We further found that by AT1/ET1 receptors are the main regulators of most genes in the network by blocking a combination of multiple receptors (AT1/ET1 receptors vs. ion channel receptors).

Several pathways that were not included in the model were specifically enriched for DE genes that were induced only by longitudinal stretch, including the KEGG annotations for Hippo and Rap1 signaling pathways. The Hippo signaling pathway co-regulates cardiac myocyte hypertrophy and proliferation with several micro-RNAs by regulating downstream gene

expression [313-314]. The activation of Rap1 can also regulate cell-cell interactions, adhesion and migration by stimulating ERK1/2 and Rho-ROCK pathways which are both in our model [315]. Several genes encoding for potassium channels were significantly downregulated with longitudinal stretch but not included in the model. Down-regulation of repolarizing potassium currents is a characteristic of the pro-arrhythmic "electrical remodeling" associated with structural heart diseases in which myocardial mechanical loading is increased such as ventricular hypertrophy and heart failure [316]. While studies have investigated mechanoregulation of the expression of junctional proteins involved in electrical conduction such as connexin-43 [317], mechanoregulated pathways controlling potassium channel remodeling have not been elucidated.

3.4.3. Systems Modeling Approaches

Two main classes of mathematical model have been used to model gene expression at the system scale as we discussed in section 1.2 and 1.3: Boolean, and ODE models. These modeling approaches have been used to help interpret experimental data, to infer new relations from experimental data, and to define new testable hypotheses. Our new network model was based on a logic-based ODE system that combined Hill-type modeling with mass action kinetics. By using mass action to model mRNA synthesis and degradation, we were able to make use of mRNA half-life measurements to initialize the transcriptional activity to the measured control state by assuming steady state at baseline. This overcame the disadvantage of the normalized logic-based approach that by default, the initial steady-state of each gene in the model would be zero (or occasionally maximal), making quantitative comparison with experimentally measured mRNA fold changes impractical. In the cases when the model output gene encoded a node in the model, we used a simple translation reaction to update the normalized activity of the node. We assumed a linear relationship between gene activation rates and normalized transcription factor activity. while

this approach allowed us to account for baseline gene expression in the control state, it also required us to specify an initial residual level of network activation that was arbitrary. More biochemically realistic models of transcriptional regulation have been developed that could overcome some of the limitations of our current implementation [166].

3.4.4. Limitations and Future Studies

Our experimental apparatus applies static non-equibiaxial stretch [291]. While many investigators have used pulsatile stretch to better approximate dynamic myocyte loading *in vivo*, for oscillatory stretch to replicate physiological mechanical conditions, myocytes would need to be synchronously paced in phase with the stretch, and this becomes a difficult setup. We consider the static stretch stimulus to be more representative of a sustained alteration in hemodynamic load and a proven stimulus to myocyte hypertrophy. While the non-equibiaxial cell stretcher we used does apply physiologically representative anisotropic strains, because it was not purely uniaxial, some stretch was simultaneously applied in both directions. The 3.5% longitudinal strain when the major stretch axis was transverse, may have been sufficient to elicit a response and explain why we could not identify a significant number of genes that were exclusively activated by transverse stretch alone. Another potential limitation is the likely inclusion of non-myocytes in the cultures (fibroblasts, endothelial cells, etc.). Myocytes were purified prior to culture via pre-plating as described previously [291]. However, the procedure does not completely remove all non-myocytes, and therefore, some of the measured gene expression could be from non-myocytes or a result of paracrine signaling. Experimental limitations of RNA-seq may also contribute to differences between model and experiment. The analysis of the current study shows that RNA-seq data analysis has a power of 0.8. As with many RNA-seq study designs, the current study has a small number (4~5) of biological replicates. Therefore, while the false discovery rate criterion for

significantly changed gene expression was stringent, the probability of a type II error was consequently higher. Genes predicted by the model to be stretch-regulated whose observed changes did not reach statistical significance, would be good candidates for more detailed experimental investigation with more replicates.

A limitation of our network modeling approach is that many differentially expressed genes were not included the model and a significant number of target genes in the model were not found to change experimentally. Some of the literature sources used to construct the transcriptional regulatory network were based on experiments that were not specific to cardiac myocytes, and none of these interactions were specific to stretch. Signaling parameters of the model were mainly derived from our previously published and validated network model without any parameter optimization [172]. In a recent uncertainty quantification study of that network model [318], we found that the model accuracy was robust to parameter changes over a wide range. In the present extension to the model, we were able to predict mRNA fold changes over time, enabling more quantitative comparison with experiments. This, coupled with the larger number of model outputs, should make the new model more amendable to numerical parameter optimization. The model also only uses canonical mechanisms of transcriptional regulation. Published studies indicate that other regulatory mechanisms such as microRNAs are also important in myocyte hypertrophy responses to mechanical loading [319-320].

3.5. Conclusions

In this study, we developed a novel extension of our previous myocyte mechanosignaling model that added the transcriptional regulation of 772 target genes and validated the model with RNA-seq measurements of transcriptomic-wide gene expression levels using primary neonatal micropatterned mouse ventricular myocytes cultures exposed to up to four hours of anisotropic

stretch. This new approach, with introducing the mass-action method, displayed high performance that 69% of the model predictions and 72% of predicted DEG were confirmed by the experimental measurements. Our analysis suggests that the difference between transverse and longitudinal stretch responses in cardiomyocytes may be related to the sensitivity of directional mechanotransduction, with the sensitivity to longitudinal stretch being greater than transverse. In addition, we found that gene expression did not monotonically change with the number of TFs but showed a saturated expression dynamic. This finding along with model simulations indicate that TFs may alter dynamics by reaching maximal activity earlier when multiple TFs co-regulate the gene. Moreover, through the inhibition simulation and the subsequent experiments, we identified that the stretch induced gene responses were mainly regulated by the specifical interaction with AT1 and ET1 receptor pathways rather than other receptors such as LTCC, TRP and NHE, which may be redundant in stretch sensing. Finally, our study showed the importance of a hypertrophy pathway that regulates target genes via the activation of AT1/ET1 receptors through the MAPK signaling pathway.

3.6. Acknowledgements

Chapter 3, in part, is currently being prepared for submission for publication of the material. Cao, Shulin; Buchholz, Kyle S.; Tan, Philip; Stowe, Jennifer C.; Aboelkassam, Yasser; Wang, Ariel; Zambon, Alexander C.; Saucerman Jeffery J.; Omens, Jeffery H.; McCulloch, Andrew D. Reprinted with permission from all co-authors. The dissertation author was a primary investigator and author of this material.

Chapter 4: Uncertainty Quantification and Regulation Analysis of Profibrotic Mechanosignaling in Pulmonary Arterial Adventitial Fibroblasts

4.1. Introduction

Cell signaling networks are cascades of biochemical reactions that regulate cellular responses to external cues, and their dysregulation is important in the progression of disease. Pulmonary arterial hypertension (PAH) is a vasculopathy manifested by sustained elevation of pulmonary arterial pressures, vascular constriction, and irreversible vascular remodeling [106], which is mediated in part by pulmonary arterial adventitial fibroblasts (PAAFs) in response to pathological strain and stresses such as mechanical overload and hypoxia. Studying the interplay between the effects of signaling cytokines, hypoxia, and the mechanical stimuli that are activated in PAH will help to elucidate signaling pathway interactions and may aid in developing novel therapies to reverse vascular fibrosis and disease progression.

PAAFs residing in the adventitial layer of the arterial wall are responsive to altered mechanical conditions and function to remodel the extracellular matrix (ECM) thereby modulating its mechanical properties [106], and there is evidence that PAAFs are regulated by matrix stiffness [374-376], stretch [121, 377], or overstretch injury [361, 378] and hypoxia [106]. During injury, PAAFs are activated and differentiate into myofibroblast subtypes that remodel vascular wall properties by directly altering the expression, degradation or cross-linking of ECM proteins including collagen, fibronectin, and elastin. Given that the ECM also serves as a substrate for cell adhesion and sends physical and chemical cues that determine cell phenotype [321], it has been

suggested that matrix stiffening may signal tissue remodeling and be causative drivers of pulmonary hypertension [351]. While fibroblast activation induces changes in the composition and structure of the vascular collagen matrix, it is unclear how PAAFs are regulated by matrix composition and stiffness, how PAAFs are affected by altered vessel stretch due to increased loading during PAH, what signaling pathways regulate these phenotypic responses to physical stimuli, and the extent to which these mechanically stimulated pathways overlap and interact.

Mathematical modeling of cell signaling networks is a useful tool for synthesizing available experimental data and investigating interactions between pathways that are difficult to study experimentally. To better identify the receptors and pathways involved in regulating PAAF responses during PAH, we introduced a new logic-based ordinary differential equation model [173] of the major biochemical networks known to regulate pro-fibrotic cell responses such as ECM expression, proliferation, and myofibroblast transformation in PAAFs [321]. The network model was derived from published cell biological experiments and transcriptional measurements in primary PAAFs supplemented, where necessary, with information on canonical pathway structure from better studied fibroblast types, mainly cardiac fibroblasts. Inputs to the PAAF signaling network model were based on reported stimuli upregulated in PAH [106]. While the signaling pathways included in this model have been identified in PAAFs, their interplay is not well understood, and there is a paucity of experimental data in the literature specific to these fibroblast cells. Therefore, after constructing a PAAF signaling network model, we carried out a sensitivity analysis to identify the important nodes in the network.

Creating a cell signaling model inherently introduces parameter uncertainty, since experimental studies rarely report quantitative biochemical reaction properties. There are also epistemic uncertainties in the structure and logic of the network, which depend on published

experiments from a variety of cell types and conditions that are occasionally inconsistent or ambiguous [322]. Therefore, to analyze the robustness of the developed model and identify how small perturbations in the parameters leads to changes in model predictions, we have carried out uncertainty quantification (UQ) analysis of the model parameters. Using a separate set of data not used in the model formulation, we determined the prediction capabilities of the model and its qualitative accuracy. We also used this method to determine if adding pathways from other fibroblast cell types impacts model accuracy.

Here, we have not attempted to optimize model parameters, so we cannot expect close quantitative agreement between model predictions and experimental data. Rather, objective qualitative comparison criteria were used, and we used UQ to assess the robustness of model prediction accuracy and to identify the modules and parameters that are most affected by incomplete or noisy data [268]. Analysis of parameter and structural uncertainty showed that the PAAF model is robust to most parameter uncertainty and identified the new experiments that are needed the most to improve model confidence and accuracy. Also, we used an elaboration of this model together with *in-vitro* experiments on PAAFs cultured in different stiffness gels and under different stretch conditions to determine how six profibrotic genes may respond to stretch and stiffness changes mimicking mild and severe stages of PAH. The analysis suggests pathways that are differentially activated by changes in cell stretch and ECM stiffness that may help elucidate the sequence of tissue remodeling in PAAFs.

4.2. Materials and Methods

4.2.1. Computational Model of Pro-Fibrotic PAAF Cell Signaling

The PAAF signaling model was manually constructed with the same default parameters and model file structures as the one developed by Zeigler *et al.* for cardiac fibroblasts [131]. Out of the 92 reactions in our model, 52 reactions are unique to PAAFs. The model construction was based on results reported in 52 published papers describing experimental studies in PAAFs or other fibroblast types [25, 108, 111, 113, 115-120, 122, 124, 130, 135-138, 143-144, 147, 149, 152-154, 158, 323-349] when necessary to complete 18 intermediate reactions not described in the comparatively sparse literature on PAAF signaling. In addition, 20 independent papers documenting *in-vitro* or *in-vivo* experiments in rat or human PAAFs and not used in the original model formulation were set aside to measure the predictive capability of the model.

The resulting PAAF signaling network (Fig. 4.1) integrates seven input stimuli that are implicated in PAH pathogenesis: mechanical loading, transforming growth factor-β (TGF β), tumor necrosis factor- α (TNF α), platelet-derived growth factor (PDGF), angiotensin II (f), fibroblast growth factor (FGF), and hypoxia. These activate seven receptors and signaling modules, namely the phosphoinositide 3-kinase (PI3K), TGF β, Notch, reactive oxygen species (ROS), mitogen-activated protein kinase (MAPK), calcineurin and Hippo pathways. Downstream

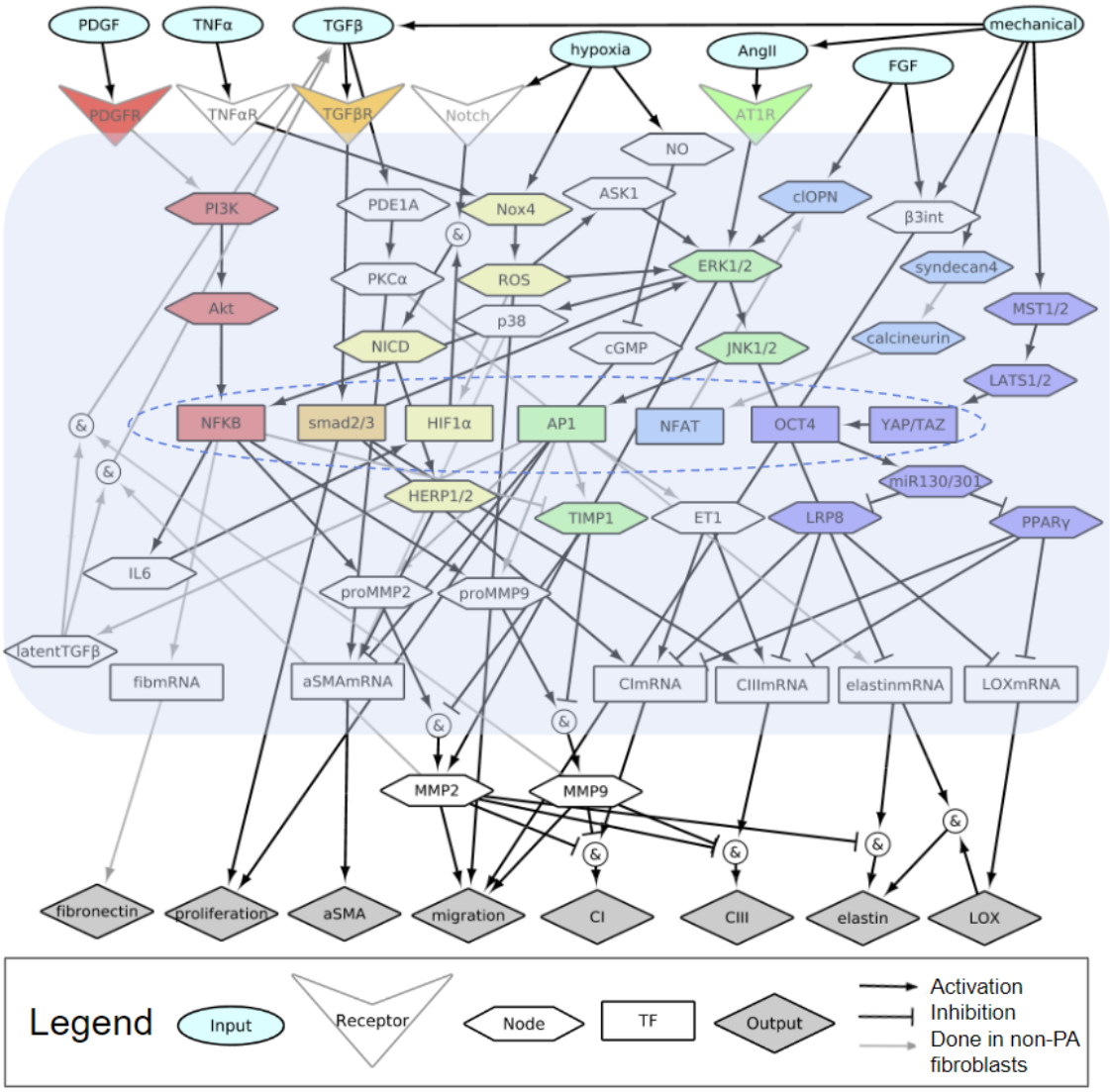

Figure 4.1| A schematic of pro-fibrotic PAAF cell signaling network comprised of 64 nodes. This network is comprised of 64 nodes with input stimuli (blue ovals), receptors (triangles), signaling molecules (hexagons), transcription factors (colored rectangles), messenger RNA (rectangles) and phenotypic outputs (grey diamonds). The colors represent the recognized signaling modules including phosphoinositide 3-kinase (PI3K) (red), TGFβ (orange), Notch, reactive oxygen species (ROS, yellow), mitogen-activated protein kinase (MAPK, green), calcineurin (blue) and Hippo (purple). The arrows indicate the 92 activation or inhibition reactions, with the grey arrows denoting reactions based only on experiments in non-PA fibroblasts. Converging reactions denoted by & indicate 'AND' gate logic, while other combinations imply 'OR' gate logic. (Online version in color.)

transcription factors regulate the expression of eight outputs important in the pro-fibrotic cell

phenotype and ECM remodeling [149]. Overall, there are 64 nodes that represent physical stimuli, ligands, receptors, signaling molecules, transcription factors, messenger RNA (mRNA), proteins, and cell phenotypes interconnected via 92 reactions. The publications used to justify each individual reaction and interaction are cited in electronic supplementary material, S4.1.

Using previously described methods in Section 1.2, the PAAF signaling network model was implemented as a system of logic-based ordinary differential equations that were integrated numerically using the explicit second and third order Runge-Kutta method as described previously in Chapter 1 [131, 172]. The baseline model solution was obtained using a default Hill coefficient of n=1.4 and EC_{50} of 0.6 for every node. The time constants τ for each different reaction type in the network followed those used previously [131]: 0.1 hour for signaling reactions; 1 hour for transcription; and 10 hr for translation. Timepoints chosen were run at steady state. Input weights (ω) were initialized to 0.25 to represent baseline activity. Reaction weights for the rest of the system (ω) were set to a default value of 1.

In the revised network analysis where we wish to distinguish the effect of substrate stiffness and stretch, the input weights of stretch and stiffness were both set to 0.25 to represent the softest matrix, 0.5-kPa, and no applied stretch. We increased the stiffness input weight to 0.7 and 0.9 to represent the effects of 3-kPa and 10-kPa substrates, respectively, and evaluated the model at t=72 hr to mimic the *in-vitro* experimental time course.

To numerically simulate the effects of stretch on PAAFs after 24 hr and the changes in substrate stiffness for 72 hr when inhibiting nodes, the model was evaluated at those time points (i.e., $y_i(t=24)$ and $y_i(t=72)$) after the corresponding input weights of stiffness and stretch were increased from 0.25 to 0.7. To simulate the effects of inhibition, $y_{i,max}$ corresponding to blocked

nodes were set to 0, while the other parameters remained the same. The change for each gene was calculated with respect to each condition's control group.

To simulate the different conditions under which losartan inhibited AT1R, we conducted eight sets of simulations. Four sets of these simulations were evaluated on 0.5-kPa substrate stiffness for 72 hr with parameters at baseline, and input weights stiffness and stretch set to 0.25. For simulations involving stretch but no inhibition, the input weight of stretch was increased from 0.25 to 0.7 and the model was evaluated at t=24 hr. For the unstretched and stretched inhibited conditions, $y_{i,max}$ corresponding to the AT1R node was set to 0 before applying changes to the stretch input weight and evaluated at t =24 hr. The same combinations were used for the other four set of simulations on 3-kPa substrate conditions, but with a stiffness input weight of 0.9.

4.2.2. Model Validation

To validate the model, 39 input-output experiments in rat or human PAAF cells (reported in 20 papers [351-370]) were classified as observing a significant increase or decrease, or no significant change in activity of an output quantity that is a node in the model in response to a stimulus, that was also an input to the model. The threshold for considering a response in the model to represent a significant change in output activity was chosen to be 0.05. *In-vivo* data were used when there were no *in-vitro* data reported in the literature on PAAFs. The time-course of the model for each comparison was matched to that of the corresponding experimental measurement. Citations to the publications used for each model comparison experiment are given in electronic supplementary material, S4.2.

4.2.3. Sensitivity Analysis

A model baseline was calculated by setting all input weights to 0.25 and the initial values of all state variables to 0. They were then integrated until a steady state was achieved for all nodes at 200 minutes. 100% knockdown of each node was simulated by reducing y_{max} from 1 to 0, and the subsequent effect at every node was calculated as knockdown activity minus baseline activity. Sensitivity analysis was performed under baseline conditions and under conditions of high mechanical stretch (mechanical input weight set to 0.9) to represent the effects of mechanical overload and matrix stiffening associated with PAH.

4.2.4. Uncertainty Quantification

To propagate parameter uncertainties in the network, we followed the approach described by Marino *et al.* [370], in which each parameter in θ is assumed to be a uniform random variable from the uniform distribution ~ U(min, max). Herein, we propagate three uncertain independent parameters. These parameters were sampled randomly from uniform distributions. The ranges chosen for the model parameters vary roughly 30% around their mean when carrying out UQ analysis. For example, n was chosen to be a uniform random variable such that n ~ U(1.36, 2.36). It should be noted that the range of n was set from 1.36 to 2.36 as guided by the equation in section 2.2.3.1 [173], since a default value of EC_{50} = 0.6 gives a minimum of n to be 1.36 or else B would be negative and thus K would not produce a viable value. When n is set to 1.4, the EC_{50} can only vary slightly around the default value of 0.6, so the UQ analysis was run with n set to 2, in order to perturb a wider range of EC_{50} from 0.4 to 0.7, EC_{50} ~ U(0.4,0.7). Similarly, the input weight ω was also run with n set to 2 to keep the results consistent, and was set to vary from 0.1 to 0.4, around the default value (0.25), ω ~ U(0.1,0.4).

The uncertainty quantification simulations were performed using the package Uncertainpy 1.2.1 in Python [275]. The package was run in order to quantify the change in model accuracy when varying the aforementioned three parameters: n, EC_{50}, and ω. Since there are only 7 locations in the network that depend on the input weight ω, we used the polynomial chaos expansion approach with order-4 approximation to non-intrusively propagate uncertainty. This is generally less computationally expensive than Monte Carlo simulations, however for systems with over 20 uncertain parameters, the required number of model evaluations scales worse than the Monte Carlo method [275]. Because of this, the (quasi-) MC method was used with 5,000 model evaluations for UQ analysis of n and EC_{50} due to there being 99 reactions each with individual n and EC_{50} values being perturbed in the network. The ranges of parameter values that are noted in the UQ results are identified by examining the output file and sorting by accuracy, then analyzing the combinations of parameters that led to notable changes in accuracy. The code used for uncertainty analysis is available on Github.

Moreover, to compare the baseline model results with a model derived only from experiments in PAAFs or cardiac fibroblasts, we ran UQ analysis using the (quasi-)Monte Carlo approach varying all 3 parameters where $n \sim U(2, 2.4)$, $EC_{50} \sim U(0.4, 0.6)$, and $\omega \sim U(0.1, 0.4)$, and with 10,000 model evaluations. The effects on model accuracy of changing parameters and the network structure were evaluated by classifying input-output model results as increased, decreased, or unchanged using a threshold change of 0.05 and determining the percentage of model results in agreement with the published experimental findings.

4.2.5. Cell Isolation

Pulmonary arteries (PAs) were harvested and isolated from six to eight weeks old normotensive male Sprague-Dawley rats (Charles River Laboratories, Wilmington, MA, USA) under advisement of the Animal Care and Use Committee at the University of California San Diego (Protocol #S17237). The adventitial layer was stripped off and segments were cut into pieces, enzymatically digested with 1 mg/mL Type 2 collagenase (#LS004176, Worthington, Lakewood, NJ, USA) in Dulbecco's Modified Eagle Media (DMEM, D5030, Gibco Thermo Fisher Scientific, Waltham, MA, USA) and agitated for 1.5 hr at 37 ℃, following the protocol by Liu *et al.* [118]. Fibroblast media was prepared by combining DMEM and 10% by volume fetal bovine serum (FBS) (#16140, Sigma Aldrich, St. Louis, Missouri, USA) and 1% antibiotic-antimycotic solution (#15240062, Gibco Thermo Fisher Scientific, Waltham, MA, USA). Isolated PAAFs were expanded on T75 tissue culture plastic (#25-209, Genesee Scientific, El Cajon, CA, USA) in the incubator at 5% CO_2 and 37 ℃, 100 % humidity. To characterize PAAF cultures and compare their phenotypes to PAAFs *in-vivo*, 10-mm segments of fixed, intact normotensive pulmonary artery were cryosections and immunolabeled with antibodies against von Willebrand Factor (vWF) (#SC-365712, 1:50, Santa Cruz Biotechnology, Santa Cruz, CA, USA) as a marker for pulmonary arterial endothelial cells, myosin-11 (MYH11) (#SC-6956, 1:50, Santa Cruz Biotechnology, Santa Cruz, CA, USA) as a marker of pulmonary arterial smooth muscle cells and vimentin (#AB-92547, 1:250, AbCam, Cambridge, UK) as a marker in all pulmonary artery cells that is also highly expressed in pulmonary arterial myofibroblasts, with appropriately matched secondary antibodies (Life Technologies, Carlsbad, CA, USA) (1:500) (Goat anti-Mouse Texas Red (#T862), Goat anti-Rabbit AlexaFluor700 (#A21038) and Wheat Germ Agglutinin-488 for

membrane (#W6748, 10 μg/mL) and DAPI (#P36941) using standard immunofluorescence protocols with images taken at 40x magnification. The same staining protocol and imaging settings were also used to image isolated PAAFs that were expanded on plastic to characterize the culture. Cells were freshly isolated or used at a maximum passage number of 3 for these experiments. Data on Cytosoft® 6-well plates (#5140 and #5142, Sigma Aldrich, St. Louis, Missouri, USA) were from seeding 100,000 frozen PAAFs per well, where 2 wells were pooled for RNA isolation after 3 days.

4.2.6. Stretcher Preparation

Polyacrylamide gels were prepared using stiffnesses corresponding to a normotensive pulmonary artery (0.5-kPa), mild PAH (3-kPa), and severe PAH (10-kPa), based on work by Liu *et al.* [380]. Gel stiffness was modulated by the percentage of acrylamide and bis-acrylamide (#A9099 and #146072, Sigma Aldrich, St. Louis, Missouri, USA): 3% acrylamide and 0.06% bis-acrylamide were used for the construction of 0.5-kPa gels; 4% acrylamide and 0.3% bis-acrylamide were used for the constructions of 3-kPa gels; and 10% acrylamide and 0.1% bis-acrylamide were used for the construction of 10-kPa gels [381].

Custom-made circular biaxial stretchers were designed using computer-aided design and constructed with polycarbonate. Polydimethylsiloxane (PDMS) membranes were built by mixing the Sylgard™ 186 elastomer kit (#4026144, Dow, Midland, MI, USA), extruding onto a wafer, degassing in a vacuum chamber then curing in the oven. The PDMS membranes were treated with 10% benzophenone (#A10739, Alfa Aesar Thermo Scientific, Haverhill, MA, USA) for polyacrylamide gel adherence, as previously described by Herum *et. al* [321]. The polyacrylamide gels were constructed to be 25 mm in diameter, cross-linked through exposure to ultraviolet light for 25 minutes, attached to PDMS membranes and surrounded by silicone grease to prevent cell

migration and media leakage. The gels were equilibrated in 1X Phosphate Buffered Saline (PBS, # 10010023, Gibco Thermo Fisher Scientific, Waltham, MA, USA) overnight, then collagen I (100 μg/mL, #354236, Corning, NY, USA) was attached with 1-Ethyl-3-(3-dimethylaminopropyl) carbodiimide (#00050, Chemplex, Mahwah, MJ, USA) and N-hydroxysuccinimide (#A10312, Alfa Aesar Thermo Scientific, Haverhill, MA, USA) to facilitate cell adherence. The stretcher was assembled so that two full turns were equivalent to 10% static stretch, as previously done [291, 382]. PAAFs were trypsinized from the tissue culture plates using 0.2% Trypsin-EDTA (#25200056, Gibco Thermo Fisher Scientific, Waltham, MA, USA) and seeded onto the gels at a density of 140,000 cells per gel. Cells were cultured at 37℃, 5% CO_2, 100% humidity for three days. Cells were changed to serum-free media before being stretched for 24 hr. The stretch condition was applied for 24 hr based on the increase in gene expression shown by Herum *et al.* in left ventricular cardiac fibroblasts [321].

4.2.7. Inhibition Studies

For the inhibition experiments, PAAFs were seeded onto 0.5-kPa and 3-kPa gels at a density of 40,000 cells per gel and cultured for three days as described above. The media was changed to serum-free, and each gel slated for inhibition was pre-incubated for 4 hr with 1 μM of losartan (#3798, Tocris Bioscience, Minneapolis, MN, USA). The dose of losartan was delivered according to work by Kim *et al.* in adventitial fibroblasts from 6-week old Sprague-Dawley rats [383]. The cells were then stretched for 24 hr as previously described in the 4.2.6 subsection. RNA Isolation of these cells was conducted as described below.

4.2.8. RNA Isolation

For RNA extraction of the normotensive pulmonary artery, the adventitial layer was sectioned into 6 pieces and submerged in TRIzol by Invitrogen (#15596026, Thermo Fisher Scientific, Waltham, MA, USA). Tissue was homogenized using a BeadBug homogenizer with zirconium beads. (Benchmark Scientific). For PAAF experiments, RNA isolation was carried out using TRIzol and 5PRIME phase lock tubes (#2302830, Quantabio, Beverly, MA, USA) and RNA was extracted using the RNeasy® Mini kit (#74104, Qiagen®, Hilden, Germany) which was then reverse transcribed into cDNA using the NEB cDNA ProtoScript First Strand Kit (#E6300L, New England Biolabs, Ipswich, MA, USA). Quantitative real-time PCR was performed using the StepOnePlus™ Real-time PCR machine (Thermo Fisher Scientific, Waltham, MA, USA) and KAPA SYBR Fast Universal qPCR kit (#KK4601, Roche, Basel, Switzerland) using primers targeting genes of interest listed in Supplement S4.3 (produced by Integrated DNA Technologies, San Diego, CA, USA). Relative gene expressions were compared against housekeeping gene 18S ribosomal RNA unless otherwise noted.

4.2.9. Imaging

30,000 PAAFs were plated onto 35 mm cell culture dishes with #0 coverglass bottom (#D35-20-0-N, CellVis, Sunnyvale, CA, USA) onto 0.5-kPa and 3-kPa polyacrylamide gels, and directly onto plastic for 3 days at 37°C and 5% CO_2. Images were taken on an EVOS FL Auto 2 microscope, running software version 2.0.1732.0 (Thermo Fisher Scientific, Waltham, MA, USA). Antibodies against α-Actin Smooth Muscle Mouse (#A5228 1:100, Sigma, St. Louis, Missouri, USA) with secondary Goat anti-Mouse Texas Red (#T862, 1:250, Life Technologies, Carlsbad, CA, USA), Wheat Germ Agglutinin-488 for membrane (#W6748, 10 μg/mL, Life Technologies,

Carlsbad, CA, USA) and DAPI for nuclei in mounting media with Prolong Gold Antifade Reagent with DAPI (#P36941, Life Technologies, Carlsbad, CA, USA). Images were processed using DeconvolutionLab2 (EPFL, Lausanne, Switzerland) in ImageJ v1.53g4 developed by the National Institutes of Health (Bethesda, MD, USA).

4.2.10. Protein Quantification

10,000 PAAFs per gel were plated on 12 mm polyacrylamide gels at 0.5-kPa, 3-kPa, and 10-kPa stiffnesses formulated as described above and cultured for 3 days and fixed. Antibodies against Collagen 3a1 Rabbit (#13548-1-AP, 1:50, Proteintech, Wuhan, China) with secondary Goat anti-Rabbit AF700 (#A21038, 1:250, Life Technologies, Carlsbad, CA, USA) and against Smooth Muscle Alpha Actin (SMA) Mouse (#A5228, 1:100, Sigma, St. Louis, MO, USA) with secondary Goat anti-Mouse Texas Red (#T862, 1:250, Life Technologies, Carlsbad, CA, USA) were used to stain the PAAFs. The same imaging settings were used across cells cultured on different stiffnesses and fluorescence intensity was quantified using ImageJ v1.53g4 developed by the National Institutes of Health (Bethesda, MD, USA) and displayed as corrected total cell fluorescence (CTCF). Imaging data is added as supplementary material S4.4.

4.2.11. Statistics

Descriptive statistics were performed using JMP Pro Statistical software (version 14, SAS Institute Inc., NC, USA) for group comparisons of relative gene expression. For normally distributed data, one-way ANOVA was used to test for differences in means of three different stiffnesses and gene expression of the normotensive pulmonary artery adventitial layer for all six genes followed by the Dunnett's *post-hoc* test. Otherwise, the non-parametric Wilcoxon-Kruskal-Wallis statistic was used followed by the Dunnett's *post-hoc* test. Effects of stiffness and stretch

were tested using two-way ANOVA with stiffness and stretch as fixed factors. For normally distributed data, the Dunnett's *post-hoc* test was used. Otherwise, the non-parametric Wilcoxon-Kruskal Wallis statistic was used followed by Dunnett's *post-hoc* test. For the inhibition studies, three-way ANOVA was used to compare the effects of stiffness, stretch, and inhibition, followed by a Sidak's *post-hoc* test. Data are expressed as means ± standard error of the mean, unless otherwise specified. Statistical significance was determined at a level of $\alpha < 0.05$. Data were graphed in GraphPad Prism software (Version 8.4.3.686, San Diego, CA) and Illustrator (Adobe, Version 24.2.3).

4.3. Results

4.3.1. Model Validation

The model accurately predicted 31 out of 39 (80%) of the qualitative experimental results, including 4 out of 5 of the *in-vivo* (bolded) and 27/34 of the *in-vitro* experimental findings (Fig. 4.2A). Model accuracy went down to 35% when not using PAAF-specific pathways and using only reactions from the cardiac fibroblast model by Zeigler *et al.* (data not shown) [131].

The model was also able to predict results from *in-vitro* experiments in rat PAAFs in which TGFβ, TNFα or ROS were inhibited pharmacologically [366-367]. Each node in the model was first initialized with a default baseline value of 0.25, and the control activity of collagen I, α-SMA, fibronectin, and IL6 were computed. Next, stimulation with TGFβ and TNFα was simulated by increasing the input weights corresponding to those nodes to 0.475 and 0.375, respectively. These two values were chosen to best match the increase in relative level of α-SMA as reported by Zhang *et al.* and IL6 as reported by He *et al.* [366-367] experiment. Experiments using 10 μM of the ERK inhibitor U0126 (T+U) reduced its activity to 30% [372]. Similarly, 10 μM of the p38 inhibitor

SB203580 (T+SB) reduced p38 activity to 5% [373], the ROS scavenger N-acetyl-L-cysteine (NAC) completely blocked ROS activity [367]. Hence, after stimulation of the baseline model with TGFβ, the effects inhibiting the ERK1/2 and p38 nodes were simulated in the model by reducing y_{max} from 1.0 to 0.3 and 0.05, respectively (Fig. 4.2B-D). Similarly, the effects of NAC on TNF α were simulated by reducing the ROS node from 1.0 to 0.0 (Fig. 4.2E). Simulations ran for 24 hr [366] and 8 hr [367] to match the time-course of the corresponding experimental measurements, as depicted in Fig. 4.2B-E.

Figure 4.2| Model prediction of qualitative input-output experiments and inhibition results signaling. (A) Input–output validation: model predictions agreed with published experimental observations for 31 out of 39 (80%) of the input–output responses measured in rat or human PAAFs. Intermediate and phenotypic output results are organized by input stimulus, where the bolded node names indicate experimental results that were measured *in vivo*. (B–E) Inhibition validation: results of the PAAF model are compared with the results of inhibition experiments in cultured rat PAAFs reported by Zhang et al. (B–D) [76] and He et al. (E) [77]. Each model prediction was normalized to the baseline condition obtained when all inputs were 0.25. Stimulation with TGFβ and TNFα were simulated by increasing these inputs to 0.475 and 0.375, respectively, to be consistent with the experimental protocol. The effects of the ERK inhibitor (T+U), p38 inhibitor (T+SB) and ROS scavenger (NAC) were simulated by decreasing ymax for those nodes from 1.0 to 0.3, 0.05 and 0, respectively, consistent with the published reports [83,84]. (Online version in color.)

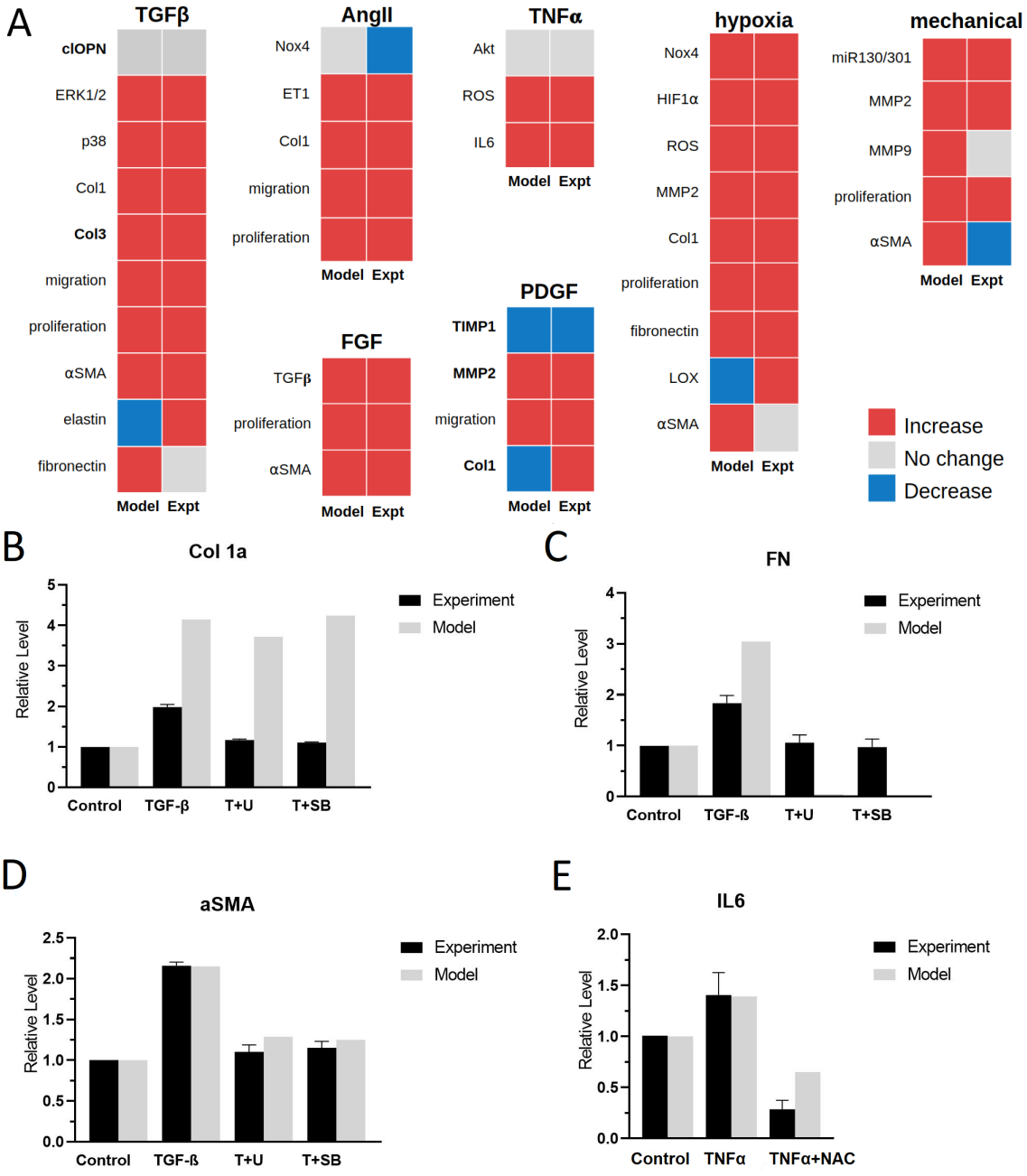
A
TGFβ
clOPN
ERK1/2
p38
Col1
Col3
migration
proliferation
αSMA
elastin
fibronectin
Model Expt
AngII
Nox4
ET1
Col1
migration
proliferation
Model Expt
TNFα
Akt
ROS
IL6
Model Expt
hypoxia
Nox4
HIF1α
ROS
MMP2
Col1
proliferation
fibronectin
LOX
αSMA
Model Expt
mechanical
miR130/301
MMP2
MMP9
proliferation
αSMA
Model Expt
FGF
TGFβ
proliferation
αSMA
Model Expt
PDGF
TIMP1
MMP2
migration
Col1
Model Expt
Increase
No change
Decrease
B
Col 1a
Relative Level
Experiment
Model
Control
TGF-β
T+U
T+SB
C
FN
Relative Level
Experiment
Model
Control
TGF-ß
T+U
T+SB
D
aSMA
Relative Level
Experiment
Model
Control
TGF-ß
T+U
T+SB
E
IL6
Relative Level
Experiment
Model
Control
TNFα
TNFα+NAC

Percent errors between model-predicted and experimental results for collagen I expression stimulated by TGFβ and with TGFβ in the presence of the ERK1/2 and p38 inhibitors were 109%, 218%, and 283%, respectively [366]. Although these errors were high, the model did qualitatively predict the observed increase in collagen I stimulated by TGFβ but not the observed inhibitory effects of either inhibitor. This may be because of incomplete or inaccurate interaction logic in the module of the network regulating collagen I expression. On the other hand, the model did correctly predict observed trends for fibronectin with % errors of 66%, -95%, and -99%, though predicted inhibition was greater than observed, perhaps because only MAPK signaling regulates fibronectin in the model. Because the model simulation was matched to the α-SMA experimental results, the error for TGFβ stimulation was only -0.4%, and there was a good match with the inhibition results with % errors of 16.7% for T+U (ERK1/2 y_{max} to 0.3) and 8.4% T+SB (p38 y_{max} to 0.05) [366]. This shows that the model was able to closely predict the trends in α-SMA and fibronectin activity. Changes in the model structure may be required before collagen I expression can be predicted.

We compared the model to experiments in which TNFα was added to rat PAAFs [367] by increasing the TNFα node from 0.25 to 0.375. The error in the predicted increase in IL6 expression was only -1.1%, and the predicted effect of adding the ROS scavenger was qualitatively similar to observation, with an error of 128% (Fig 4.2E).

All model results were significantly different ($p < 0.05$) than experimental means except those for α-SMA (Fig. 4.2D. A Student's heteroscedastic t-Test produced p-values of 0.06 for α-SMA stimulation and ERK inhibitor (T+U) and 0.16 for α-SMA stimulation and p38 inhibitor (T+SB) given the sample size (n=3) and standard deviation reported in the original experimental paper [366].

4.3.2. Sensitivity Analysis

A sensitivity analysis was used to identify the nodes that are the most influential determinants of network state under baseline conditions and conditions of high-mechanical stimulation as occurs in PAH. The change in the steady-state (200 min) response of each node in the network (columns) to 100% knockout of each node individually (rows) is displayed as a heat map in Fig 4.3. The analysis shows that mechanical stimulation, hypoxia, AngII, and TGFβ are the most important inputs. Important intermediate regulators include the mitogen-activated protein kinases (ERK1/2, JNK1/2 and p38), calcineurin, the Smads 2 and 3, cleaved osteopontin (clOPN), reactive oxygen species (ROS), notch intracellular domain (NICD), nitric oxide (NO), and NADPH oxidase 4 (Nox4). This sensitivity analysis has thus revealed the larger influence of hypoxia and FGF in the PAAF model than in the model of cardiac fibroblasts [131].

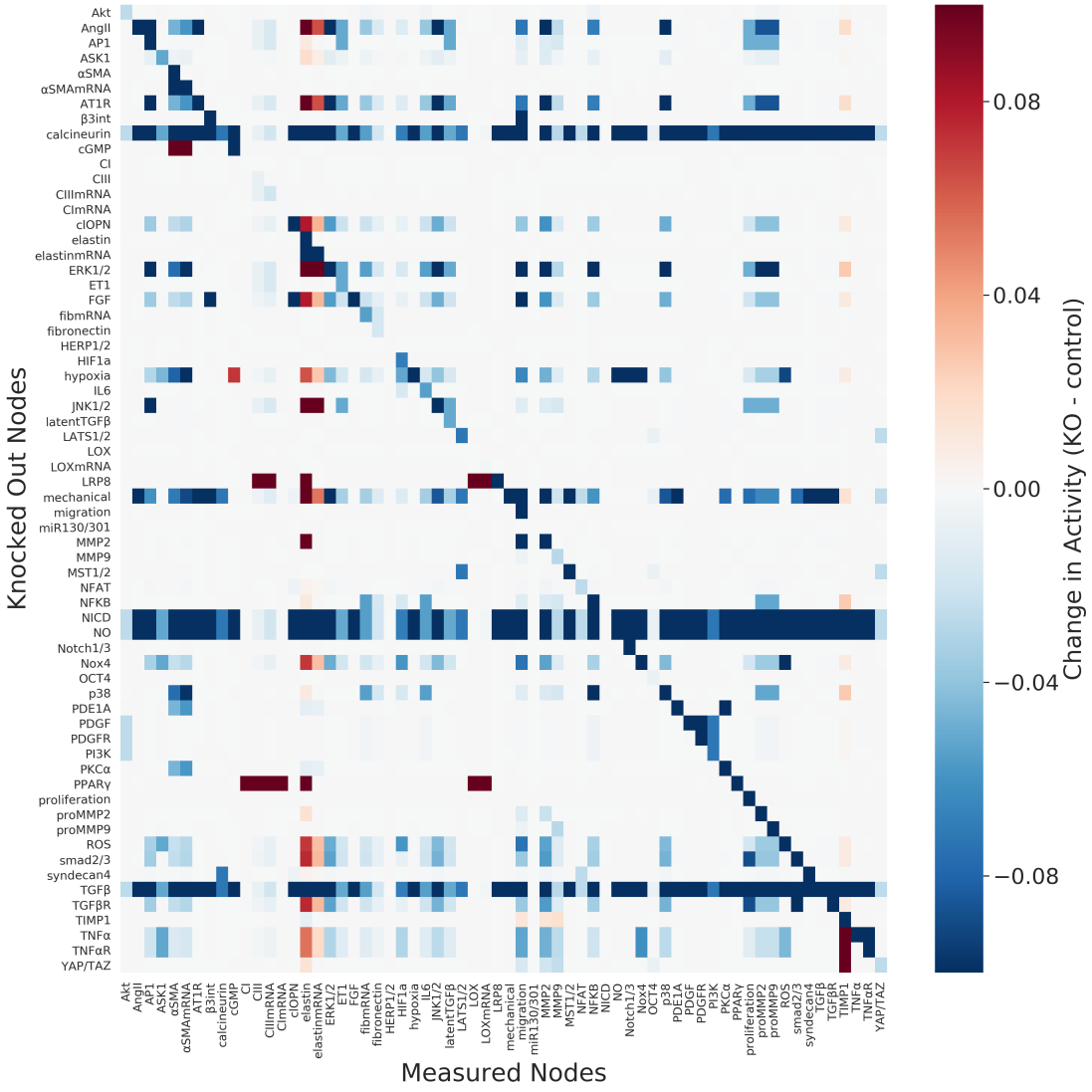

Figure 4.3| Heatmap of the baseline sensitivity analysis. Heatmap of the baseline sensitivity analysis showing changes in activity of all the nodes in the model (columns) in response to knocking out each node (rows), where red indicates an increase in activity over baseline and blue shades indicate a decrease in activity in response to the knockout. (Online version in color.)

Given the importance of mechanical loading and vessel stiffening in the pathogenesis of pulmonary arterial fibrosis, we repeated the sensitivity analysis in the context of high-mechanical load by increasing the input weight of the mechanical stimulation input node from the baseline value of 0.25 to 0.9 as shown in electronic supplementary material, S4.5. Under these conditions,

the most influential unique nodes were found to be α-SMA, cGMP, ET1, proteins in the Hippo pathway, and syndecan4. These nodes are highly active in mechanotransduction, proliferation, vasoconstriction, and activation of fibroblasts into the myofibroblast phenotype [321]. Knocking out these nodes generally resulted in a decrease in matrix proteins including collagen III and fibronectin. This global sensitivity analysis is also a way to elucidate the likely determinants of greatest structural and parameter uncertainty in the model. In the following sections we investigated the effects of parameter and network uncertainty in the model.

4.3.3. Quantification of Parameter Uncertainty

In order to examine the effect of propagated uncertainty of model parameters on the accuracy of the model, a table of the 39 experimental results was coded to compare results against. The accuracy was compared with the baseline 80% accuracy achieved with default model parameters.

Each parameter was varied independently using a uniform distribution n ~ (1.36-2.36), EC_{50} ~ (0.4-0.7), ω ~ (0.1-0.4). A (quasi-)Monte Carlo method with 5,000 model evaluations was used for UQ analysis of n and EC_{50} to cover the 99 uncertain reactions, and an order-4 polynomial chaos expansion was used for the weight ω of the 7 model inputs. As seen in Figure 4, the distribution of model accuracy for input weight has a mean of 70.4%, standard deviation of 5.3%, a minimum accuracy of 66.67%, and a maximum accuracy of 79.5%. For EC50, the mean of the distribution is 65.4% with a standard deviation of 19.2% and a minimum accuracy of 20.5% and maximum accuracy of 82%. For the Hill coefficient, the mean accuracy of the distribution was 63.9% with a standard deviation of 13.3%, a minimum accuracy of 20.5%, and a maximum

accuracy of 79.5%. This indicates that network model accuracy was most vulnerable to uncertainty in n, somewhat vulnerable to uncertainty in EC_{50} and relatively robust to input weight uncertainty.

A subset of specific combinations of input weights over the range of 0.1-0.4 did result in a decrease in accuracy including a combination of low mechanical and low hypoxia or a combination of low AngII, TGFβ and FGF, but these did not decrease the model accuracy more than 13% (Fig 4.4A).

There was a wide range of changes in model accuracy as shown in Fig 4.4B, over the relatively large range of n of 1.36-2.36, showing increased uncertainty propagation. Lower model accuracy (<40%) was observed when more than 30% of the 99 reactions had Hill coefficients n exceeding 2.2. In order to allow EC_{50} to vary, n was set to 2 as stated in the Methods to avoid numerical errors [173].

Model accuracy was generally high and robust to varying EC_{50} from 0.4-0.7, but there was a secondary peak at 20% as seen in Fig 4.4C. The low peak occurred when the reactions of MST1/2 activating LATS1/2 and miR130/301 inhibiting LRP8 both had EC_{50} values greater than 0.68. Both reactions are involved in the Hippo pathway, which is activated by mechanical stimulus. Finally, there was a set of EC_{50} values that led to an increased model accuracy of 82%. When compared with thousands of combinations that produced an 80% accuracy. This result is unique in that all of the inputs and hypoxia -> Nox4 were not extreme values ($0.42 < EC_{50} < 0.68$)

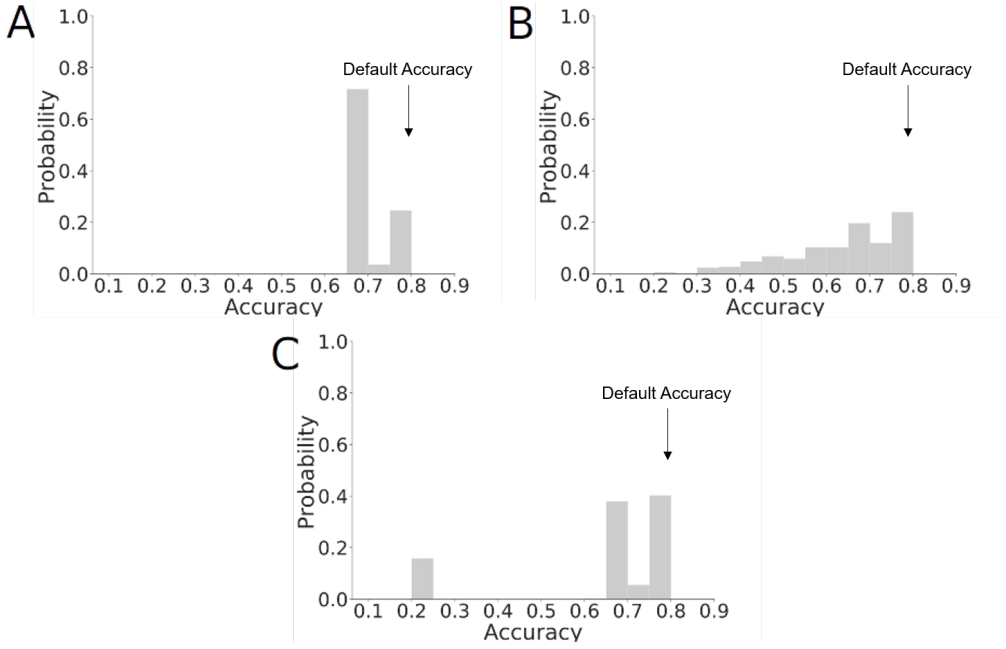

Figure 4.4| Uncertainty quantification of parameters. Quantification of the effects of model parameter uncertainty on the probability of qualitative model prediction accuracy assuming uniform random distributions of input weights w (a), Hill coefficients n (b), and half-maximal activations EC50 (c). Accuracy with using default parameters is annotated. Varying input weight w randomly between 0.1 and 0.4 for seven inputs using polynomial chaos expansion with a fourth order produced accuracies between 70% and 80%, whereas varying the Hill coefficient n from 1.36 to 2.36 for all 99 reactions using the (quasi-)Monte Carlo method resulted in a much wider distribution of model accuracies ranging from 20% to 80%. Varying EC50 randomly between 0.4 and 0.7 for all 99 reactions using the (quasi-)Monte Carlo method resulted in peaks in accuracy at around 20% and at 70–80%.

combined with a high EC_{50} (>0.68) for the reaction: MMP9 and latentTGFβ activating TGFβ and a low EC_{50} (<0.42) for the reaction: proMMP9 activating MMP9 and TIMP1 inhibiting MMP9. This finding demonstrates how further tuning can be done by optimizing model parameters.

The 11 inhibition results seen in Fig 4.2B-E (activation by TGFβ and TNFα then inhibition of p38, ERK1/2 or ROS) were coded with a threshold of 0.05, and UQ was repeated using polynomial chaos expansion with an order-4 varying the 7 input weights from 0.1-0.4. Supplement S4.6 shows that the predicted results of inhibition experiments were relatively robust to this change, accurately predicting 9/11 (82%) or 8/11 (73%) of the activation by TGFβ and TNFα and inhibition of p38, ERK1/2, and ROS. However, the model was not able to capture the inhibition of collagen I by p38 or ERK1/2.

4.3.4. Quantification of Epistemic Uncertainty

To use UQ to evaluate the level of uncertainty associated with the cell type used in the model construction, a reduced version of the model was created with only experimental data reported for fibroblast cells from the cardiovascular system, specifically PAAFs and cardiac fibroblasts (CFBs). This new criterion led to a reduced model with 82 reactions and 62 nodes, due to the removal of ET1 and latentTGFβ, versus the 92 reactions and 64 nodes in the original model (electronic supplementary material, S4.1). The reduced model was qualitatively compared against the same independent set of data as the full model. Here the accuracy went down to 24/38 (63%) from the accuracy of 31/39 (80%) for the original model. The number of experiments compared against drops down from 39 to 38 as a result of ET1 being a node in the input-output comparison.

We ran a (quasi-)Monte Carlo simulation with 10,000 model evaluations where n was given a uniform distribution from 2 to 2.4, EC_{50} was given a uniform distribution of 0.4 to 0.7

(default value of 0.6), and the input weight ω was given a uniform distribution of 0.1 to 0.4 (default value of 0.25) as depicted in Fig. 4.5A.

We further compared the two models by varying all three parameters at once: n ~ U(2, 2.4), EC_{50} ~ U(0.4, 0.6), and ω ~ U(0.1, 0.4). The mean accuracy of the baseline model (Fig 4.5A) was 35.7% with a standard deviation of 18% and reaches a maximum accuracy of 80%, while the mean accuracy of the reduced model (Fig 4.5B) was 38.4% with a standard deviation of 12% and a maximum accuracy of 63%. Overall, this result suggests that while using data from non-cardiovascular cell types is a source of epistemic uncertainty, the additional model components and reactions deduced from these other cell types can improve prediction accuracy without significantly compromising robustness. These results may help to prioritize new *in-vitro*

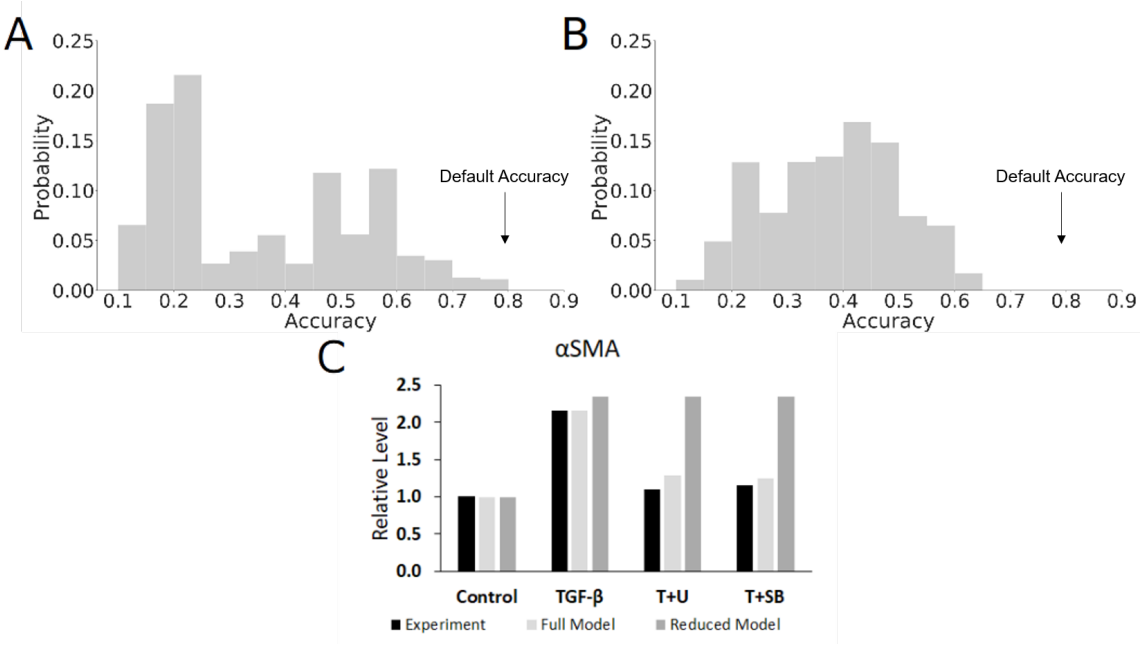

Figure 4.5| Quantification of epistemic uncertainty of network structure signaling. Results of a 10000 model evaluation runs using the (quasi-)Monte Carlo simulation where the Hill coefficient n was a uniform random variate between 2 and 2.4, EC_{50} was given a uniform distribution of 0.4 to 0.6, and w was varied according to a uniform random distribution of 0.1 to 0.4. The two models being compared are the UQ results for the full model (a) versus the reduced model (b) based only on literature data from cardiovascular cells (PAAFs and CFBs) with accuracy using default parameters annotated. Inhibition results for α-SMA using the reduced model were run under the same conditions used to produce figure 2d (c). Results remained unchanged for the other outputs (collagen I, fibronectin, IL6) as seen in electronic supplementary material, S4.6.

experiments in PAAFs that are not available in the literature but are important to the accuracy of the model.

This includes experiments on the feedback from and activation of latent TGFβ, activation of TIMP1 and ET1 by AP1, activation of elastin mRNA by PKCα, activation of HIF1α by ROS, and activation of α-SMAmRNA by p38.

To examine the effects of only including cardiovascular fibroblast data (PAAFs and CFBs) on the inhibition results, simulations were rerun with the same conditions as in Figure 4.5B-E. Briefly, input TGFβ = 0.475, and TNFα = 0.375, ERK1/2 y_{max} = 0.3, p38 y_{max} = 0.05, ROS y_{max}

= 0, and at 24 hr and 8 hr, respectively. While other trends remained the same as shown in electronic supplementary material, S4.1, the reduced model resulted in a qualitative reversal of the accuracy for α-SMA predicted by the full PAAF model. As shown in Fig 4.5C, there was no longer a decrease in activity in α-SMA due to ERK and p38 inhibitors as originally observed. The reduced form of the model only agrees with the increase in α-SMA due to TGFβ stimulation. The results also no longer match the experiment, producing p values that were less than 0.05 with a heteroscedastic Student's t-Test, rejecting the null hypothesis that the model results lie in the same distribution as the experimental ones [366]. Thus, the full model, despite including some information from non-cardiovascular fibroblasts, better captures the complex regulation of α-SMA expression.

4.3.5. Revised Computational PAAF Network Model

We used the model described in section 4.2.1 to investigate how substrate stiffness and stretch regulate profibrotic gene expression in PAAFs [379]. The mechanical stimulus input was divided into substrate stiffness and stretch inputs, where stretch activated integrin β_3, AngII, MST1/2, and TRP; and stiffness activated integrin β_3, Ang II, MST1/2, TGF-β, and Syndecan-4 [111, 113, 158, 327, 329, 346, 384]. We also added details to the activation of mitogen activated protein kinases (MAPKs) to allow independent regulation of JNK1/2, p38, and ERK1/2 [125-133]. In this refined model, ASK1 regulates JNK1/2 as well as ERK1/2 [125-126]. Ras was added downstream of AT1R to mediate regulation of ERK1/2 and JNK1/2 [127-128]. Based on studies by Xie *et al.* [129] in adult rat cardiac fibroblasts, activation of JNK1/2 by cleaved osteopontin (clOPN) was included. The TGF-β receptor now also activates p38 via the TGF-β –activated kinase (TAK1) [130] and TGF-β receptor also activates *Eln* through smad2/3 based on work in

PAAFs by Rabinovitch *et al.* [145]. Based on a model of cardiac fibroblasts by Zeigler *et al.* [131] and papers on MAPK signaling [132-133], we included ROS activation of p38. Finally, we incorporated the activation of TRP channels TRPC6 and TRPC1/C5 by stretch, which allows calcium to activate Protein Kinase C alpha (PKCα) [163-164, 318]. Given the scarcity of PAAF studies, the network includes reactions from fibroblasts not derived from pulmonary arteries, such as cardiac and lung fibroblasts. The updated network is displayed in Fig. 4.6.

The input weights of stretch and stiffness were both set to 0.25 to represent the softest matrix, 0.5-kPa, and no applied stretch. We increased the stiffness input weight to 0.7 and 0.9 to represent the effects of 3-kPa and 10-kPa substrates, respectively, and evaluated the model at t=72 hr to mimic the *in-vitro* experimental time course. Similar to the network model analysis by Tan *et al.*, we chose a change in normalized model output values of 0.1 as the threshold for considering the output to have changed significantly by mechanical stimulation or for a significant response to have been significantly inhibited [172]. While Tan *et al.* used a threshold of 0.05, we chose a more stringent threshold of 0.1, but our conclusions were not affected by this difference. Parameters in the model have not been optimized or fitted. Rather we chose equal parameters for all reactions using values from Zeigler *et al.* [131]. While the parameters EC_{50}, weight, and Hill coefficient were set to be the same value across all reactions, the time constant τ was chosen according to the

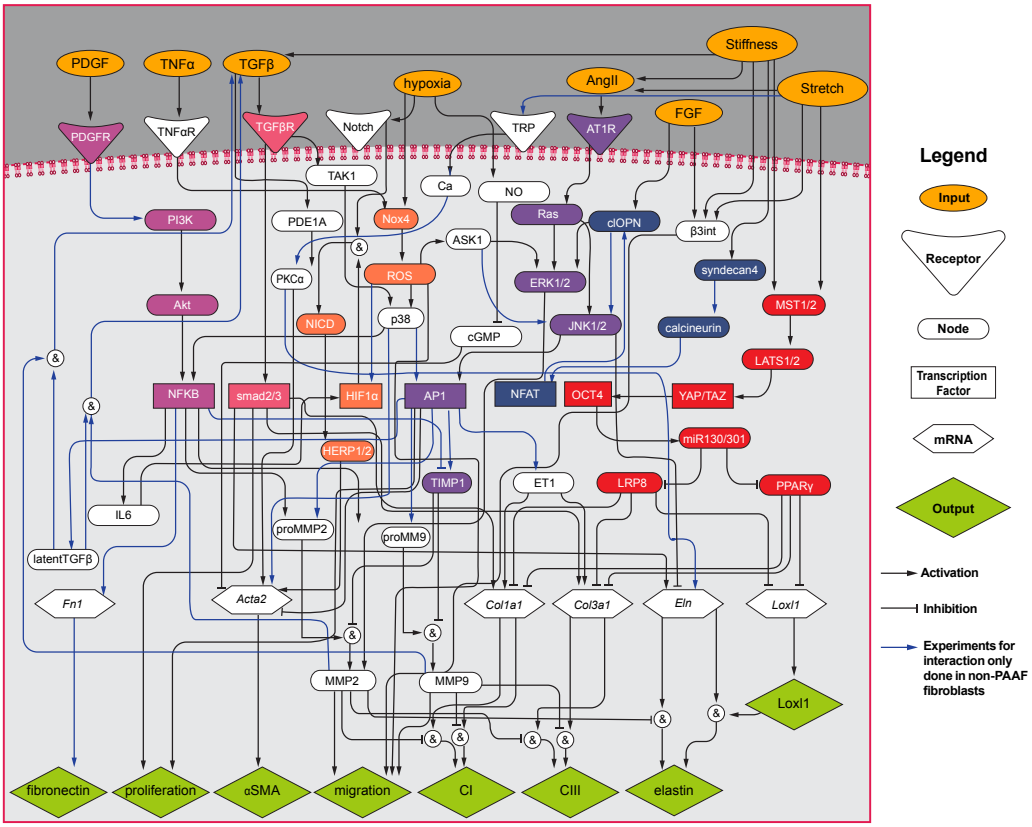

Figure 4.6| The revised PAAF signaling network model. PAAF mechanosignaling network with 8 input stimuli (orange ovals), 6 receptors (triangles), 34 nodes (ovals), 7 transcription factors (rectangles), 6 messenger RNAs (hexagons), and 8 phenotypic outputs (green diamonds), modified from our previous work [378]. Activation is shown with arrows and inhibition is shown with blunt head arrows. Blue arrows indicate non-PAAF-based experiments. Magenta nodes indicate the Phosphoinositide 3-kinase (PI3K) pathway, orange nodes indicate the Reactive Oxygen Species (ROS) pathway, purple nodes indicate the mitogen-activated protein kinase (MAPK) pathway, blue nodes indicate the calcineurin pathway, and red nodes indicate the Hippo signaling pathway.

type of reaction. Furthermore, parameter values were tested for consistency with the mathematical constraints described in Cao *et al.* for this class of model [318]. In a previous comprehensive analysis of parameter uncertainty, we verified that model accuracy was robust to the choices of these parameter values [379].

To numerically simulate the effects of stretch on PAAFs after 24 hr and the changes in substrate stiffness for 72 hr when inhibiting nodes, the model was evaluated at those time points (i.e., $y_i(t=24)$ and $y_i(t=72)$) after the corresponding input weights of stiffness and stretch were increased from 0.25 to 0.7. To simulate the effects of inhibition, $y_{i,max}$ corresponding to blocked nodes were set to 0, while the other parameters remained the same. The change for each gene was calculated with respect to each condition's control group.

To simulate the different conditions under which losartan inhibited AT1R, we conducted eight sets of simulations. Four sets of these simulations were evaluated on 0.5-kPa substrate stiffness for 72 hr with parameters at baseline, and input weights stiffness and stretch set to 0.25. For simulations involving stretch but no inhibition, the input weight of stretch was increased from 0.25 to 0.7 and the model was evaluated at t=24 hr. For the unstretched and stretched inhibited conditions, $y_{i,max}$ corresponding to the AT1R node was set to 0 before applying changes to the stretch input weight and evaluated at t=24 hr. The same combinations were used for the other four set of simulations on 3-kPa substrate conditions, but with a stiffness input weight of 0.9.

4.3.6. PAAFs Upregulate Profibrotic Genes in Response to Increased Substrate Stiffness and Stretch

When we immunostained cultures for markers of endothelial cells (vWF), smooth muscle cells (MYH11), and myofibroblasts (vimentin) (Fig. 4.7A-H), only 3% were positive for vWF and 0.2% were positive for MYH11 suggesting high enrichment of PAAFs in our cell cultures. Intact PA tissue sections were stained and imaged with the same antibodies and imaging settings as positive controls for these markers (Fig. 4.7I-R).

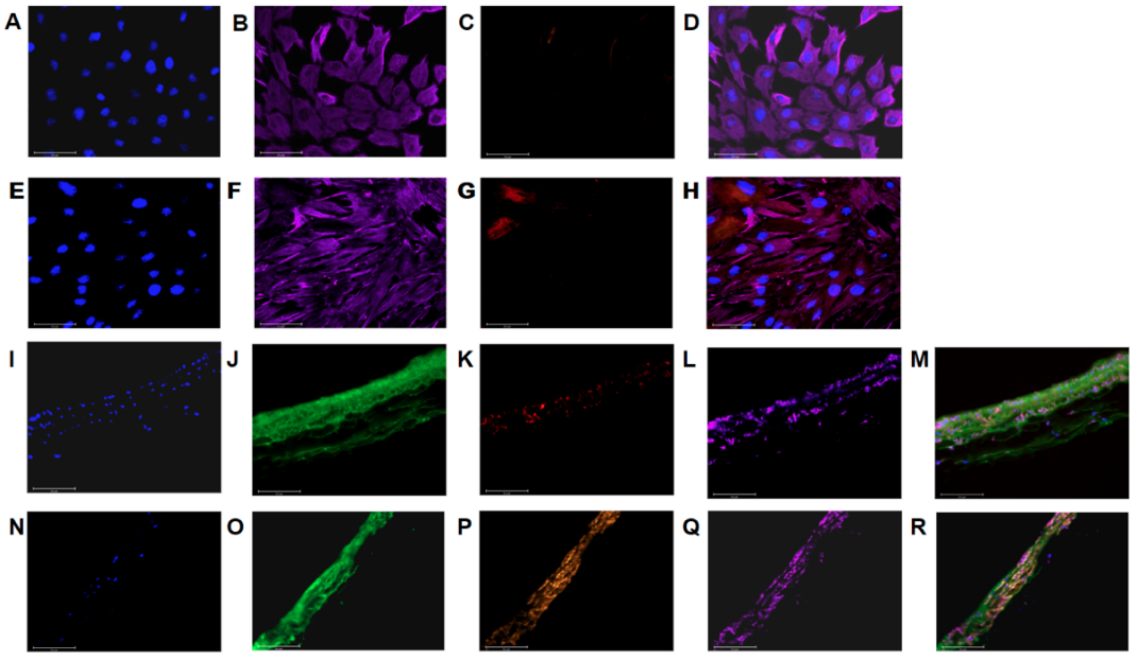

Figure 4.7| The enrichment study of PAAFs in cell cultures. The cell culture showed positive labeling for (A,E) DAPI, (B,F) vimentin, (C) vWF, and (G) MYH11 with (D,H) overlays. Out of 425 isolated cells, 3% expressed vWF, and out of 888 cells 0.2% expressed MYH11 and 100% expressed vimentin with representative images shown in (A–H). Immunostained PA tissue sections showed positive labeling for: (I) DAPI, (J) WGA, (K) vWF, (red), and (L) vimentin(magenta) with an (M) overlay. Separate immunostained PA tissue sections showed positive labeling for: (N) DAPI, (O) WGA, (P) MYH11 (orange), and (Q) vimentin (magenta) with an (R) overlay. These samples were used as labeling controls to estimate purity of a cell culture expanded on plastic. Images were all acquired at 40× magnification, scale bar 50 um.

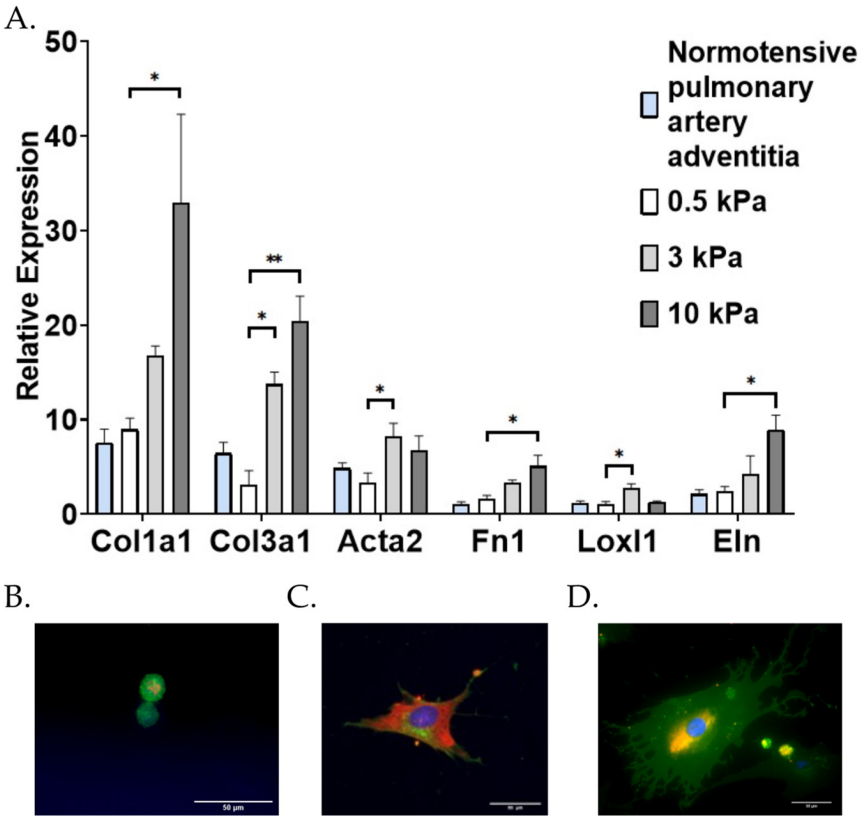

Figure 4.8| Effect of substrate stiffness on PAAF differentiation. Mean ± standard errors of the mean relative to housekeeping gene 18S ribosomal RNA of PAAFs cultured at different stiffness (n = 9) compared with gene expression of sections in a normotensive pulmonary artery adventitia (n = 6). Effect of stiffness (* $p < 0.05$ and ** $p < 0.0001$) by one-way analysis of variance (ANOVA) compared with control 0.5 kPa with a post-hoc Dunnett's test. (B–D) PAAFs plated on (B) 0.5 kPa (40×), (C) 3 kPa (20×) polyacrylamide gel and (D) plastic (40×), scale bar 50 µm. Cells were stained with DAPI, which stains the nucleus (blue), wheat germ agglutinin stains the membrane (green), and α-SMA filaments (orange).

PAAFs expanded on plastic reverted from a myofibroblast to a fibroblast phenotype after three days of culture on 0.5-kPa stiffness 6-well plates, as assessed by their low expression of *Acta2* (Fig. S4.1) and their rounded appearance in culture (Fig. 4.8B) compared with the more stellate shapes and higher *Acta2* expression in cells grown on stiffer substrates (Fig. 4.8C-D). Messenger RNA levels of *Col1a1*, *Col3a1*, *Eln*, *Fn1*, *Loxl1*, and *Acta2* genes in fibroblasts cultured on 0.5-kPa substrates, were not significantly different from those obtained by extracting RNA from the

pulmonary artery adventitia of a normotensive rat ($p>0.05$ by one-way ANOVA, Fig. 4.8A). This finding suggests that cells cultured on a 0.5-kPa substrate may mimic expression of PAAFs *in-vivo* with respect to the six genes studied in this paper.

Compared with mRNA levels in PAAFs cultured on 0.5-kPa substrates, all six genes were significantly upregulated in response to increased matrix stiffness ($p<0.05$ by one-way ANOVA and Dunnett's *post-hoc* test). The expression of *Acta2* and *Loxl1* was significantly higher on cells grown on 3-kPa matrices but not significantly higher on cells grown on 10-kPa matrices, while *Col1a1*, *Col3a1*, *Eln*, and *Fn1* were significantly upregulated on 10-kPa substrates (comparable to arterial stiffness in advanced PAH [380]), compared with PAAFs cultured on 0.5-kPa matrices (Figure 4.3A). Interestingly, *Acta2* and *Loxl1* expression exhibited non-monotonic responses, with significant upregulation of gene expression on 3-kPa matrices compared with the 0.5-kPa matrices, but no significant difference between cells cultured on 0.5-kPa and 10-kPa matrices.

Examining the transcriptional responses of the six genes to 10% equibiaxial stretch for 24 hr in PAAFs (Fig. 4.9A-F), *Col1a1*, *Col3a1*, *Eln*, *Loxl1* and *Acta2* were significantly upregulated compared with unstretched cells independent of the substrate stiffness ($p<0.05$ based on group comparisons made using a two-way ANOVA). Although *Fn1* expression did not significantly change after 24 hr of stretch (Fig. 4.8D), it was significantly upregulated after 4 hr on all gel stiffnesses (from 1.62±0.34 to 5.07±1.22 on 0.5-kPa gels, 3.36±0.26 to 6.93±1.65 on 3 kPa gels and 5.08±1.16 to 8.04±2.32 on 10-kPa gels, $p=0.0002$, $n=6$). On the other hand, *Col1a1* was only significantly upregulated after 24 hr of stretch, but not after 4 hr. This suggests *Fn1* is transiently induced by a short period of stretch, while the *Col1a1* response to

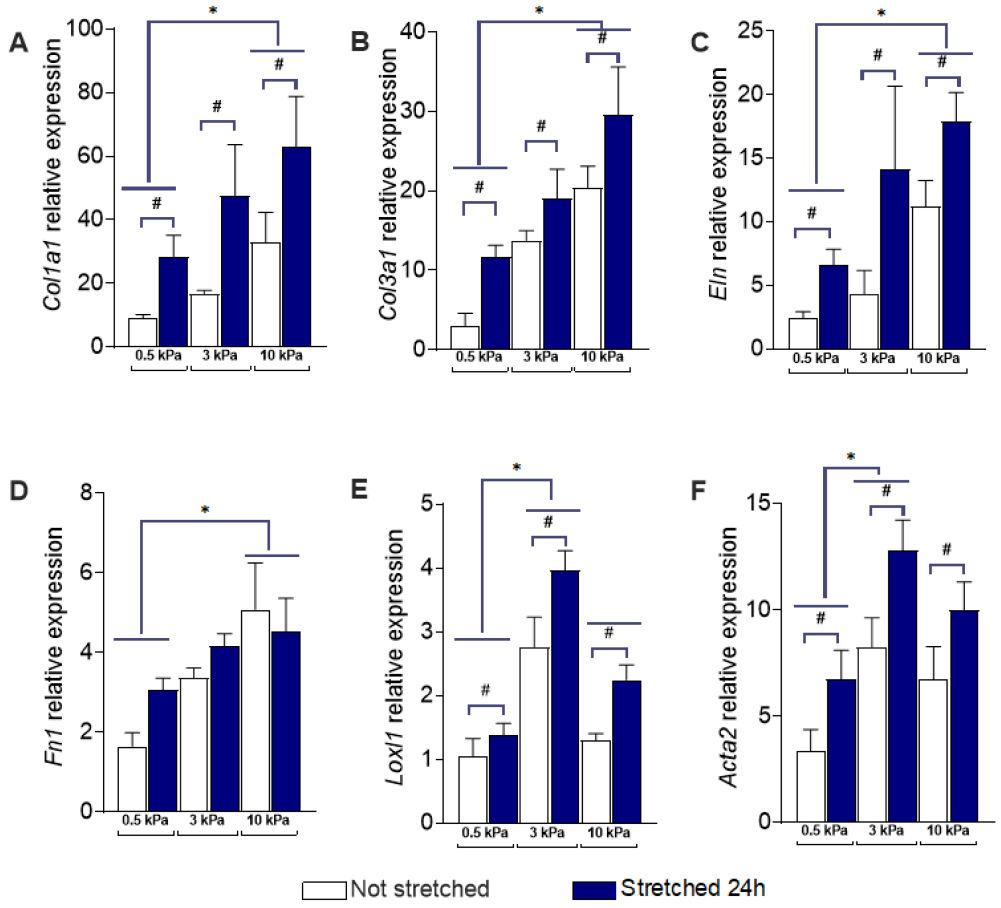

Figure 4.9| Effect of stiffness and stretch on gene expression in PAAFs. Mean ± standard errors of the mean of mRNA levels relative to housekeeping control gene 18S ribosomal RNA in unstretched cells (n = 9, white bars) and after 24 h 10% equibiaxial stretch (n = 12, blue bars). *Significant pairwise effect of stiffness ($p < 0.05$) by a post-hoc Dunnett's multiple comparisons test and # significant effect of stretch ($p < 0.05$) based on group comparisons made using a two-way analysis of variance (ANOVA) for: (A) Collagen I (Col1a1) (B) Collagen III (Col3a1) (C) Elastin (Eln) (D) Fibronectin (Fn1) (E) Lysyl oxidase-like 1 (Loxl1) (F) Smooth Muscle Actin (Acta2).

Table 4.1| Two-way ANOVA of the effects of substrate stiffness and stretch on the expression of six genes in cultured PAAFs. Bolded values indicate p<0.05.

Genes	Effects of Stiffness	Effect of Stretch	Interaction Term
Col1a1	**0.046**	**0.006**	0.86
Col3a1	**<0.0001**	**0.012**	0.69
Eln	**0.009**	**0.009**	0.66
Fn1	**0.001**	0.27	0.28
Loxl1	**<0.0001**	**0.0007**	0.30
Acta2	**0.0007**	**0.002**	0.88

stretch is much slower. This finding is consistent with reports identifying Fn1 as an early response gene [385]. No significant interaction effects between substrate stiffness and stretch were found in the expression of any of the six genes (Table 4.1).

Increased ECM stiffness significantly upregulated protein expression of Collagen III and Smooth Muscle Actin (SMA) from a baseline of 0.5-kPa at both 3-kPa and 10 kPa based on a *post-hoc* test (Fig. 4.10). There was no significant difference between 3-kPa and 10-kPa protein expression for either Collagen III or SMA. This is consistent with the changes in relative

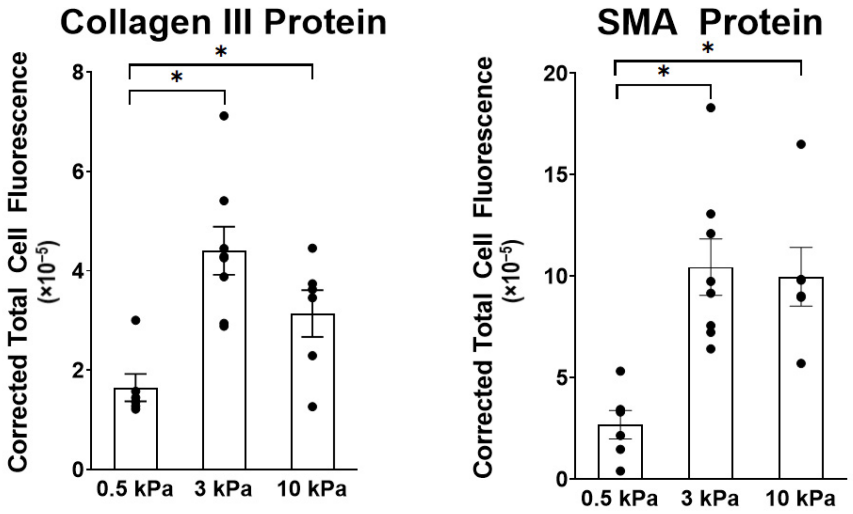

Figure 4.10| Effect of stiffness on protein expression of Collagen III and SMA in PAAFs. Mean ± standard errors of the mean of Corrected Total Cell Fluorescence (CTCF) for 6–8 replicate hydrogels. *Significant pairwise effect of stiffness ($p < 0.05$) determined by one-way analysis of variance (ANOVA).

expression of RNA for Collagen III (*Col3a1*) and SMA (*Acta2*) shown in Fig. 4.9B, F, which showed significant increases from 0.5-kPa to 3-kPa, and no further significant increase from 3-kPa and 10-kPa substrates.

4.3.7. PAAF Network Model Simulates Gene Expression Activated by Stiffness and Stretch

A threshold change of 0.1 in the normalized variable representing each of the six genes was used to classify the change in each gene as significant. The model predicted significant upregulation of all six genes in response to an increase in substrate stiffness from 0.5-kPa to 3- or 10-kPa (Figure 4.11). These model predictions matched our experimental observation that all six

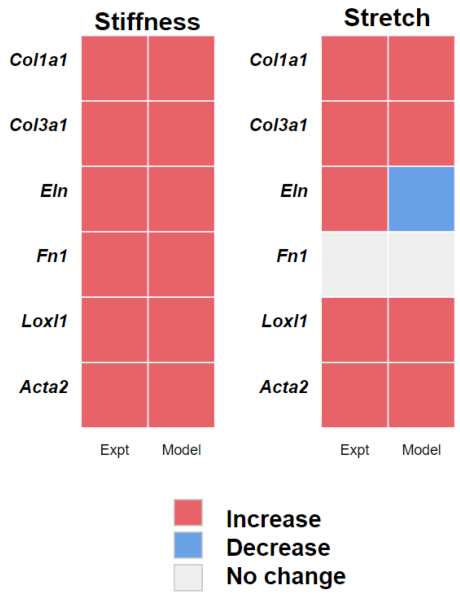

Figure 4.11| Comparison of the experimental observations (Expt) with model predictions (Model) of gene activity due to stretch and stiffness. Increase (red), decrease (blue), and no change (grey) in gene predicted by the model is based on a threshold of 0.1 and experimental observations that reached a significant difference 24 hr after stretch ($p < 0.05$).

genes were significantly upregulated in cells grown on stiffer matrices.

The model also predicted upregulation of the gene expression of *Col1a1*, *Col3a1*, *Loxl1*, and *Acta2* and the return to baseline of *Fn1* expression 24 hr after induction by 10% equibiaxial

stretch. However, the model predicted *Eln* expression to be downregulated with stretch while experimental results showed upregulation. We investigated whether the inhibitory effect of JNK1/2 on *Eln* may have outweighed the activating effect of PKCα and found that decreasing the weight of the inhibition of JNK1/2 on *Eln* [386] by 50% allowed the model to predict the observed upregulation of *Eln* (Figure 4.9). While the model was in qualitative agreement with the data, it did not recapitulate the non-monotonic responses of *Loxl1* and *Acta2* (Figure 4.8A), which were significantly upregulated by 3-kPa matrix stiffness (compared with 0.5-kPa) but not by 10-kPa substrates.

4.3.8. Angiotensin II Receptor Inhibition Unmasks an Interaction Between Stiffness and Stretch on Fibronectin Gene Expression

Based on a sensitivity analysis [379], we simulated the effects of stretch and increased stiffness in the presence of inhibitors of three mechanosensitive nodes in the model (AT1, and TGF-β, and MST1/2). Table 4.2 shows the effects of inhibiting AT1, TGF-β, and MST1/2 on changes in gene expression due to an increase in substrate stiffness from 0.5 and 3-kPa and due to stretch on 0.5 kPa stiffness matrices. Here, model-predicted differences in the normalized mRNA variable due to inhibitor treatments were considered significant if they exceeded a threshold of 0.1.

Table 4.2| Changes in gene expression due to inhibition of selected receptors in response to stiffness and stretch PAAFs). Numbers in bold indicate activity changes greater than a threshold of 0.1.

Genes	Effects of Stiffness on 3kPa			Effect of Stretch on 0.5 kPa		
	AT1	**TGF-β**	**MST1/2**	**AT1**	**TGF-β**	**MST1/2**
Col1a1	**-0.16**	**-0.24**	**-0.10**	**-0.14**	-0.06	**-0.26**
Col3a1	**-0.16**	**-0.24**	**-0.10**	**-0.14**	-0.06	**-0.26**
Eln	-0.04	**-0.46**	0	**0.20**	-0.08	0
Fn1	**-0.15**	**-0.39**	0	-0.01	-0.03	0
Loxl1	0	0	**-0.37**	0	0	**-0.37**
Acta2	**-0.14**	**-0.70**	0	-0.04	**-0.14**	0

From the model simulations, the induction of *Loxl1* expression by increased substrate stiffness is specifically regulated by MST1/2 signaling, whereas the responses of the other five genes to stiffness were all significantly inhibited by blocking TGFβ receptor. AT1 receptor inhibition significantly attenuated the stiffness-dependent induction of *Col1a1*, *Col3a1*, *Fn1* and *Acta2*, but had no significant effect on *Eln* or *Loxl1*, and the magnitude of inhibition was noticeably less than when TGFβ receptors were blocked. Blocking angiotensin signaling in the model with increased substrate stiffness downregulated the collagens by 20% and blocking TGFβ signaling downregulated the collagens by 30%, while blocking angiotensin downregulated *Acta2* by 17% and blocking TGFβ downregulated it by 86% (Table 4.2).

Blocking TGFβ signaling in the model while applying stretch stimulation suppressed the upregulation of *Acta2* by 28% and reduced the downregulation of *Eln* by 11%. Stretch induction of *Col1a1* and *Col3a1* was shown to be reduced by inhibition of MST1/2 (by 46%) and angiotensin II signaling (by 26%), while *Loxl1* regulation by stretch was affected only by inhibiting MST1/2 (by 100%). *Fn1* expression, which was not significantly altered by stretch, remained unchanged

in the presence of all three inhibitors. This is in contrast to its response to substrate stiffness, where inhibiting AT1 and TGF β receptors had a significant effect (Table 4.2).

Since the model suggested a significant role for AngII signaling in regulating *Fn1* expression in response to increased stiffness but not stretch (Table 2 and Fig. 4.12B), we treated cultured PAAFs with 1 μM losartan, an AT1 receptor blocker.

Losartan abrogated the induction of fibronectin mRNA expression by 3-kPa substrates

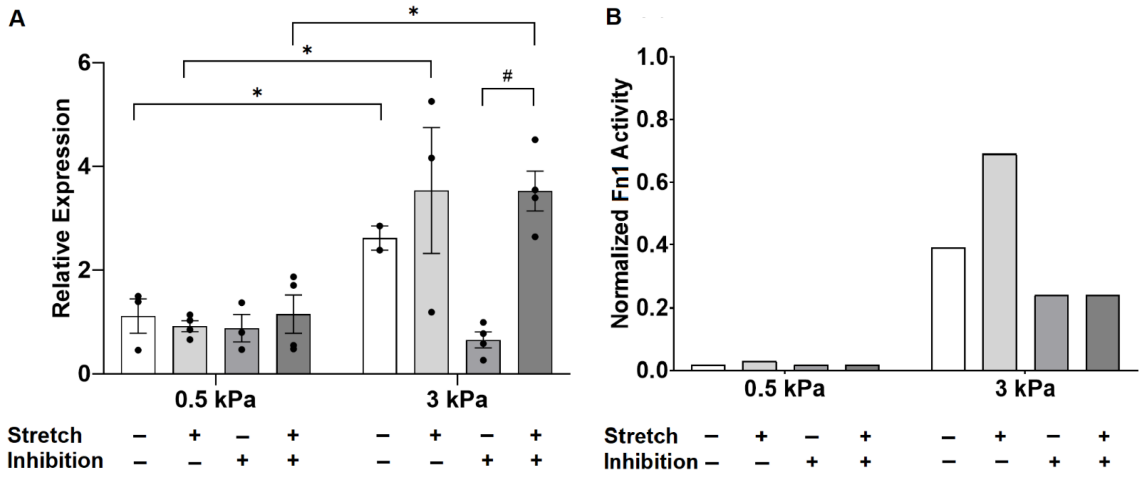

Figure 4.12| Experimental observations of fibronectin gene expression in response to increased substrate stiffness and 10% equibiaxial stretch, with and without AT1R inhibitor losartan PAAFs). (A) Data are expressed as Fn1 gene expression mean ± standard errors relative to 18S ribosomal RNA housekeeping gene. * Significant effect of stiffness ($p < 0.05$), # significant effect of stretch ($p < 0.05$) by three-way analysis of variance (ANOVA) with a post-hoc Sidak's test. (B) Model simulation results where stiffness and stretch stimuli were increased by increasing the stiffness input weight from 0.25 to 0.7, stretch input weight from 0.25 to 0.7, and inhibition applied by blocking the AT1R node.

compared with 0.5-kPa, and *Fn1* expression by PAAFs grown on 0.5-kPa matrices remained unresponsive to stretch after 24 hr (Fig. 4.12A). Stretch significantly upregulated the expression of *Fn1* by PAAFs grown on stiffer 3-kPa substrates when AngII signaling was blocked.

Model simulations of *Fn1* expression in response to increased stiffness, stretch, and AT1 receptor inhibition corresponding to each experimental condition in Figure 7A are shown in Figure

7B. The model recapitulated the increase in fibronectin mRNA under control conditions, when substrate stiffness increased from 0.5-kPa to 3-kPa, and the qualitative response of *Fn1* on 3-kPa matrices to induction by stretch. The model also correctly predicted no effect of losartan on *Fn1* mRNA levels under stretched and unstretched conditions on 0.5-kPa substrates 24 hr after stretch. However, while we observed *in-vitro* that losartan inhibited *Fn1* upregulation by increased stiffness in unstretched but not stretched PAAFs, and that blocking AT1R led to a stretch response of *Fn1* on 3-kPa matrices, the model could not reproduce these observations.

4.4. Discussion

We created a novel network model of cell signaling in pulmonary arterial adventitial fibroblasts that integrates seven signaling modules known to be involved in pulmonary arterial fibrosis. This model was qualitatively consistent with experimentally measured input-output relationships and the results from inhibition experiments all from independent papers not used to formulate the model originally. To determine the specificity of the model to fibroblasts from the pulmonary arterial adventitia, we ran a simulation using only nodes also included in the cardiac fibroblast model developed by Zeigler *et al*. Here the cardiac fibroblast model with 40 reactions significantly underpredicted by almost threefold the PAAF input-output experiments. This indicates the important role played by the 52 added reactions in our fibroblast model to describe the signaling pathway representing PAAF properties in PAH. Sensitivity analysis showed that the model-predicted PAAF network state was most sensitive to TGFβ, MAPK, and hypoxia signaling pathways. The sensitivity analysis for the cardiac fibroblast model showed similar importance of TGFβ pathways and MAPK pathways, but that mechanical stimulus more impact. By using uncertainty quantification, we determined the robustness of the model with respect to input weight

and EC_{50}, but found that parameter uncertainty propagation was increased significantly with increased n.

This paper takes similar approaches to those previously undertaken in other logic-based network models including those done by Zeigler *et al*. [131] and Kraeutler *et al*. [173]. The Zeigler model has been shown to be similarly robust to this PAAF model, with an accuracy of 80% and similarly predicts a strong influence of TGFβ [131]. Our model uses the same default parameters and also includes analysis of variation in baseline input. This is in contrast to the Kraeutler model, where the model is fully parameterized and the authors carried out a sensitivity analysis on the Hill coefficient, EC_{50}, and y_{max} [173]. We have further varied the Hill coefficient and EC_{50} using a uniform distribution using UQ.

We also identified the areas of epistemic uncertainty inherent in network construction that will need further confirmation, revision and comparison with future experiments done specifically in PAAFs by running a three parameter UQ analysis on the model with and without the pathways derived from non-cardiovascular fibroblasts. In some cases, information from non-cardiovascular cell types were shown not to highly affect input-output prediction accuracy but did improve the accuracy of predictions on the effects of inhibitors as seen in the predictions of how α-SMA responds to TGFβ when ERK or ROS were inhibited. Thus, the full model, despite including pathways from other cell types, better recapitulated the regulation of α-SMA expression. In this way, UQ was able to capture the levels to which the output of model accuracy could vary given changes in large ranges of parameters and in the absence of pathways elucidated by non-cardiovascular fibroblasts. This analysis was crucial to a system that has so little certainty in model construction and literature data such as in PAAFs. With directions for optimization given by UQ, this model can be improved to help the scientific community understand the complex interplay of

pathways in pulmonary arterial remodeling in order to identify treatments that can better target adventitial fibrosis.

In-vitro experiments in pulmonary arterial adventitial fibroblasts were used to investigate the differential effects of equibiaxial stretch and increased substrate stiffness on six genes of a revised mathematical model of PAAF cell signaling [379]. While both physical stimuli occur in PAH, these stimuli are thought to be at different stages of the disease, in part because increased vascular fibrosis leads to ECM stiffening that in turn opposes the increase in arterial wall strain caused by increased wall stress. In this study, we used a novel combination of *in-vitro* and *in-silico* models to investigate how PAAFs respond to changes in ECM stiffness and strains representative of those associated with adventitial remodeling in PAH. While PAAFs are exposed to cyclic loading *in vivo*, we used static stretch as a model of the chronically elevated mean hemodynamic load (Herum KM *et al*., 2017) during PAH rather than acute phasic vascular loading, in part because cyclic stretch systems cannot recapitulate the high physiological cardiac frequencies (~6 Hz) in rats (Layland J *et al*., 1995) [321, 387]. Although there are no existing studies examining how PAAFs respond to cyclic stretch, Wu et al. (Wu J *et al*., 2013) reported that 10% cyclic stretch for 36 hr led to 2-3 fold increases in *Col1a1* and *Col3a1* expression in mouse aortic fibroblasts, which are comparable to the 3-fold increase in *Col1a1* and 2- to 4-fold increase in *Col3a1* that we observed after 24 hr of static stretch [340]. While the cells were maintained at a 10% static stretch for 24 hr, measurements of cell area in cardiac fibroblasts using the same circular custom stretchers (Herum KM *et al*., 2017) showed that after cell area initially increased during static stretch, they returned to their original size within 1 hour, well before the 24-hour time point at which gene expression was measured [321].

4.4.1. Stiffness and Stretch Differentially Affect Expression of Six Profibrotic Genes

Stretch and increased substrate stiffness were both able to upregulate five out of the six profibrotic genes we investigated. But while increasing stiffness from 0.5 kPa significantly induced all six genes, fibronectin expression was transiently upregulated by stretch at 4 hr but was not significantly altered by stretch at 24 hr. There was also a non-monotonic response to the two levels of increased substrate stiffness in the expression of *Loxl1* and *Acta2*, which were both upregulated compared with 0.5-kPa substrates on 3-kPa matrices (similar to vessel walls during mild PAH), but the expression of both was not significantly altered compared with 0.5-kPa substrates on 10-kPa matrices (which are comparable in stiffness to vessel walls during severe PAH). Unlike observations in cardiac fibroblasts [321], we found no statistical interaction effects between the stretch and stiffness conditions in all these six genes. These results suggest that the expression of *Col1a1*, *Col3a1* and *Eln* could be expected to rise early *in-vivo* as elevated pulmonary arterial pressure increases vascular wall strain and remain elevated as fibrosis increases adventitial ECM stiffness, even though this stiffening would also reduce arterial strain. In contrast, *Loxl1* and *Acta2* expression may initially rise but eventually return to baseline as wall stiffening becomes severe, and *Fn1* mRNA may be induced only after the ECM has remodeled and stiffened.

4.4.2. Model Modifications to Investigate Differential Regulation by Stretch and Stiffness

By allowing stiffness and stretch to be separate inputs to the model, we investigated the pathways regulating the expression of six mechanosensitive genes (*Col1a1*, *Col3a1*, *Eln*, *Fn1*, *Loxl1*, *Acta2*) in response to each stimulus. While there is published evidence that TGFβ is activated by stretch in cardiac [321] and lung [388] fibroblasts, we only found experimental evidence of TGFβ activation by substrate stiffness in PAAFs [327, 329]. Based on ample

published data in other cell types, we refined the model of the MAPK signaling cascade in the original version of our model so that ERK1/2, p38, and JNK1/2 could be independently activated, and we updated the model to include the effects of stretch-activated TRP channels observed by Yue and Suzuma *et al* [163-164].

Comparing the predictions of this revised model against the same independent experimental data from rat and human PAAFs that we used to test our original implementation [379], we found no significant changes in model validation accuracy from what we reported previously [379]. Comparing predictions of the revised model with *in-vitro* PAAF experiments conducted here on the effects of stretch and stiffness on gene expression, the model correctly predicted the upregulation of all six ECM genes by increased stiffness though not the subsequent return to baseline levels on the stiffest matrices for *Loxl1* and *Acta2*. The model also correctly predicted the observed upregulation of four ECM genes and the lack of response to stretch in *Fn1* expression at 24 hr. However, while we observed an increase in *Eln* mRNA after stretch, the model incorrectly predicted a decrease. Examining the regulation of elastin gene expression in the network, we found that halving the weight of JNK1/2 inhibition on *Eln* mRNA while leaving the activating weight of PKCα on *Eln* the same reversed this result. Hence it is possible that the activating effect of PKCα dominates the inhibiting effect of JNK1/2 in the regulation of elastin gene expression by stretch.

The model is composed of studies from both *in-vivo* and *in-vitro* experiments. While we used the rat PAAFs to validate the gene expression in response to stimuli such as mechanical stretch or substrate stiffness, this approach allows us to predict how phenotypic outputs respond to mechanical load. It is reported that mechanical stretch may increase the stiffness of the substrate, which in turn decreases the stretch. However, the interactions between them have not yet been

classified. Through this work, we can model the interactions by adjusting time parameters and the activated reactions to represent beneficial versus maladaptive remodeling in fibrosis. Furthermore, the model can simulate a high number of experimental designs and make corresponding predictions that would be difficult to reproduce experimentally. This feature also enables the model to predict effects of specific drugs through simulating the activation or inhibition of any target species in the network.

4.4.3. Crosstalk between TGF and AngII

Using this model to predict the effects of inhibiting key mechanoresponsive nodes in the network, we found that blocking AT1R in the model significantly decreased expression of *Fn1* in response to stiffness but did not significantly decrease expression of *Fn1* in response to stretch. Experimentally, we confirmed that blocking the AT1 receptor with losartan inhibited the significant upregulation of *Fn1* expression when substrate stiffness is increased and had no effect on the response to stretch on 0.5-kPa substrates. However, losartan unmasked a response to stretch in PAAFs grown on the stiffer matrices that was not seen in untreated cells or predicted by the model. These findings show that angiotensin II signaling is required for the *Fn1* response to increased stiffness, and that *Fn1* expression can be stretch-regulated by an angiotensin-independent pathway on stiffer matrices when the saturating effects of higher stiffness are blocked. The requirement for angiotensin receptors to be activated before fibronectin mRNA can be induced by elevated substrate stiffness may be related to angiotensin-mediated conversion of latent TGFβ to the active state [389-390]. The network already represents this feedback based on reports that cyclic strain activates AT1R to cause activation of TGF-β in rat cardiac fibroblasts and human fibroblasts [389, 391]. However, because stiffness also directly activates TGFβ in the model,

angiotensin signaling could be blocked in the model without preventing stiffness from inducing *Fn1* expression. This suggests that increased stiffness only activates TGFβ signaling after angiotensin has activated latent TGFβ in our experiments. Angiotensin receptor inhibition also unmasked angiotensin-independent *Fn1* expression in response to stretch at a higher substrate stiffness, but in the model, fibronectin mRNA can only be induced by stretch directly *via* the angiotensin receptor. Hence, our experimental results suggest that there is another stretch-activated pathway that regulates a transient response to stretch in fibronectin and is more active in cells grown on stiffer matrices independent of AngII. This indicates a currently unknown angiotensin-independent stretch-activated pathway responsible for an initial rapid upregulation of fibronectin gene expression, possibly the STAT3 pathway which is involved in stretch induction of fibronectin in renal epithelial cells but not proven in fibroblasts studied by Hamzeh *et al.* [392]. An angiotensin-dependent pathway that downregulates fibronectin expression after 4 hr need to be added to the model. One way to further examine this potential crosstalk would be to treat PAAFs with a TGF-β blocker based on the high magnitude of inhibition predicted by the model simulations (Table 4.2). When blocking TGFβ in the model, expression of *Col1a1*, *Col3a1*, *Eln*, *Fn1*, and *Acta2* were significantly inhibited in response to increased stiffness, with no significant change observed on inhibiting stretch effects except for *Acta2*.

4.4.4. Limitations and Future Directions

There is very little literature from which to determine specific model parameters, so we have not attempted to identify individual parameters and instead used constant values for every node and explored parameter uncertainty over a wide range. For example, all reactions are at a default weight of 1, however literature data could suggest that some reactions are more important

than others in determining fibrosis. These findings are consistent with the conclusion that capturing the molecular interactions within the network topology is more important for reproducing the qualitative features revealed by typical cell biological experiments than the particular choice of parameters. This property explains why this class of network model is often preferred to more biochemically detailed models with fewer interacting pathways for interpreting the frequently more qualitative conclusions of many cell biological studies. The analyses suggested that the model is quite robust to parameter uncertainty, at least when using qualitative experimental criteria. When varying input weight (ω) the model accuracy ranged from 67%-80%, when varying half-maximal effective concentration (EC_{50}) the accuracy generally ranged from 60%-80%, and the model accuracy was highly affected by changes in the Hill coefficient n). Given that the UQ results depend on the ranges chosen for the model parameters, in this case n, EC_{50}, and ω, caution should be taken in making too many biological conclusions based on this analysis.

A critical next step identified by uncertainty quantification is to fill in the areas where there are no *in-vitro* experiments in PAAFs both to refine the model and acquire more validation data so one can be more confident in the results. For example, there is no literature data on how stimulation of PAAFs with TNFα affect phenotypic outputs, only on intermediates in the model. There is some data uncertainty in the literature, as a low sample size and power in typical cell biology experiments means there is less confidence in experimental findings concluding no significant change vs. those reporting significant changes.

The model is currently only shown to be qualitatively consistent with input-output experiments and normalized from 0 to 1 as the range is unknown and many reported experimental results are not quantitative. In the future, we can implement mass-action equations with kinetic rates to create a more quantitative and realistic measure of matrix remodeling that we can validate

through experimentation. We can also integrate paracrine signaling with other cell types, as PAAFs are known to activate macrophages and smooth muscle cells surrounding them in the pulmonary arterial wall [351]. Another future direction is to reformulate the model by adding exogenous stimulation for ET1 and IL6 and feedback, which could increase model accuracy.

In-vitro experiments in pulmonary arterial adventitial fibroblasts were used to investigate the differential effects of equibiaxial stretch and increased substrate stiffness on six genes of a new mathematical model of PAAF cell signaling [379]. While both physical stimuli occur in PAH, these stimuli are thought to be at different stages of the disease, in part because increased vascular fibrosis leads to ECM stiffening that in turn opposes the increase in arterial wall strain caused by increased wall stress. In this study, we used a novel combination of *in-vitro* and *in-silico* models to investigate how PAAFs respond to changes in ECM stiffness and strains representative of those associated with adventitial remodeling in PAH.

We used rat PAAFs because of the detailed biomechanical measurements of ECM stiffness pulmonary arterial strain in the sugen-hypoxia rat model of PAH and normotensive control rats. However, human PAAF cell lines have been used to study fibrotic signaling in response to increased ECM stiffness [351], where they showed that ten out of twelve genes studied were differentially expressed when stiffness increased from 1 to 12 kPa. Their analysis identified a miR-130/301-PPARγ signaling network regulated by ECM stiffness and associated with ECM remodeling in human PAH. Studies of mechanosignaling in human PAAF cell lines would enable us to generate a similar model of profibrotic mechanosignaling in human cells that could include these networks. ECM remodeling depends on protein synthesis, post-translational modifications and cell-mediated matrix assembly [107]. One limitation of this study is that we focused primarily on gene expression, but we did find that changes in collagen III and smooth muscle actin protein

abundances in response to increased ECM stiffness were consistent with changes in their mRNA expression. Finally, while the model was able to predict the response of fibronectin gene expression on soft gels, it did not replicate all of the observed responses to AT1 receptor inhibition on stiff gels or the transient response of *Fn1* expression to stretch. These model limitations can nevertheless be used to identify candidate pathways and reactions that need to be added to the network.

4.5. Conclusion

In-vitro experiments using hydrogel substrates of various stiffnesses coating elastic membranes in biaxial cell stretch devices showed that expression of profibrotic genes by PAAFs is differentially regulated by cell stretch and extracellular matrix stiffness. No interaction effects between stretch and stiffness were observed for the six genes studied here, however AT1 receptor blockade uncovered an angiotensin-independent activation of *Fn1* expression by stretch in PAAFs when grown on stiff but not soft substrates. A novel combination of *in-vitro* and *in-silico* models of PAAF profibrotic cell signaling in response to altered mechanical conditions may help identify regulators of the vascular adventitial remodeling that results from the changes in stretch and matrix stiffness occurring during the progression of PAH *in-vivo*.

4.6. Acknowledgements

Chapter 4, in full, is a reprint of the materials as it appears in the following publications: Philosophical Transactions of the Royal Society A 2020. Wang, Ariel; Cao, Shulin; Aboelkassam Yasser; Valdez-Jasso Daniela, Cells 2021. Wang, Ariel; Cao, Shulin; Stowe Jennifer C.; Valdez-Jasso Daniela. The dissertation author was the second author of these papers and developed all methodology and computational analysis.

Chapter 5: Summary and Conclusion

5.1. Summary of Objectives and Conclusions

The objective of this dissertation was to unveil the mechanisms underlying the differential responses of different experiments and explore potential therapies of heart failure in the future. In Chapter 2, a global UQ analysis was performed to illustrate the model robustness to the changes in parameters, network modules and validation data. In Chapter 3, a computational model of gene expression responses to mechanical stretch was constructed by extending a published mechanosignaling network with transcriptional regulatory network and used to identify key regulators of the stretch induced responses and the pathways and genes that responded differently to transverse stretch and longitudinal stretch. In Chapter 4, a new PAAF model was constructed using the same methodology to showcase the effectiveness of the model and identify the differential responses of pro-fibrotic genes induced by substrate stiffness and stretch.

Quantification analysis of the effects of the uncertainty in model parameters, logic, and validation data on the estimated accuracy of the mechanosignaling network model showed that the model was very robust to parameter and data uncertainty but was more vulnerable to errors in the choice of logic used to represent the biochemical reactions between interacting species. Our analysis indicates that the correct interpretation of experimental data representing the 'AND' and 'OR' logic could be critical to model prediction accuracy.

We further developed a novel extension of our myocyte mechanosignaling network model to include both transcriptional and translational regulation and introduce a mass-action method to model quantitative gene expression. The KEGG enrichment analysis of the RNA-Seq measurements showed many pathways used to formulate the model were also enriched. By

incorporating the RNA-Seq data, this new model displayed high accuracy with 69% agreement for overall predictions and 72% of predicted DE genes under 4 hr longitudinal stretch. It is also indicated from model simulations that TF activities may saturate faster when multiple TFs coregulate gene expression. Our analysis also suggests that the difference between transverse and longitudinal stretch responses in cardiomyocytes may be related to the sensitivity of directional mechanotransduction, with the sensitivity to longitudinal stretch being greater than transverse. We further identified AT1 and ET1 as main regulators in response to stretch through receptor inhibition simulations and the subsequent experiments. This analysis also showed the importance of a hypertrophy pathway that regulate target genes via the activation of AT1/ET1 receptors through the MAPK signaling pathway.

To showcase the performance of this methodology, we applied this approach to build a PAAF signaling model and achieved 80% agreement with published studies that were not used to build the model. The UQ analysis indicated that the model accuracy was very robust to the parameter changes as well as epistemic uncertainty while reducing the network to reactions only reported in PAAFs had a larger impact. This model also demonstrated that the differential responses of profibrotic genes induced by substrate stiffness and stretch were mainly in Fn1 expression, which could be activated *via* an angiotensin-independent pathway.

5.2. Future Work

5.2.1. Modifications and Improvements of the Mechanosignaling Network

The RNA-seq measurements showed 495 genes were DE under stretch but their regulations were not clearly identified when the mechanosignaling network model was constructed. By using a published database of TF-gene regulation, we found that a new set 17 genes were regulated by 9

TFs in the model. By incorporating these genes in a revised network, our model correctly predicted the responses of these genes, which may indicate the potential roles of these genes in the hypertrophy. Further, an enrichment of these 495 genes showed 4 genes were targets of SREBP, a TF associated with lipid metabolism targeted by AngII signaling pathway during the cardiac hypertrophy [393-394]. This approach provides a methodology of identifying new TFs to the mechanosignaling network model.

For model genes, our current model incorrectly predicted the direction of 67 genes, with 39 predicted upregulated in the model while NC in the data and 28 predicted NC in the model but downregulated in the data. By looking into the TF-gene regulation database [395], we found 7 genes were repressed by 16 TFs, which was not present in the current model. Among these TFs, we found Smad4 associated with cardiac hypertrophy [394-395]. TGFβ-Smad4 was found to be elevated by AngII-MAPK signaling while the deletion of Smad4 resulted in hypertrophy in cardiomyocytes [396-397]. These results suggests that the model could be improved by including more detailed regulations especially negative regulators.

Pathway enrichment analysis of the RNA-Seq data suggested more pathways could be involved in the current model. Early studies showed the critical role of the Hippo signaling pathway in cardiomyocyte hypertrophy [155-156, 313-314] induced by exercise training rather than pathological hypertrophy. The inactive Hippo signaling enhances gene by interacting with proteins such as SMAD [156, 313]. Hippo signaling has also been shown to be an important regulator of many miRNAs, which often act as negative regulators of transcriptional responses [313-314]. It is also documented that Akt and MAPKs could also interact with Hippo signaling while the effects of these interactions were not clear [156, 313].

Oxytocin (OT) and its receptor OTR are expressed in heart and also important players involved in cardioprotection [398-399]. The treatment of cardiomyocyte with OT can promote the accumulation of ANP and increase intracellular cGMP by reducing the Akt phosphorylation thus blocking the translocation of NFAT into the cell nuclei [399].

The Ras related GTPase (Rap), a memeber of the Ras superfamily, mostly acts as the transformation suppressor to ameliorate the Ras transformed phenotype. The Rap1 signaling pathway, which is activated by cyclic AMP (cAMP), calcium and DAG, promotes vasoconstriction by the activation of JNK, ERK and Rho/ROCK signaling and further increase cell adhesion [315].

The ErbB protein is a receptor tyrosine kinase that transduces the signal from extracellular environment to the nucleus and promotes differentiation. The over-expression of ErbB will upregulate the Heat Shock Factor (HSF)-1 transcription factor and its target genes [400]. ErbB receptors activate the mitogen-activated protein kinase (MAPK)/ERK1/2 as well as PI3K/Akt signaling. It is also reported that ErbB is downregulated during the progression of cardiac hypertrophy [400-401], however, the mechanism is not clear yet.

Hypoxia Inducible Factor (HIF)-1 is a transcription factor that regulates oxygen homeostasis thus critical to maintain normal cardiac function. By its name, HIF-1 signaling pathway has been shown to be associated with reduction of the generation of reactive oxygen species (ROS) and hypoxia induced hypertrophy.

By including these new pathways in the current model, we aim to explore more genes in the stretch induced hypertrophy genetic program and identify the key regulators underlying in the differential responses for the experiment of interest.

5.2.2. Pressure and Volume Overload Induced Hypertrophy

In structural heart diseases, increased ventricular load is a key trigger mechanism for altered gene expression and cardiac remodeling. Increased ventricular load translates into increased wall stress and results in the growth of the individual cardiomyocyte, leading to increased heart weight. Studies showed that the total myocyte number remains unchanged following the TAC but its proportion in the cell population dropped due to a profound increase of fibroblasts [402]. These changes then increased the stiffness of the tissue. Both systolic and diastolic blood pressure were found to be increased 2 weeks after TAC and remained elevated [403-406]. The left ventricle peak systolic wall stress was found elevated as quickly as 1 day after TAC and restored at around 10 days [407]. Compared with pressure overload that induced concentric hypertrophy, volume overload induced eccentric hypertrophy increased both the thickness of heart wall and the volume of the ventricle. The mechanisms that led to the two types of hypertrophies, however, require further understanding.

While many studies have shown the roles of individual signaling pathways in cardiac hypertrophy, how these signaling pathways integrates in regulating the transcriptional and translational responses are poorly understood. It is reported that different pathways were activated during these two processes. CaMK and ERK signaling were found activated in pressure overload induced hypertrophy while Akt signaling was elevated in volume overload induced hypertrophy [408]. On the transcription level, it is shown that cyclin D2 expression attenuated cardiomyocyte hypertrophy in pressure overload but not volume overload [409]. Thus, realizing this difference, we will use the mechanosignaling network model to study the differential regulation patterns that led to the difference of hypertrophy induced by pressure overload and volume overload. By

referring to the network, we will use mechanical stress to initialize the network and identify key regulators in response to hypertrophy.

5.3. Significance

The global UQ analysis provides us an objective approach in demonstrating the model robustness as well as the correct choice of model parameters. The independent enrichment analysis of KEGG pathways from DE genes and model genes validated the effectiveness of pathway integration during model construction. By analyzing the RNA-Seq data of stretch, we showed the numerical relationship of transverse stretch and longitudinal stretch induced gene expressions. In our work, this is the first time that we were able to model gene expression quantitatively, which also confirmed our finding of the numerical difference between transverse stretch and longitudinal stretch on regulating gene expression. Besides, the analysis of the MSN regulatory model also helped identify the key regulators of the mechanical stretch induced genetic responses. The further application of this methodology in another tissue (PAAF) has also shown effectiveness and implied the potential ability of the MSN model to be integrated into the organ level. Finally, the receptor inhibition analysis also suggested the efficacy of model to test and develop new drugs. To summarize, the integration of the RNA-Seq data and the mass action method allows the quantitative comparison between experimental measurements and model predictions, which can help understand the mechanisms behind the differential responses of different experiments and explore potential therapies of heart failure in the future.

References

[1] Braunwald E. Heart disease.

[2] Mihl C, Dassen WR, Kuipers H. Cardiac remodelling: concentric versus eccentric hypertrophy in strength and endurance athletes. Netherlands Heart Journal. 2008 Apr;16(4):129-33.

[3] Samak M, Fatullayev J, Sabashnikov A, Zeriouh M, Schmack B, Farag M, Popov AF, Dohmen PM, Choi YH, Wahlers T, Weymann A. Cardiac hypertrophy: an introduction to molecular and cellular basis. Medical science monitor basic research. 2016;22:75.

[4] Azevedo PS, Polegato BF, Minicucci MF, Paiva SA, Zornoff LA. Cardiac remodeling: concepts, clinical impact, pathophysiological mechanisms and pharmacologic treatment. Arquivos brasileiros de cardiologia. 2015 Dec 8;106:62-9.

[5] Heineke J, Molkentin JD. Regulation of cardiac hypertrophy by intracellular signalling pathways. Nature reviews Molecular cell biology. 2006 Aug;7(8):589-600.

[6] Estrada AC, Yoshida K, Saucerman JJ, Holmes JW. A multiscale model of cardiac concentric hypertrophy incorporating both mechanical and hormonal drivers of growth. Biomechanics and Modeling in Mechanobiology. 2021 Feb;20(1):293-307.

[7] Majkut S, Dingal PD, Discher DE. Stress sensitivity and mechanotransduction during heart development. Current Biology. 2014 May 19;24(10):R495-501.

[8] Jaalouk DE, Lammerding J. Mechanotransduction gone awry. Nature reviews Molecular cell biology. 2009 Jan;10(1):63-73.

[9] Swynghedauw B. Darwinian evolution and cardiovascular remodeling. Heart failure reviews. 2016 Nov;21(6):795-802.

[10] Sugden PH. Mechanotransduction in cardiomyocyte hypertrophy.

[11] Lyon RC, Zanella F, Omens JH, Sheikh F. Mechanotransduction in cardiac hypertrophy and failure. Circulation research. 2015 Apr 10;116(8):1462-76.

[12] Derderian CA, Bastidas N, Lerman OZ, Bhatt KA, Lin SE, Voss J, Holmes JW, Levine JP, Gurtner GC. Mechanical strain alters gene expression in an in vitro model of hypertrophic scarring. Annals of plastic surgery. 2005 Jul 1;55(1):69-75.

[13] Ali H, Braga L, Giacca M. Cardiac regeneration and remodelling of the cardiomyocyte cytoarchitecture. The FEBS journal. 2020 Feb;287(3):417-38.

[14] Sequeira V, Nijenkamp LL, Regan JA, van der Velden J. The physiological role of cardiac cytoskeleton and its alterations in heart failure. Biochimica et Biophysica Acta (BBA)-Biomembranes. 2014 Feb 1;1838(2):700-22.

[15] Harston RK, Kuppuswamy D. Integrins are the necessary links to hypertrophic growth in cardiomyocytes. Journal of signal transduction. 2011;2011.

[16] Sadoshima JI, Xu Y, Slayter HS, Izumo S. Autocrine release of angiotensin II mediates stretch-induced hypertrophy of cardiac myocytes in vitro. Cell. 1993 Dec 3;75(5):977-84.

[17] Kagami S, Border WA, Miller DE, Noble NA. Angiotensin II stimulates extracellular matrix protein synthesis through induction of transforming growth factor-beta expression in rat glomerular mesangial cells. The Journal of clinical investigation. 1994 Jun 1;93(6):2431-7.

[18] Reed A, Kohl P, Peyronnet R. Molecular candidates for cardiac stretch-activated ion channels. Global Cardiology Science and Practice. 2014 Aug 1;2014(2):19.

[19] Komuro I, Kudo S, Yamazaki T, Zou Y, Shiojima I, Yazaki Y. Mechanical stretch activates the stress-activated protein kinase in cardiac myocytes. The FASEB Journal. 1996 Apr;10(5):631-6.

[20] Sadoshima JI, Izumo S. Mechanical stretch rapidly activates multiple signal transduction pathways in cardiac myocytes: potential involvement of an autocrine/paracrine mechanism. The EMBO journal. 1993 Apr;12(4):1681-92.

[21] Covella M, Rowin EJ, Hill NS, Preston IR, Milan A, Opotowsky AR, Maron BJ, Maron MS, Maron BA. Mechanism of progressive heart failure and significance of pulmonary hypertension in obstructive hypertrophic cardiomyopathy. Circulation: Heart Failure. 2017 Apr;10(4):e003689.

[22] Mitra A, Ghosh RK, Bandyopadhyay D, Ghosh GC, Kalra A, Lavie CJ. Significance of pulmonary hypertension in hypertrophic cardiomyopathy. Current problems in cardiology. 2020 Jun 1;45(6):100398.

[23] Tuder RM. Pulmonary vascular remodeling in pulmonary hypertension. Cell and tissue research. 2017 Mar;367(3):643-9.

[24] Martin KB, Klinger JR, Rounds SI. Pulmonary arterial hypertension: new insights and new hope. Respirology. 2006 Jan;11(1):6-17.

[25] Stenmark KR, Nozik-Grayck E, Gerasimovskaya E, Anwar A, Li M, Riddle S, Frid M. The adventitia: essential role in pulmonary vascular remodeling. Comprehensive Physiology. 2011 Jan;1(1):141.

[26] Davie NJ, Gerasimovskaya EV, Hofmeister SE, Richman AP, Jones PL, Reeves JT, Stenmark KR. Pulmonary artery adventitial fibroblasts cooperate with vasa vasorum endothelial cells to regulate vasa vasorum neovascularization: a process mediated by

hypoxia and endothelin-1. The American journal of pathology. 2006 Jun 1;168(6):1793-807.

[27] Ervasti JM, Campbell KP. A role for the dystrophin-glycoprotein complex as a transmembrane linker between laminin and actin. Journal of Cell Biology. 1993 Aug 15;122(4):809-23.

[28] Li S, Qi Y, McKee K, Liu J, Hsu J, Yurchenco PD. Integrin and dystroglycan compensate each other to mediate laminin-dependent basement membrane assembly and epiblast polarization. Matrix Biology. 2017 Jan 1;57:272-84.

[29] Ogawa E, Saito Y, Harada M, Kamitani S, Kuwahara K, Miyamoto Y, Ishikawa M, Hamanaka I, Kajiyama N, Takahashi N, Nakagawa O. Outside-in signalling of fibronectin stimulates cardiomyocyte hypertrophy in cultured neonatal rat ventricular myocytes. Journal of molecular and cellular cardiology. 2000 May 1;32(5):765-76.

[30] Terracio L, Rubin K, Gullberg D, Balog E, Carver W, Jyring R, Borg TK. Expression of collagen binding integrins during cardiac development and hypertrophy. Circulation research. 1991 Mar;68(3):734-44.

[31] Sadoshima JI, Izumo S. Molecular characterization of angiotensin II--induced hypertrophy of cardiac myocytes and hyperplasia of cardiac fibroblasts. Critical role of the AT1 receptor subtype. Circulation research. 1993 Sep;73(3):413-23.

[32] Shubeita HE, McDonough PM, Harris AN, Knowlton KU, Glembotski CC, Brown JH, Chien KR. Endothelin induction of inositol phospholipid hydrolysis, sarcomere assembly, and cardiac gene expression in ventricular myocytes. A paracrine mechanism for myocardial cell hypertrophy. Journal of Biological Chemistry. 1990 Nov 25;265(33):20555-62.

[33] Zou Y, Akazawa H, Qin Y, Sano M, Takano H, Minamino T, Makita N, Iwanaga K, Zhu W, Kudoh S, Toko H. Mechanical stress activates angiotensin II type 1 receptor without the involvement of angiotensin II. Nature cell biology. 2004 Jun;6(6):499-506.

[34] Hirota H, Chen J, Betz UA, Rajewsky K, Gu Y, Ross Jr J, Müller W, Chien KR. Loss of a gp130 cardiac muscle cell survival pathway is a critical event in the onset of heart failure during biomechanical stress. Cell. 1999 Apr 16;97(2):189-98.

[35] Uozumi H, Hiroi Y, Zou Y, Takimoto E, Toko H, Niu P, Shimoyama M, Yazaki Y, Nagai R, Komuro I. gp130 plays a critical role in pressure overload-induced cardiac hypertrophy. Journal of Biological Chemistry. 2001 Jun 22;276(25):23115-9.

[36] Fischer P, Hilfiker-Kleiner D. Role of gp130-mediated signalling pathways in the heart and its impact on potential therapeutic aspects. British journal of pharmacology. 2008 Mar;153(S1):S414-27.

[37] Nakamura K, Kamouchi M, Kitazono T, Kuroda J, Matsuo R, Hagiwara N, Ishikawa E, Ooboshi H, Ibayashi S, Iida M. Role of NHE1 in calcium signaling and cell proliferation

in human CNS pericytes. American Journal of Physiology-Heart and Circulatory Physiology. 2008 Apr;294(4):H1700-7.

[38] Stromer MH. The cytoskeleton in skeletal, cardiac and smooth muscle cells.

[39] Ehler E, Perriard JC. Cardiomyocyte cytoskeleton and myofibrillogenesis in healthy and diseased heart. Heart failure reviews. 2000 Oct;5(3):259-69.

[40] Peter AK, Cheng H, Ross RS, Knowlton KU, Chen J. The costamere bridges sarcomeres to the sarcolemma in striated muscle. Progress in pediatric cardiology. 2011 May 1;31(2):83-8.

[41] Spudich JA. The myosin swinging cross-bridge model. Nature reviews Molecular cell biology. 2001 May;2(5):387-92.

[42] Frank D, Frey N. Cardiac Z-disc signaling network. Journal of Biological Chemistry. 2011 Mar 25;286(12):9897-904.

[43] Granzier HL, Labeit S. The giant protein titin: a major player in myocardial mechanics, signaling, and disease. Circulation research. 2004 Feb 20;94(3):284-95.

[44] Anderson BR, Granzier HL. Titin-based tension in the cardiac sarcomere: molecular origin and physiological adaptations. Progress in biophysics and molecular biology. 2012 Oct 1;110(2-3):204-17.

[45] Bogomolovas J, Gasch A, Simkovic F, Rigden DJ, Labeit S, Mayans O. Titin kinase is an inactive pseudokinase scaffold that supports MuRF1 recruitment to the sarcomeric M-line. Open biology. 2014 May 1;4(5):140041.

[46] Hoshijima M. Mechanical stress-strain sensors embedded in cardiac cytoskeleton: Z disk, titin, and associated structures. American Journal of Physiology-Heart and Circulatory Physiology. 2006 Apr;290(4):H1313-25.

[47] Knöll R, Hoshijima M, Hoffman HM, Person V, Lorenzen-Schmidt I, Bang ML, Hayashi T, Shiga N, Yasukawa H, Schaper W, McKenna W. The cardiac mechanical stretch sensor machinery involves a Z disc complex that is defective in a subset of human dilated cardiomyopathy. Cell. 2002 Dec 27;111(7):943-55.

[48] Manso AM, Li R, Monkley SJ, Cruz NM, Ong S, Lao DH, Koshman YE, Gu Y, Peterson KL, Chen J, Abel ED. Talin1 has unique expression versus talin 2 in the heart and modifies the hypertrophic response to pressure overload. Journal of Biological Chemistry. 2013 Feb 1;288(6):4252-64.

[49] Gingras AR, Bate N, Goult BT, Patel B, Kopp PM, Emsley J, Barsukov IL, Roberts GK, Critchley DR. Central Region of Talin Has a Unique Fold That Binds Vinculin and Actin [S]. Journal of Biological Chemistry. 2010 Sep 1;285(38):29577-87.

[50] Kostin S, Scholz D, Shimada T, Maeno Y, Mollnau H, Hein S, Schaper J. The internal and external protein scaffold of the T-tubular system in cardiomyocytes. Cell and tissue research. 1998 Nov;294(3):449-60.

[51] Israeli-Rosenberg S, Manso AM, Okada H, Ross RS. Integrins and integrin-associated proteins in the cardiac myocyte. Circulation research. 2014 Jan 31;114(3):572-86.

[52] Guilluy C, Swaminathan V, Garcia-Mata R, O'Brien ET, Superfine R, Burridge K. The Rho GEFs LARG and GEF-H1 regulate the mechanical response to force on integrins. Nature cell biology. 2011 Jun;13(6):722-7.

[53] Hart MJ, Jiang X, Kozasa T, Roscoe W, Singer WD, Gilman AG, Sternweis PC, Bollag G. Direct stimulation of the guanine nucleotide exchange activity of p115 RhoGEF by Gα13. Science. 1998 Jun 26;280(5372):2112-4.

[54] Peters SL, Michel MC. The RhoA/Rho kinase pathway in the myocardium.

[55] Pham CG, Harpf AE, Keller RS, Vu HT, Shai SY, Loftus JC, Ross RS. Striated muscle-specific β1D-integrin and FAK are involved in cardiac myocyte hypertrophic response pathway. American Journal of Physiology-Heart and Circulatory Physiology. 2000 Dec 1;279(6):H2916-26.

[56] Zhang SJ, Truskey GA, Kraus WE. Effect of cyclic stretch on β1D-integrin expression and activation of FAK and RhoA. American Journal of Physiology-Cell Physiology. 2007 Jun;292(6):C2057-69.

[57] Torsoni AS, Fonseca PM, Crosara-Alberto DP, Franchini KG. Early activation of p160ROCK by pressure overload in rat heart. American Journal of Physiology-Cell Physiology. 2003 Jun 1;284(6):C1411-9.

[58] Morita T, Mayanagi T, Sobue K. Reorganization of the actin cytoskeleton via transcriptional regulation of cytoskeletal/focal adhesion genes by myocardin-related transcription factors (MRTFs/MAL/MKLs). Experimental cell research. 2007 Oct 1;313(16):3432-45.

[59] Kuppuswamy D, Kerr C, Narishige T, Kasi VS, Menick DR, Cooper G. Association of tyrosine-phosphorylated c-Src with the cytoskeleton of hypertrophying myocardium. Journal of Biological Chemistry. 1997 Feb 14;272(7):4500-8.

[60] Hall JE, Schaller MD. Phospholipid binding to the FAK catalytic domain impacts function. PloS one. 2017 Feb 21;12(2):e0172136.

[61] Oudit GY, Sun H, Kerfant BG, Crackower MA, Penninger JM, Backx PH. The role of phosphoinositide-3 kinase and PTEN in cardiovascular physiology and disease. Journal of molecular and cellular cardiology. 2004 Aug 1;37(2):449-71.

[62] Cantley LC. The phosphoinositide 3-kinase pathway. Science. 2002 May 31;296(5573):1655-7.

[63] Franchini KG, Torsoni AS, Soares PH, Saad MJ. Early activation of the multicomponent signaling complex associated with focal adhesion kinase induced by pressure overload in the rat heart. Circulation research. 2000 Sep 29;87(7):558-65.

[64] Wollert KC, Fiedler B, Gambaryan S, Smolenski A, Heineke J, Butt E, Trautwein C, Lohmann SM, Drexler H. Gene transfer of cGMP-dependent protein kinase I enhances the antihypertrophic effects of nitric oxide in cardiomyocytes. Hypertension. 2002 Jan 1;39(1):87-92.

[65] Dimmeler S, Fleming I, Fisslthaler B, Hermann C, Busse R, Zeiher AM. Activation of nitric oxide synthase in endothelial cells by Akt-dependent phosphorylation. Nature. 1999 Jun;399(6736):601-5.

[66] Schlossmann J, Ammendola A, Ashman K, Zong X, Huber A, Neubauer G, Wang GX, Allescher HD, Korth M, Wilm M, Hofmann F. Regulation of intracellular calcium by a signalling complex of IRAG, IP 3 receptor and cGMP kinase Iβ. Nature. 2000 Mar;404(6774):197-201.

[67] Inoue R, Shi J, Jian Z, Imai Y. Regulation of cardiovascular TRP channel functions along the NO–cGMP–PKG axis. Expert review of clinical pharmacology. 2010 May 1;3(3):347-60.

[68] Hoxhaj G, Manning BD. The PI3K–AKT network at the interface of oncogenic signalling and cancer metabolism. Nature Reviews Cancer. 2020 Feb;20(2):74-88.

[69] Walsh K. Akt signaling and growth of the heart.

[70] Proud CG. Ras, PI3-kinase and mTOR signaling in cardiac hypertrophy. Cardiovascular research. 2004 Aug 15;63(3):403-13.

[71] Ozes ON, Mayo LD, Gustin JA, Pfeffer SR, Pfeffer LM, Donner DB. NF-κB activation by tumour necrosis factor requires the Akt serine–threonine kinase. Nature. 1999 Sep;401(6748):82-5.

[72] Mercurio F, Murray BW, Shevchenko A, Bennett BL, Young DB, Li JW, Pascual G, Motiwala A, Zhu H, Mann M, Manning AM. IκB kinase (IKK)-associated protein 1, a common component of the heterogeneous IKK complex. Molecular and cellular biology. 1999 Feb 1;19(2):1526-38.

[73] Beals CR, Sheridan CM, Turck CW, Gardner P, Crabtree GR. Nuclear export of NF-ATc enhanced by glycogen synthase kinase-3. Science. 1997 Mar 28;275(5308):1930-3.

[74] Kerkela R, Kockeritz L, MacAulay K, Zhou J, Doble BW, Beahm C, Greytak S, Woulfe K, Trivedi CM, Woodgett JR, Epstein JA. Deletion of GSK-3β in mice leads to hypertrophic cardiomyopathy secondary to cardiomyoblast hyperproliferation. The Journal of clinical investigation. 2008 Nov 3;118(11):3609-18.

[75] El Jamali A, Freund C, Rechner C, Scheidereit C, Dietz R, Bergmann MW. Reoxygenation after severe hypoxia induces cardiomyocyte hypertrophy in vitro: activation of CREB downstream of GSK3beta. FASEB JOURNAL. 2004 Jul 1;18:1096-8.

[76] Nojima H, Tokunaga C, Eguchi S, Oshiro N, Hidayat S, Yoshino KI, Hara K, Tanaka N, Avruch J, Yonezawa K. The mammalian target of rapamycin (mTOR) partner, raptor, binds the mTOR substrates p70 S6 kinase and 4E-BP1 through their TOR signaling (TOS) motif. Journal of Biological Chemistry. 2003 May 2;278(18):15461-4.

[77] Rommel C, Bodine SC, Clarke BA, Rossman R, Nunez L, Stitt TN, Yancopoulos GD, Glass DJ. Mediation of IGF-1-induced skeletal myotube hypertrophy by PI (3) K/Akt/mTOR and PI (3) K/Akt/GSK3 pathways. Nature cell biology. 2001 Nov;3(11):1009-13.

[78] Hilfiker-Kleiner D, Shukla P, Klein G, Schaefer A, Stapel B, Hoch M, Müller W, Scherr M, Theilmeier G, Ernst M, Hilfiker A. Continuous glycoprotein-130–mediated signal transducer and activator of transcription-3 activation promotes inflammation, left ventricular rupture, and adverse outcome in subacute myocardial infarction. Circulation. 2010 Jul 13;122(2):145-55.

[79] Molkentin JD, Dorn II GW. Cytoplasmic signaling pathways that regulate cardiac hypertrophy. Annual review of physiology. 2001 Mar;63(1):391-426.

[80] Kunisada K, Hirota H, Fujio Y, Matsui H, Tani Y, Yamauchi-Takihara K, Kishimoto T. Activation of JAK-STAT and MAP kinases by leukemia inhibitory factor through gp130 in cardiac myocytes. Circulation. 1996 Nov 15;94(10):2626-32.

[81] Marrero MB, Schieffer B, Paxton WG, Heerdt L, Berk BC, Delafontaine P, Bernstein KE. Direct stimulation of Jak/STAT pathway by the angiotensin II AT 1 receptor. Nature. 1995 May;375(6528):247-50.

[82] Shah BH, Catt KJ. A central role of EGF receptor transactivation in angiotensin II-induced cardiac hypertrophy. Trends in pharmacological sciences. 2003 May 1;24(5):239-44.

[83] Tanaka Y, Tamura K, Koide Y, Sakai M, Tsurumi Y, Noda Y, Umemura M, Ishigami T, Uchino K, Kimura K, Horiuchi M. The novel angiotensin II type 1 receptor (AT1R)-associated protein ATRAP downregulates AT1R and ameliorates cardiomyocyte hypertrophy. FEBS letters. 2005 Mar 14;579(7):1579-86.

[84] Ruwhof C, van der Laarse A. Mechanical stress-induced cardiac hypertrophy: mechanisms and signal transduction pathways. Cardiovascular research. 2000 Jul 1;47(1):23-37.

[85] Sadoshima J, Izumo S. The cellular and molecular response of cardiac myocytes to mechanical stress. Annual review of physiology. 1997 Mar;59(1):551-71.

[86] Zhong L, Chiusa M, Cadar AG, Lin A, Samaras S, Davidson JM, Lim CC. Targeted inhibition of ANKRD1 disrupts sarcomeric ERK-GATA4 signal transduction and

abrogates phenylephrine-induced cardiomyocyte hypertrophy. Cardiovascular research. 2015 May 1;106(2):261-71.

[87] Haizlip KM, Bupha-Intr T, Biesiadecki BJ, Janssen PM. Effects of increased preload on the force-frequency response and contractile kinetics in early stages of cardiac muscle hypertrophy. American Journal of Physiology-Heart and Circulatory Physiology. 2012 Jun 15;302(12):H2509-17.

[88] Ruwhof C, Van Wamel JE, Noordzij LA, Aydin S, Harper JC, Van Der Laarse A. Mechanical stress stimulates phospholipase C activity and intracellular calcium ion levels in neonatal rat cardiomyocytes. Cell calcium. 2001 Feb 1;29(2):73-83.

[89] Sigurdson W, Ruknudin A, Sachs F. Calcium imaging of mechanically induced fluxes in tissue-cultured chick heart: role of stretch-activated ion channels. American Journal of Physiology-Heart and Circulatory Physiology. 1992 Apr 1;262(4):H1110-5.

[90] Gao H, Wang F, Wang W, Makarewich CA, Zhang H, Kubo H, Berretta RM, Barr LA, Molkentin JD, Houser SR. Ca2+ influx through L-type Ca2+ channels and transient receptor potential channels activates pathological hypertrophy signaling. Journal of molecular and cellular cardiology. 2012 Nov 1;53(5):657-67.

[91] Qi Y, Li Z, Kong CW, Tang NL, Huang Y, Li RA, Yao X. Uniaxial cyclic stretch stimulates TRPV4 to induce realignment of human embryonic stem cell-derived cardiomyocytes. Journal of molecular and cellular cardiology. 2015 Oct 1;87:65-73.

[92] Lyford GL, Strege PR, Shepard A, Ou Y, Ermilov L, Miller SM, Gibbons SJ, Rae JL, Szurszewski JH, Farrugia G. α1C (CaV1. 2) L-type calcium channel mediates mechanosensitive calcium regulation. American Journal of Physiology-Cell Physiology. 2002 Sep 1;283(3):C1001-8.

[93] Spassova MA, Hewavitharana T, Xu W, Soboloff J, Gill DL. A common mechanism underlies stretch activation and receptor activation of TRPC6 channels. Proceedings of the National Academy of Sciences. 2006 Oct 31;103(44):16586-91.

[94] Loukin S, Zhou X, Su Z, Saimi Y, Kung C. Wild-type and brachyolmia-causing mutant TRPV4 channels respond directly to stretch force. Journal of Biological Chemistry. 2010 Aug 27;285(35):27176-81.

[95] Von Lewinski D, Stumme B, Maier LS, Luers C, Bers DM, Pieske B. Stretch-dependent slow force response in isolated rabbit myocardium is Na+ dependent. Cardiovascular research. 2003 Mar 15;57(4):1052-61.

[96] Von Lewinski D, Stumme B, Fialka F, Luers C, Pieske B. Functional relevance of the stretch-dependent slow force response in failing human myocardium. Circulation research. 2004 May 28;94(10):1392-8.

[97] Oancea E, Meyer T. Protein kinase C as a molecular machine for decoding calcium and diacylglycerol signals. Cell. 1998 Oct 30;95(3):307-18.

[98] Klee CB, Ren H, Wang X. Regulation of the calmodulin-stimulated protein phosphatase, calcineurin. Journal of Biological Chemistry. 1998 May 29;273(22):13367-70.

[99] Chin D, Means AR. Calmodulin: a prototypical calcium sensor. Trends in cell biology. 2000 Aug 1;10(8):322-8.

[100] Xuan YT, Guo Y, Zhu Y, Wang OL, Rokosh G, Messing RO, Bolli R. Role of the protein kinase C-ε–Raf-1–MEK-1/2–p44/42 MAPK signaling cascade in the activation of signal transducers and activators of transcription 1 and 3 and induction of cyclooxygenase-2 after ischemic preconditioning. Circulation. 2005 Sep 27;112(13):1971-8.

[101] Coles LC, Shaw PE. PAK1 primes MEK1 for phosphorylation by Raf-1 kinase during cross-cascade activation of the ERK pathway. Oncogene. 2002 Mar;21(14):2236-44.

[102] Vega RB, Harrison BC, Meadows E, Roberts CR, Papst PJ, Olson EN, McKinsey TA. Protein kinases C and D mediate agonist-dependent cardiac hypertrophy through nuclear export of histone deacetylase 5. Molecular and cellular biology. 2004 Oct 1;24(19):8374-85.

[103] Mathias RA, Guise AJ, Cristea IM. Post-translational Modifications Regulate Class IIa Histone Deacetylase (HDAC) Function in Health and Disease*[S]. Molecular & Cellular Proteomics. 2015 Mar 1;14(3):456-70.

[104] Lu J, McKinsey TA, Nicol RL, Olson EN. Signal-dependent activation of the MEF2 transcription factor by dissociation from histone deacetylases. Proceedings of the National Academy of Sciences. 2000 Apr 11;97(8):4070-5.

[105] Backs J, Backs T, Bezprozvannaya S, McKinsey TA, Olson EN. Histone deacetylase 5 acquires calcium/calmodulin-dependent kinase II responsiveness by oligomerization with histone deacetylase 4. Molecular and cellular biology. 2008 May 15;28(10):3437-45.

[106] Stenmark KR, Davie N, Frid M, Gerasimovskaya E, Das M. Role of the adventitia in pulmonary vascular remodeling. Physiology. 2006 Apr;21(2):134-45.

[107] Thenappan T, Chan SY, Weir EK. Role of extracellular matrix in the pathogenesis of pulmonary arterial hypertension. American Journal of Physiology-Heart and Circulatory Physiology. 2018 Nov 1;315(5):H1322-31.

[108] McGrath JC, Deighan C, Briones AM, Shafaroudi MM, McBride M, Adler J, Arribas SM, Vila E, Daly CJ. New aspects of vascular remodelling: the involvement of all vascular cell types. Experimental physiology. 2005 Jul;90(4):469-75.

[109] Seeger W, Pullamsetti SS. Mechanics and mechanisms of pulmonary hypertension—Conference summary and translational perspectives.

[110] Kim SH, Turnbull J, Guimond S. Extracellular matrix and cell signalling: the dynamic cooperation of integrin, proteoglycan and growth factor receptor. The Journal of endocrinology. 2011 Feb 9;209(2):139-51.

[111] Anwar A, Li M, Frid MG, Kumar B, Gerasimovskaya EV, Riddle SR, McKeon BA, Thukaram R, Meyrick BO, Fini MA, Stenmark KR. Osteopontin is an endogenous modulator of the constitutively activated phenotype of pulmonary adventitial fibroblasts in hypoxic pulmonary hypertension. American Journal of Physiology-Lung Cellular and Molecular Physiology. 2012 Jul 1;303(1):L1-1.

[112] Cizmeci-Smith G, Langan E, Youkey J, Showalter LJ, Carey DJ. Syndecan-4 is a primary-response gene induced by basic fibroblast growth factor and arterial injury in vascular smooth muscle cells. Arteriosclerosis, thrombosis, and vascular biology. 1997 Jan;17(1):172-80.

[113] Herum KM, Lunde IG, Skrbic B, Florholmen G, Behmen D, Sjaastad I, Carlson CR, Gomez MF, Christensen G. Syndecan-4 signaling via NFAT regulates extracellular matrix production and cardiac myofibroblast differentiation in response to mechanical stress. Journal of molecular and cellular cardiology. 2013 Jan 1;54:73-81.

[114] Haurani MJ, Pagano PJ. Adventitial fibroblast reactive oxygen species as autacrine and paracrine mediators of remodeling: bellwether for vascular disease?. Cardiovascular research. 2007 Sep 1;75(4):679-89.

[115] Yang W, Zhang J, Wang H, Gao P, Singh M, Shen K, Fang N. Angiotensin II downregulates catalase expression and activity in vascular adventitial fibroblasts through an AT1R/ERK1/2-dependent pathway. Molecular and cellular biochemistry. 2011 Dec;358(1):21-9.

[116] Shen WL, Gao PJ, Che ZQ, Ji KD, Yin M, Yan C, Berk BC, Zhu DL. NAD (P) H oxidase-derived reactive oxygen species regulate angiotensin-II induced adventitial fibroblast phenotypic differentiation. Biochemical and biophysical research communications. 2006 Jan 6;339(1):337-43.

[117] Panzhinskiy E, Zawada WM, Stenmark KR, Das M. Hypoxia induces unique proliferative response in adventitial fibroblasts by activating PDGFβ receptor-JNK1 signalling. Cardiovascular research. 2012 Aug 1;95(3):356-65.

[118] Liu G, Eskin SG, Mikos AG. Integrin αvβ3 is involved in stimulated migration of vascular adventitial fibroblasts by basic fibroblast growth factor but not platelet-derived growth factor. Journal of cellular biochemistry. 2001 Oct 1;83(1):129-35.

[119] Ji J, Xu F, Li L, Chen R, Wang J, Hu WC. Activation of adventitial fibroblasts in the early stage of the aortic transplant vasculopathy in rat. Transplantation. 2010 Apr 27;89(8):945-53.

[120] Barman SA, Chen F, Su Y, Dimitropoulou C, Wang Y, Catravas JD, Han W, Orfi L, Szantai-Kis C, Keri G, Szabadkai I. NADPH oxidase 4 is expressed in pulmonary artery adventitia and contributes to hypertensive vascular remodeling. Arteriosclerosis, thrombosis, and vascular biology. 2014 Aug;34(8):1704-15.

[121] Bishop JE, Butt R, Dawes K, Laurent G. Mechanical load enhances the stimulatory effect of PDGF on pulmonary artery fibroblast procollagen synthesis. Chest. 1998 Jul 1;114(1):S25.

[122] Siques P, López de Pablo ÁL, Brito J, Arribas SM, Flores K, Arriaza K, Naveas N, González MC, Hoorntje A, León-Velarde F, López MR. Nitric oxide and superoxide anion balance in rats exposed to chronic and long term intermittent hypoxia. BioMed Research International. 2014 Oct;2014.

[123] Morris HE, Neves KB, Montezano AC, MacLean MR, Touyz RM. Notch3 signalling and vascular remodelling in pulmonary arterial hypertension. Clinical Science. 2019 Dec;133(24):2481-98.

[124] Qiao L, Xie L, Shi K, Zhou T, Hua Y, Liu H. Notch signaling change in pulmonary vascular remodeling in rats with pulmonary hypertension and its implication for therapeutic intervention. PLoS one. 2012 Dec 12;7(12):e51514.

[125] Tobiume K, Matsuzawa A, Takahashi T, Nishitoh H, Morita KI, Takeda K, Minowa O, Miyazono K, Noda T, Ichijo H. ASK1 is required for sustained activations of JNK/p38 MAP kinases and apoptosis. EMBO reports. 2001 Mar 1;2(3):222-8.

[126] Yu CC, Hsu MJ, Kuo ML, Chen RF, Chen MC, Bai KJ, Yu MC, Chen BC, Lin CH. Thrombin-induced connective tissue growth factor expression in human lung fibroblasts requires the ASK1/JNK/AP-1 pathway. The Journal of Immunology. 2009 Jun 15;182(12):7916-27.

[127] Gana-Weisz M, Haklai R, Marciano D, Egozi Y, Ben-Baruch G, Kloog Y. The Ras antagonists-farnesylthiosalicylic acid induces inhibition of MAPK activation. Biochemical and biophysical research communications. 1997 Oct 29;239(3):900-4.

[128] Lang YD, Hung CL, Wu TY, Wang LF, Chen CM. The renin-angiotensin system mediates hyperoxia-induced collagen production in human lung fibroblasts. Free radical biology and medicine. 2010 Jul 1;49(1):88-95.

[129] Xie Z, Singh M, Singh K. ERK1/2 and JNKs, but not p38 kinase, are involved in reactive oxygen species-mediated induction of osteopontin gene expression by angiotensin II and interleukin-1β in adult rat cardiac fibroblasts. Journal of cellular physiology. 2004 Mar;198(3):399-407.

[130] Kucich U, Rosenbloom JC, Abrams WR, Rosenbloom J. Transforming growth factor-β stabilizes elastin mRNA by a pathway requiring active Smads, protein kinase C-δ, and p38. American journal of respiratory cell and molecular biology. 2002 Feb 1;26(2):183-8.

[131] Zeigler AC, Richardson WJ, Holmes JW, Saucerman JJ. A computational model of cardiac fibroblast signaling predicts context-dependent drivers of myofibroblast differentiation. Journal of molecular and cellular cardiology. 2016 May 1;94:72-81.

[132] Sano M, Fukuda K, Sato T, Kawaguchi H, Suematsu M, Matsuda S, Koyasu S, Matsui H, Yamauchi-Takihara K, Harada M, Saito Y. ERK and p38 MAPK, but not NF-κB, are critically involved in reactive oxygen species–mediated induction of IL-6 by angiotensin II in cardiac fibroblasts. Circulation research. 2001 Oct 12;89(8):661-9.

[133] Lu H, Tian A, Wu J, Yang C, Xing R, Jia P, Yang L, Zhang Y, Zheng X, Li Z. Danshensu inhibits β-adrenergic receptors-mediated cardiac fibrosis by ROS/p38 MAPK axis. Biological and Pharmaceutical Bulletin. 2014 Jun 1;37(6):961-7.

[134] Wang Z, Ren Z, Hu Z, Hu X, Zhang H, Wu H, Zhang M. Angiotensin-II induces phosphorylation of ERK1/2 and promotes aortic adventitial fibroblasts differentiating into myofibroblasts during aortic dissection formation. Journal of molecular histology. 2014 Aug 1;45(4):401-12.

[135] Short M, Nemenoff RA, Zawada WM, Stenmark KR, Das M. Hypoxia induces differentiation of pulmonary artery adventitial fibroblasts into myofibroblasts. American Journal of Physiology-Cell Physiology. 2004 Feb;286(2):C416-25.

[136] Jin X, Fu GX, Li XD, Zhu DL, Gao PJ. Expression and function of osteopontin in vascular adventitial fibroblasts and pathological vascular remodeling. PloS one. 2011 Sep 19;6(9):e23558.

[137] Hall MC, Young DA, Waters JG, Rowan AD, Chantry A, Edwards DR, Clark IM. The comparative role of activator protein 1 and Smad factors in the regulation of Timp-1 and MMP-1 gene expression by transforming growth factor-β1. Journal of Biological Chemistry. 2003 Mar 21;278(12):10304-13.

[138] Misra S, Fu AA, Misra KD, Shergill UM, Leof EB, Mukhopadhyay D. Hypoxia induces a phenotypic switch of fibroblasts to myofibroblasts through a MMP-2/TIMP mediated pathway: Implications for venous neointimal hyperplasia in hemodialysis access. Journal of vascular and interventional radiology: JVIR. 2010 Jun;21(6):896.

[139] Shi Y, Patel S, Niculescu R, Chung W, Desrochers P, Zalewski A. Role of matrix metalloproteinases and their tissue inhibitors in the regulation of coronary cell migration. Arteriosclerosis, thrombosis, and vascular biology. 1999 May;19(5):1150-5.

[140] Murphy G, Willenbrock F. [30] Tissue inhibitors of matrix metalloendopeptidases. Methods in enzymology. 1995 Jan 1;248:496-510.

[141] Cheng YC, Kuo WW, Wu HC, Lai TY, Wu CH, Hwang JM, Wang WH, Tsai FJ, Yang JJ, Huang CY, Chu CH. ZAK induces MMP-2 activity via JNK/p38 signals and reduces MMP-9 activity by increasing TIMP-1/2 expression in H9c2 cardiomyoblast cells. Molecular and cellular biochemistry. 2009 May;325(1):69-77.

[142] Wang Z, Juttermann R, Soloway PD. TIMP-2 is required for efficient activation of proMMP-2 in vivo. Journal of Biological Chemistry. 2000 Aug 25;275(34):26411-5.

[143] Liu P, Zhang C, Feng JB, Zhao YX, Wang XP, Yang JM, Zhang MX, Wang XL, Zhang Y. Cross Talk Among Smad, MAPK, and Integrin Signaling Pathways Enhances Adventitial Fibroblast Functions Activated by Transforming Growth Factor–β1 and Inhibited by Gax. Arteriosclerosis, thrombosis, and vascular biology. 2008 Apr 1;28(4):725-31.

[144] Ren M, Wang B, Zhang J, Liu P, Lv Y, Liu G, Jiang H, Liu F. Smad2 and Smad3 as mediators of the response of adventitial fibroblasts induced by transforming growth factor β1. Molecular medicine reports. 2011 May 1;4(3):561-7.

[145] Tojais NF, Cao A, Lai YJ, Wang L, Chen PI, Alcazar MA, de Jesus Perez VA, Hopper RK, Rhodes CJ, Bill MA, Sakai LY. Codependence of bone morphogenetic protein receptor 2 and transforming growth factor-β in elastic fiber assembly and its perturbation in pulmonary arterial hypertension. Arteriosclerosis, thrombosis, and vascular biology. 2017 Aug;37(8):1559-69.

[146] Orriols M, Gomez-Puerto MC, Ten Dijke P. BMP type II receptor as a therapeutic target in pulmonary arterial hypertension. Cellular and Molecular Life Sciences. 2017 Aug 1;74(16):2979-95.

[147] Li L, Fan D, Wang C, Wang JY, Cui XB, Wu D, Zhou Y, Wu LL. Angiotensin II increases periostin expression via Ras/p38 MAPK/CREB and ERK1/2/TGF-β1 pathways in cardiac fibroblasts. Cardiovascular research. 2011 Jul 1;91(1):80-9.

[148] Yu Q, Stamenkovic I. Cell surface-localized matrix metalloproteinase-9 proteolytically activates TGF-β and promotes tumor invasion and angiogenesis. Genes & development. 2000 Jan 15;14(2):163-76.

[149] Liu Y, Liang C, Liu X, Liao B, Pan X, Ren Y, Fan M, Li M, He Z, Wu J, Wu Z. AGEs increased migration and inflammatory responses of adventitial fibroblasts via RAGE, MAPK and NF-κB pathways. Atherosclerosis. 2010 Jan 1;208(1):34-42.

[150] Ina K, Kitamura H, Tatsukawa S, Fujikura Y. Significance of α-SMA in myofibroblasts emerging in renal tubulointerstitial fibrosis. Histology and histopathology, Vol. 26, nº 7 (2011). 2011.

[151] Fan H, Ma L, Fan B, Wu J, Yang Z, Wang L. Role of PDGFR-β/PI3K/AKT signaling pathway in PDGF-BB induced myocardial fibrosis in rats. American journal of translational research. 2014;6(6):714.

[152] Zhang H, Bajraszewski N, Wu E, Wang H, Moseman AP, Dabora SL, Griffin JD, Kwiatkowski DJ. PDGFRs are critical for PI3K/Akt activation and negatively regulated by mTOR. The Journal of clinical investigation. 2007 Mar 1;117(3):730-8.

[153] Lee SJ, Bae SS, Kim KH, Lee WS, Rhim BY, Hong KW, Kim CD. High glucose enhances MMP-2 production in adventitial fibroblasts via Akt1-dependent NF-κB pathway. FEBS letters. 2007 Sep 4;581(22):4189-94.

[154] Li G, Oparil S, Kelpke SS, Chen YF, Thompson JA. Fibroblast growth factor receptor-1 signaling induces osteopontin expression and vascular smooth muscle cell–dependent adventitial fibroblast migration in vitro. Circulation. 2002 Aug 13;106(7):854-9.

[155] Yu FX, Guan KL. The Hippo pathway: regulators and regulations. Genes & development. 2013 Feb 15;27(4):355-71.

[156] Gholipour M, Tabrizi A. The role of Hippo signaling pathway in physiological cardiac hypertrophy. BioImpacts: BI. 2020;10(4):251.

[157] Zhao B, Li L, Lei Q, Guan KL. The Hippo–YAP pathway in organ size control and tumorigenesis: an updated version. Genes & development. 2010 May 1;24(9):862-74.

[158] Bertero T, Cottrill KA, Lu Y, Haeger CM, Dieffenbach P, Annis S, Hale A, Bhat B, Kaimal V, Zhang YY, Graham BB. Matrix remodeling promotes pulmonary hypertension through feedback mechanoactivation of the YAP/TAZ-miR-130/301 circuit. Cell reports. 2015 Nov 3;13(5):1016-32.

[159] Rog-Zielinska EA, Norris RA, Kohl P, Markwald R. The living scar–cardiac fibroblasts and the injured heart. Trends in molecular medicine. 2016 Feb 1;22(2):99-114.

[160] Scruggs AM, Grabauskas G, Huang SK. The role of KCNMB1 and BK channels in myofibroblast differentiation and pulmonary fibrosis. American journal of respiratory cell and molecular biology. 2020 Feb;62(2):191-203.

[161] Rodman DM, Harral J, Wu S, West J, Hoedt-Miller M, Reese KA, Fagan K. The low-voltage-activated calcium channel CAV3. 1 controls proliferation of human pulmonary artery myocytes. Chest. 2005 Dec 1;128(6):581S-2S.

[162] Cussac LA, Cardouat G, Tiruchellvam Pillai N, Campagnac M, Robillard P, Montillaud A, Guibert C, Gailly P, Marthan R, Quignard JF, Savineau JP. TRPV4 channel mediates adventitial fibroblast activation and adventitial remodeling in pulmonary hypertension. American Journal of Physiology-Lung Cellular and Molecular Physiology. 2020 Jan 1;318(1):L135-46.

[163] Yue Z, Xie J, Yu AS, Stock J, Du J, Yue L. Role of TRP channels in the cardiovascular system. American Journal of Physiology-Heart and Circulatory Physiology. 2015 Feb 1;308(3):H157-82.

[164] Suzuma I, Suzuma K, Ueki K, Hata Y, Feener EP, King GL, Aiello LP. Stretch-induced retinal vascular endothelial growth factor expression is mediated by phosphatidylinositol 3-kinase and protein kinase C (PKC)-ζ but not by stretch-induced ERK1/2, Akt, Ras, or classical/novel PKC pathways. Journal of Biological Chemistry. 2002 Jan 11;277(2):1047-57.

[165] Azeloglu EU, Iyengar R. Signaling networks: information flow, computation, and decision making. Cold Spring Harbor perspectives in biology. 2015 Apr 1;7(4):a005934.

[166] Ay A, Arnosti DN. Mathematical modeling of gene expression: a guide for the perplexed biologist. Critical reviews in biochemistry and molecular biology. 2011 Apr 1;46(2):137-51.

[167] Yoshida K, Holmes JW. Computational models of cardiac hypertrophy. Progress in Biophysics and Molecular Biology. 2021 Jan 1;159:75-85.

[168] Sánchez L, Thieffry D. A logical analysis of the Drosophila gap-gene system. Journal of theoretical Biology. 2001 Jul 21;211(2):115-41.

[169] Goodwin BC. Oscillatory behavior in enzymatic control processes. Advances in enzyme regulation. 1965 Jan 1;3:425-37.

[170] Griffith JS. Mathematics of cellular control processes I. Negative feedback to one gene. Journal of theoretical biology. 1968 Aug 1;20(2):202-8.

[171] Griffith JS. Mathematics of cellular control processes II. Positive feedback to one gene. Journal of Theoretical Biology. 1968 Aug 1;20(2):209-16.

[172] Tan PM, Buchholz KS, Omens JH, McCulloch AD, Saucerman JJ. Predictive model identifies key network regulators of cardiomyocyte mechano-signaling. PLoS Computational Biology. 2017 Nov 13;13(11):e1005854.

[173] Kraeutler MJ, Soltis AR, Saucerman JJ. Modeling cardiac β-adrenergic signaling with normalized-Hill differential equations: comparison with a biochemical model. BMC systems biology. 2010 Dec;4(1):1-2.

[174] Parikh A, Wu J, Blanton RM, Tzanakakis ES. Signaling pathways and gene regulatory networks in cardiomyocyte differentiation. Tissue Engineering Part B: Reviews. 2015 Aug 1;21(4):377-92.

[175] Gilbert SF. Developmental biology. Sinauer Associates; 2000.

[176] Reece JB, Urry LA, Cain ML, Wasserman SA, Minorsky PV, Jackson RB. Campbell biology. Boston: Pearson; 2014 Jan 1.

[177] Reményi A, Schöler HR, Wilmanns M. Combinatorial control of gene expression. Nature structural & molecular biology. 2004 Sep;11(9):812-5.

[178] Nelson TJ, Balza Jr R, Xiao Q, Misra RP. SRF-dependent gene expression in isolated cardiomyocytes: regulation of genes involved in cardiac hypertrophy. Journal of molecular and cellular cardiology. 2005 Sep 1;39(3):479-89.

[179] Wilkins BJ, De Windt LJ, Bueno OF, Braz JC, Glascock BJ, Kimball TF, Molkentin JD. Targeted disruption of NFATc3, but not NFATc4, reveals an intrinsic defect in calcineurin-mediated cardiac hypertrophic growth. Molecular and cellular biology. 2002 Nov 1;22(21):7603-13.

[180] Jeong MY, Kinugawa K, Vinson C, Long CS. AFos dissociates cardiac myocyte hypertrophy and expression of the pathological gene program. Circulation. 2005 Apr 5;111(13):1645-51.

[181] Mercurio F, Murray BW, Shevchenko A, Bennett BL, Young DB, Li JW, Pascual G, Motiwala A, Zhu H, Mann M, Manning AM. IκB kinase (IKK)-associated protein 1, a common component of the heterogeneous IKK complex. Molecular and cellular biology. 1999 Feb 1;19(2):1526-38.

[182] Craig R, Wagner M, McCardle T, Craig AG, Glembotski CC. The cytoprotective effects of the glycoprotein 130 receptor-coupled cytokine, cardiotrophin-1, require activation of NF-κB. Journal of Biological Chemistry. 2001 Oct 5;276(40):37621-9.

[183] Hojayev B, Rothermel BA, Gillette TG, Hill JA. FHL2 binds calcineurin and represses pathological cardiac growth. Molecular and cellular biology. 2012 Oct 1;32(19):4025-34.

[184] Sanna B, Bueno OF, Dai YS, Wilkins BJ, Molkentin JD. Direct and indirect interactions between calcineurin-NFAT and MEK1-extracellular signal-regulated kinase 1/2 signaling pathways regulate cardiac gene expression and cellular growth. Molecular and cellular biology. 2005 Feb 1;25(3):865-78.

[185] Kunisada K, Hirota H, Fujio Y, Matsui H, Tani Y, Yamauchi-Takihara K, Kishimoto T. Activation of JAK-STAT and MAP kinases by leukemia inhibitory factor through gp130 in cardiac myocytes. Circulation. 1996 Nov 15;94(10):2626-32.

[186] Marrero MB, Schieffer B, Paxton WG, Heerdt L, Berk BC, Delafontaine P, Bernstein KE. Direct stimulation of Jak/STAT pathway by the angiotensin II AT 1 receptor. Nature. 1995 May;375(6528):247-50.

[187] Wienerroither S, Shukla P, Farlik M, Majoros A, Stych B, Vogl C, Cheon H, Stark GR, Strobl B, Müller M, Decker T. Cooperative transcriptional activation of antimicrobial genes by STAT and NF-κB pathways by concerted recruitment of the mediator complex. Cell reports. 2015 Jul 14;12(2):300-12.

[188] Feist M, Schwarzfischer P, Heinrich P, Sun X, Kemper J, von Bonin F, Perez-Rubio P, Taruttis F, Rehberg T, Dettmer K, Gronwald W. Cooperative STAT/NF-κB signaling regulates lymphoma metabolic reprogramming and aberrant GOT2 expression. Nature communications. 2018 Apr 17;9(1):1-4.

[189] Manukyan I, Galatioto J, Mascareno E, Bhaduri S, Siddiqui MA. Cross-talk between calcineurin/NFAT and Jak/STAT signalling induces cardioprotective αB-crystallin gene expression in response to hypertrophic stimuli. Journal of cellular and molecular medicine. 2010 Jun;14(6b):1707-16.

[190] Phiel CJ, Gabbeta V, Parsons LM, Rothblat D, Harvey RP, McHugh KM. Differential binding of an SRF/NK-2/MEF2 transcription factor complex in normal versus neoplastic smooth muscle tissues. Journal of Biological Chemistry. 2001 Sep 14;276(37):34637-50.

[191] Pulimood NS, dos Santos Rodrigues W, Atkinson DA, Mooney SM, Medina AE. The role of CREB, SRF, and MEF2 in activity-dependent neuronal plasticity in the visual cortex. Journal of Neuroscience. 2017 Jul 12;37(28):6628-37.

[192] Kolodziejczyk SM, Wang L, Balazsi K, DeRepentigny Y, Kothary R, Megeney LA. MEF2 is upregulated during cardiac hypertrophy and is required for normal post-natal growth of the myocardium. Current Biology. 1999 Oct 21;9(20):1203-6.

[193] Kato Y, Zhao M, Morikawa A, Sugiyama T, Chakravortty D, Koide N, Yoshida T, Tapping RI, Yang Y, Yokochi T, Lee JD. Big mitogen-activated kinase regulates multiple members of the MEF2 protein family. Journal of Biological Chemistry. 2000 Jun 16;275(24):18534-40.

[194] Schratt G, Weinhold B, Lundberg AS, Schuck S, Berger J, Schwarz H, Weinberg RA, Rüther U, Nordheim A. Serum response factor is required for immediate-early gene activation yet is dispensable for proliferation of embryonic stem cells. Molecular and cellular biology. 2001 Apr 15;21(8):2933-43.

[195] Okamoto R, Li Y, Noma K, Hiroi Y, Liu PY, Taniguchi M, Ito M, Liao JK. FHL2 prevents cardiac hypertrophy in mice with cardiac-specific deletion of ROCK2. The FASEB Journal. 2013 Apr;27(4):1439-49.

[196] Philippar U, Schratt G, Dieterich C, Müller JM, Galgóczy P, Engel FB, Keating MT, Gertler F, Schüle R, Vingron M, Nordheim A. The SRF target gene Fhl2 antagonizes RhoA/MAL-dependent activation of SRF. Molecular cell. 2004 Dec 22;16(6):867-80.

[197] Salameh A, Karl S, Djilali H, Dhein S, Janousek J, Daehnert I. Opposing and synergistic effects of cyclic mechanical stretch and α-or β-adrenergic stimulation on the cardiac gap junction protein Cx43. Pharmacological research. 2010 Dec 1;62(6):506-13.

[198] Wang H, Xu J, Lazarovici P, Quirion R, Zheng W. cAMP response element-binding protein (CREB): a possible signaling molecule link in the pathophysiology of schizophrenia. Frontiers in molecular neuroscience. 2018 Aug 30;11:255.

[199] Ogawa C, Tone Y, Tsuda M, Peter C, Waldmann H, Tone M. TGF-β–mediated Foxp3 gene expression is cooperatively regulated by Stat5, Creb, and AP-1 through CNS2. The Journal of Immunology. 2014 Jan 1;192(1):475-83.

[200] Brown PH, Chen TK, Birrer MJ. Mechanism of action of a dominant-negative mutant of c-Jun. Oncogene. 1994 Mar 1;9(3):791-9.

[201] Omura T, Yoshiyama M, Yoshida K, Nakamura Y, Kim S, Iwao H, Takeuchi K, Yoshikawa J. Dominant negative mutant of c-Jun inhibits cardiomyocyte hypertrophy induced by endothelin 1 and phenylephrine. Hypertension. 2002 Jan 1;39(1):81-6.

[202] Aitken S, Magi S, Alhendi AM, Itoh M, Kawaji H, Lassmann T, Daub CO, Arner E, Carninci P, Forrest AR, Hayashizaki Y. Transcriptional dynamics reveal critical roles for

non-coding RNAs in the immediate-early response. PLoS computational biology. 2015 Apr 17;11(4):e1004217.

[203] Morton S, Davis RJ, McLaren A, Cohen P. A reinvestigation of the multisite phosphorylation of the transcription factor c-Jun. The EMBO journal. 2003 Aug 1;22(15):3876-86.

[204] Gupta S, Barrett T, Whitmarsh AJ, Cavanagh J, Sluss HK, Derijard B, Davis RJ. Selective interaction of JNK protein kinase isoforms with transcription factors. The EMBO journal. 1996 Jun;15(11):2760-70.

[205] Lemaire-Ewing S, Berthier A, Royer MC, Logette E, Corcos L, Bouchot A, Monier S, Prunet C, Raveneau M, Rébé C, Desrumaux C. 7β-Hydroxycholesterol and 25-hydroxycholesterol-induced interleukin-8 secretion involves a calcium-dependent activation of c-fos via the ERK1/2 signaling pathway in THP-1 cells. Cell biology and toxicology. 2009 Apr;25(2):127-39.

[206] Olson AK, Ledee D, Iwamoto K, Kajimoto M, Priddy CO, Isern N, Portman MA. C-Myc induced compensated cardiac hypertrophy increases free fatty acid utilization for the citric acid cycle. Journal of molecular and cellular cardiology. 2013 Feb 1;55:156-64.

[207] Torsoni AS, Constancio SS, Nadruz Jr W, Hanks SK, Franchini KG. Focal adhesion kinase is activated and mediates the early hypertrophic response to stretch in cardiac myocytes. Circulation research. 2003 Jul 25;93(2):140-7.

[208] Marttila M, Hautala N, Paradis P, Toth M, Vuolteenaho O, Nemer M, Ruskoaho H. GATA4 mediates activation of the B-type natriuretic peptide gene expression in response to hemodynamic stress. Endocrinology. 2001 Nov 1;142(11):4693-700.

[209] Van Berlo JH, Elrod JW, Aronow BJ, Pu WT, Molkentin JD. Serine 105 phosphorylation of transcription factor GATA4 is necessary for stress-induced cardiac hypertrophy in vivo. Proceedings of the National Academy of Sciences. 2011 Jul 26;108(30):12331-6.

[210] Lee Y, Shioi T, Kasahara H, Jobe SM, Wiese RJ, Markham BE, Izumo S. The cardiac tissue-restricted homeobox protein Csx/Nkx2. 5 physically associates with the zinc finger protein GATA4 and cooperatively activates atrial natriuretic factor gene expression. Molecular and cellular biology. 1998 Jun 1;18(6):3120-9.

[211] Evans T. Regulation of cardiac gene expression by GATA-4/5/6. Trends in cardiovascular medicine. 1997 Apr 1;7(3):75-83.

[212] Liang Q, De Windt LJ, Witt SA, Kimball TR, Markham BE, Molkentin JD. The transcription factors GATA4 and GATA6 regulate cardiomyocyte hypertrophy in vitro and in vivo. Journal of Biological Chemistry. 2001 Aug 10;276(32):30245-53.

[213] Brunet A, Bonni A, Zigmond MJ, Lin MZ, Juo P, Hu LS, Anderson MJ, Arden KC, Blenis J, Greenberg ME. Akt promotes cell survival by phosphorylating and inhibiting a Forkhead transcription factor. cell. 1999 Mar 19;96(6):857-68.

[214] Skurk C, Izumiya Y, Maatz H, Razeghi P, Shiojima I, Sandri M, Sato K, Zeng L, Schiekofer S, Pimentel D, Lecker S. The FOXO3a transcription factor regulates cardiac myocyte size downstream of AKT signaling. Journal of Biological Chemistry. 2005 May 27;280(21):20814-23.

[215] Etienne W, Meyer MH, Peppers J, Meyer Jr RA. Comparison of mRNA gene expression by RT-PCR and DNA microarray. Biotechniques. 2004 Apr;36(4):618-26.

[216] Finotello F, Di Camillo B. Measuring differential gene expression with RNA-seq: challenges and strategies for data analysis. Briefings in functional genomics. 2015 Mar 1;14(2):130-42.

[217] Park PJ. ChIP–seq: advantages and challenges of a maturing technology. Nature reviews genetics. 2009 Oct;10(10):669-80.

[218] Pepke S, Wold B, Mortazavi A. Computation for ChIP-seq and RNA-seq studies. Nature methods. 2009 Nov;6(11):S22-32.

[219] Ji Z, He L, Rotem A, Janzer A, Cheng CS, Regev A, Struhl K. Genome-scale identification of transcription factors that mediate an inflammatory network during breast cellular transformation. Nature communications. 2018 May 25;9(1):1-3.

[220] Ahmed M, Min DS, Kim DR. Integrating binding and expression data to predict transcription factors combined function. BMC genomics. 2020 Dec;21(1):1-9.

[221] Roopra A. MAGIC: A tool for predicting transcription factors and cofactors driving gene sets using ENCODE data. PLoS computational biology. 2020 Apr 6;16(4):e1007800.

[222] Han H, Cho JW, Lee S, Yun A, Kim H, Bae D, Yang S, Kim CY, Lee M, Kim E, Lee S. TRRUST v2: an expanded reference database of human and mouse transcriptional regulatory interactions. Nucleic acids research. 2018 Jan 4;46(D1):D380-6.

[223] Jayaram N, Usvyat D, Martin AC. Evaluating tools for transcription factor binding site prediction. BMC bioinformatics. 2016 Dec;17(1):1-2.

[224] Janky RS, Verfaillie A, Imrichova H, Van de Sande B, Standaert L, Christiaens V, Hulselmans G, Herten K, Naval Sanchez M, Potier D, Svetlichnyy D. iRegulon: from a gene list to a gene regulatory network using large motif and track collections. PLoS computational biology. 2014 Jul 24;10(7):e1003731.

[225] Kim GB, Gao Y, Palsson BO, Lee SY. DeepTFactor: A deep learning-based tool for the prediction of transcription factors. Proceedings of the National Academy of Sciences. 2021 Jan 12;118(2).

[226] Zrimec J, Buric F, Kokina M, Garcia V, Zelezniak A. Learning the regulatory code of gene expression. Frontiers in Molecular Biosciences. 2021;8.

[227] Matys V, Fricke E, Geffers R, Gößling E, Haubrock M, Hehl R, Hornischer K, Karas D, Kel AE, Kel-Margoulis OV, Kloos DU. TRANSFAC®: transcriptional regulation, from patterns to profiles. Nucleic acids research. 2003 Jan 1;31(1):374-8.

[228] Fornes O, Castro-Mondragon JA, Khan A, Van der Lee R, Zhang X, Richmond PA, Modi BP, Correard S, Gheorghe M, Baranašić D, Santana-Garcia W. JASPAR 2020: update of the open-access database of transcription factor binding profiles. Nucleic acids research. 2020 Jan 8;48(D1):D87-92.

[229] Hume MA, Barrera LA, Gisselbrecht SS, Bulyk ML. UniPROBE, update 2015: new tools and content for the online database of protein-binding microarray data on protein–DNA interactions. Nucleic acids research. 2015 Jan 28;43(D1):D117-22.

[230] Sharova LV, Sharov AA, Nedorezov T, Piao Y, Shaik N, Ko MS. Database for mRNA half-life of 19977 genes obtained by DNA microarray analysis of pluripotent and differentiating mouse embryonic stem cells. DNA research. 2009 Feb 1;16(1):45-58.

[231] Lal H, Verma SK, Smith M, Guleria RS, Lu G, Foster DM, Dostal DE. Stretch-induced MAP kinase activation in cardiac myocytes: differential regulation through β1-integrin and focal adhesion kinase. Journal of molecular and cellular cardiology. 2007 Aug 1;43(2):137-47.

[232] Wang Z, Gerstein M, Snyder M. RNA-Seq: a revolutionary tool for transcriptomics. Nature reviews genetics. 2009 Jan;10(1):57-63.

[233] Campbell PJ, Stephens PJ, Pleasance ED, O'Meara S, Li H, Santarius T, Stebbings LA, Leroy C, Edkins S, Hardy C, Teague JW. Identification of somatically acquired rearrangements in cancer using genome-wide massively parallel paired-end sequencing. Nature genetics. 2008 Jun;40(6):722-9.

[234] Corley SM, MacKenzie KL, Beverdam A, Roddam LF, Wilkins MR. Differentially expressed genes from RNA-Seq and functional enrichment results are affected by the choice of single-end versus paired-end reads and stranded versus non-stranded protocols. BMC genomics. 2017 Dec;18(1):1-3.

[235] Feng ZP, Collin F, Speed TP. Combining Single and Paired End RNA-seq Data for Differential Expression Analyses. InStatistical Analysis for High-Dimensional Data 2016 (pp. 155-188). Springer, Cham.

[236] Williams CR, Baccarella A, Parrish JZ, Kim CC. Trimming of sequence reads alters RNA-Seq gene expression estimates. BMC bioinformatics. 2016 Dec;17(1):1-3.

[237] Del Fabbro C, Scalabrin S, Morgante M, Giorgi FM. An extensive evaluation of read trimming effects on Illumina NGS data analysis. PloS one. 2013 Dec 23;8(12):e85024.

[238] Liao Y, Shi W. Read trimming is not required for mapping and quantification of RNA-seq reads at the gene level. NAR genomics and bioinformatics. 2020 Sep;2(3):lqaa068.

[239] Dobin A, Davis CA, Schlesinger F, Drenkow J, Zaleski C, Jha S, Batut P, Chaisson M, Gingeras TR. STAR: ultrafast universal RNA-seq aligner. Bioinformatics. 2013 Jan 1;29(1):15-21.

[240] Kim D, Paggi JM, Park C, Bennett C, Salzberg SL. Graph-based genome alignment and genotyping with HISAT2 and HISAT-genotype. Nature biotechnology. 2019 Aug;37(8):907-15.

[241] Anders S, Pyl PT, Huber W. HTSeq—a Python framework to work with high-throughput sequencing data. bioinformatics. 2015 Jan 15;31(2):166-9.

[242] Liao Y, Smyth GK, Shi W. featureCounts: an efficient general purpose program for assigning sequence reads to genomic features. Bioinformatics. 2014 Apr 1;30(7):923-30.

[243] Liao Y, Smyth GK, Shi W. The R package Rsubread is easier, faster, cheaper and better for alignment and quantification of RNA sequencing reads. Nucleic acids research. 2019 May 7;47(8):e47-.

[244] Yoon S, Nam D. Gene dispersion is the key determinant of the read count bias in differential expression analysis of RNA-seq data. BMC genomics. 2017 Dec;18(1):1-1.

[245] Hafemeister C, Satija R. Normalization and variance stabilization of single-cell RNA-seq data using regularized negative binomial regression. Genome biology. 2019 Dec;20(1):1-5.

[246] Evans C, Hardin J, Stoebel DM. Selecting between-sample RNA-Seq normalization methods from the perspective of their assumptions. Briefings in bioinformatics. 2018 Sep;19(5):776-92.

[247] Wagner GP, Kin K, Lynch VJ. Measurement of mRNA abundance using RNA-seq data: RPKM measure is inconsistent among samples. Theory in biosciences. 2012 Dec 1;131(4):281-5.

[248] Love MI, Huber W, Anders S. Moderated estimation of fold change and dispersion for RNA-seq data with DESeq2. Genome biology. 2014 Dec;15(12):1-21.

[249] Robinson MD, McCarthy DJ, Smyth GK. edgeR: a Bioconductor package for differential expression analysis of digital gene expression data. Bioinformatics. 2010 Jan 1;26(1):139-40.

[250] Zhao S, Ye Z, Stanton R. Misuse of RPKM or TPM normalization when comparing across samples and sequencing protocols. Rna. 2020 Aug 1;26(8):903-9.

[251] Robinson MD, Oshlack A. A scaling normalization method for differential expression analysis of RNA-seq data. Genome biology. 2010 Mar;11(3):1-9.

[252] Li P, Piao Y, Shon HS, Ryu KH. Comparing the normalization methods for the differential analysis of Illumina high-throughput RNA-Seq data. BMC bioinformatics. 2015 Dec;16(1):1-9.

[253] Hafemeister C, Satija R. Normalization and variance stabilization of single-cell RNA-seq data using regularized negative binomial regression. Genome biology. 2019 Dec;20(1):1-5.

[254] Benjamini Y, Hochberg Y. Controlling the false discovery rate: a practical and powerful approach to multiple testing. Journal of the Royal statistical society: series B (Methodological). 1995 Jan;57(1):289-300.

[255] Klamt S, Saez-Rodriguez J, Lindquist JA, Simeoni L, Gilles ED. A methodology for the structural and functional analysis of signaling and regulatory networks. BMC bioinformatics. 2006 Dec;7(1):1-26.

[256] Ben-Dor A, Shamir R, Yakhini Z. Clustering gene expression patterns. Journal of computational biology. 1999 Oct 1;6(3-4):281-97.

[257] Murtagh F, Contreras P. Algorithms for hierarchical clustering: an overview. Wiley Interdisciplinary Reviews: Data Mining and Knowledge Discovery. 2012 Jan;2(1):86-97.

[258] Likas A, Vlassis N, Verbeek JJ. The global k-means clustering algorithm. Pattern recognition. 2003 Feb 1;36(2):451-61.

[259] McKinney BA, Reif DM, Ritchie MD, Moore JH. Machine learning for detecting gene-gene interactions. Applied bioinformatics. 2006 Jun;5(2):77-88.

[260] Razaghi-Moghadam Z, Nikoloski Z. Supervised learning of gene-regulatory networks based on graph distance profiles of transcriptomics data. NPJ systems biology and applications. 2020 Jun 30;6(1):1-8.

[261] Kanehisa M, Goto S. KEGG: kyoto encyclopedia of genes and genomes. Nucleic acids research. 2000 Jan 1;28(1):27-30.

[262] Gopalan SM, Flaim C, Bhatia SN, Hoshijima M, Knoell R, Chien KR, Omens JH, McCulloch AD. Anisotropic stretch-induced hypertrophy in neonatal ventricular myocytes micropatterned on deformable elastomers. Biotechnology and bioengineering. 2003 Mar 5;81(5):578-87.

[263] Bullard TA, Hastings JL, Davis JM, Borg TK, Price RL. Altered PKC expression and phosphorylation in response to the nature, direction, and magnitude of mechanical stretch. Canadian journal of physiology and pharmacology. 2007 Feb;85(2):243-50.

[264] Mansour H, de Tombe PP, Samarel AM, Russell B. Restoration of resting sarcomere length after uniaxial static strain is regulated by protein kinase Cε and focal adhesion kinase. Circulation research. 2004 Mar 19;94(5):642-9.

[265] Cingolani HE, Ennis IL, Aiello EA, Pérez NG. Role of autocrine/paracrine mechanisms in response to myocardial strain. Pflügers Archiv-European Journal of Physiology. 2011 Jul;462(1):29-38.

[266] Yang H, Schmidt LP, Wang Z, Yang X, Shao Y, Borg TK, Markwald R, Runyan R, Gao BZ. Dynamic myofibrillar remodeling in live cardiomyocytes under static stretch. Scientific reports. 2016 Feb 10;6(1):1-2.

[267] Olivetti G, Melissari M, Balbi T, Quaini F, Cigola E, Sonnenblick EH, Anversa P. Myocyte cellular hypertrophy is responsible for ventricular remodelling in the hypertrophied heart of middle aged individuals in the absence of cardiac failure. Cardiovasc. Res. 28, 1994;1199–1208.

[268] Mirams GR, Pathmanathan P, Gray RA, Challenor P, Clayton RH. Uncertainty and variability in computational and mathematical models of cardiac physiology. J. Physiol. 2016;594:6833–6847.

[269] Pathmanathan P, Cordeiro JM, Gray RA. Comprehensive uncertainty quantification and sensitivity analysis for cardiac action potential models. Front. Physiol. 2019;10:721.

[270] Fox BL. Strategies for Quasi-Monte Carlo, vol. 22. New York, NY: Springer Science & Business Media. 1999.

[271] Xiu D, Karniadakis GE. The Wiener–Askey polynomial chaos for stochastic differential equations. SIAM J. Sci. Comput. 2002;24:619–644.

[272] Morris MK, Saez-Rodriguez J, Sorger PK, Lauffenburger DA. Logic-based models for the analysis of cell signaling networks. Biochemistry. 2010 Apr 20;49(15):3216-24.

[273] Rohatgi A. WebPlotDigitizer, Version: 4.2. April, 2019, San Francisco, CA. https://automeris.io/WebPlotDigitizer. 2011

[274] Anderson HDI, Wang F, Gardner DG. Role of the epidermal growth factor receptor in signaling strain-dependent activation of the brain natriuretic peptide gene. J. Biol. Chem. 2004;279:9287–9297.

[275] Tennøe S, Halnes G, Einevoll GT. Uncertainpy: a Python toolbox for uncertainty quantification and sensitivity analysis in computational neuroscience. Front. Neuroinformatics 2018;12:49.

[276] Xiu D, Hesthaven JS. High-order collocation methods for differential equations with random inputs. SIAM J. Sci. Comput. 2005;27:1118–1139.

[277] Eck VG, Donders WP, Sturdy J, Feinberg J, Delhaas T, Hellevik LR, Huberts W. A guide to uncertainty quantification and sensitivity analysis for cardiovascular applications. Int. J. Numer. Methods Biomed. Eng. 2016;32:e02755.

[278] Oladyshkin S, Nowak W. Data-driven uncertainty quantification using the arbitrary polynomial chaos expansion. Reliab. Eng. Syst. Saf. 2012;106:179–190.

[279] Ohashi N, Urushihara M, Satou R, Kobori H. Glomerular angiotensinogen is induced in mesangial cells in diabetic rats via reactive oxygen species–ERK/JNK pathways. Hypertens. Res. 2010;33:1174–1181.

[280] Kawamura S, Miyamoto S, Brown JH. Initiation and transduction of stretch-induced Rhoa and Rac1 activation through caveolae cytoskeletal regulation of ERK translocation. J. Biol. Chem. 2003;278:31 111–31 117.

[281] Loughna PT, Mason P, Bayol S, Brownson C. The LIM-domain protein FHL1 (SLIM1) exhibits functional regulation in skeletal muscle. Mol. Cell Biol. Res. Commun. 2000;3:136–140.

[282] Fimia GM, Evangelisti C, Alonzi T, Romani M, Fratini F, Paonessa G, Ippolito G, Tripodi M, Piacentini M. Conventional protein kinase C inhibition prevents alpha interferonmediated hepatitis C virus replicon clearance by impairing stat activation. J. Virol. 2004;78:12 809–12 816.

[283] Aksamitiene E, Kiyatkin A, Kholodenko BN. Cross-talk between mitogenic Ras/MAPK and survival PI3K/Akt pathways: a fine balance. 2012;40(1):139-46.

[284] Castellano E, Downward J. Ras interaction with PI3K: more than just another effector pathway. Genes Cancer. 2011;2:261–274.

[285] Avizienyte E, Frame MC. Src and FAK signalling controls adhesion fate and the epithelial-to-mesenchymal transition. Curr. Opin Cell Biol. 2005;17:542–547.

[286] Zhao X, Ito A, Kane CD, Liao T-S, Bolger TA, Lemrow SM, Means AR, Yao T-P. The modular nature of histone deacetylase HDAC4 confers phosphorylation-dependent intracellular trafficking. J. Biol. Chem. 2001;276:35 042–35 048.

[287] Grossman W, Paulus WJ. Myocardial stress and hypertrophy: a complex interface between biophysics and cardiac remodeling. The Journal of clinical investigation. 2013 Sep 3;123(9):3701-3.

[288] Saucerman JJ, Tan PM, Buchholz KS, McCulloch AD, Omens JH. Mechanical regulation of gene expression in cardiac myocytes and fibroblasts. Nature Reviews Cardiology. 2019 Jun;16(6):361-78.

[289] Lammerding JA, Kamm RD, Lee RT. Mechanotransduction in cardiac myocytes. Annals of the New York Academy of Sciences. 2004 May;1015(1):53-70.

[290] Davis J, Davis LC, Correll RN, Makarewich CA, Schwanekamp JA, Moussavi-Harami F, Wang D, York AJ, Wu H, Houser SR, Seidman CE. A tension-based model distinguishes hypertrophic versus dilated cardiomyopathy. Cell. 2016 May 19;165(5):1147-59.

[291] Camelliti P, Gallagher JO, Kohl P, McCulloch AD. Micropatterned cell cultures on elastic membranes as an in vitro model of myocardium. Nature protocols. 2006 Aug;1(3):1379-91.

[292] Pfeiffer ER, Wright AT, Edwards AG, Stowe JC, McNall K, Tan J, Niesman I, Patel HH, Roth DM, Omens JH, McCulloch AD. Caveolae in ventricular myocytes are required for stretch-dependent conduction slowing. Journal of molecular and cellular cardiology. 2014 Nov 1;76:265-74.

[293] Andrews S. FastQC: a quality control tool for high throughput sequence data. 2010.

[294] Gordon A, Hannon GJ. Fastx-toolkit. FASTQ/A short-reads preprocessing tools (unpublished) http://hannonlab. cshl. edu/fastx_toolkit. 2010 Jan 20;5.

[295] Bi R, Liu P. Sample size calculation while controlling false discovery rate for differential expression analysis with RNA-sequencing experiments. BMC bioinformatics. 2016 Dec;17(1):1-3.

[296] Chen J, Bardes EE, Aronow BJ, Jegga AG. ToppGene Suite for gene list enrichment analysis and candidate gene prioritization. Nucleic acids research. 2009 Jul 1;37(suppl_2):W305-11.

[297] Ryall KA, Holland DO, Delaney KA, Kraeutler MJ, Parker AJ, Saucerman JJ. Network reconstruction and systems analysis of cardiac myocyte hypertrophy signaling. Journal of Biological Chemistry. 2012 Dec 7;287(50):42259-68.

[298] Potier D, Davie K, Hulselmans G, Sanchez MN, Haagen L, Koldere D, Celik A, Geurts P, Christiaens V, Aerts S. Mapping gene regulatory networks in Drosophila eye development by large-scale transcriptome perturbations and motif inference. Cell reports. 2014 Dec 24;9(6):2290-303.

[299] Wingender E, Chen X, Fricke E, Geffers R, Hehl R, Liebich I, Krull M, Matys V, Michael H, Ohnhäuser R, Prüß M. The TRANSFAC system on gene expression regulation. Nucleic acids research. 2001 Jan 1;29(1):281-3.

[300] Shannon P, Markiel A, Ozier O, Baliga NS, Wang JT, Ramage D, Amin N, Schwikowski B, Ideker T. Cytoscape: a software environment for integrated models of biomolecular interaction networks. Genome research. 2003 Nov 1;13(11):2498-504.

[301] Koschützki D, Schreiber F. Centrality analysis methods for biological networks and their application to gene regulatory networks. Gene regulation and systems biology. 2008 Jan;2:GRSB-S702.

[302] Yoon J, Blumer A, Lee K. An algorithm for modularity analysis of directed and weighted biological networks based on edge-betweenness centrality. Bioinformatics. 2006 Dec 15;22(24):3106-8.

[303] Tamura I, Rosenbloom J, Macarak E, Chaqour B. Regulation of Cyr61 gene expression by mechanical stretch through multiple signaling pathways. American Journal of Physiology-Cell Physiology. 2001 Nov 1;281(5):C1524-32.

[304] Wang Y, Zhang Y, Ding G, May HI, Xu J, Gillette TG, Wang H, Wang ZV. Temporal dynamics of cardiac hypertrophic growth in response to pressure overload. American Journal of Physiology-Heart and Circulatory Physiology. 2017 Dec 1;313(6):H1119-29.

[305] Rysä J, Tokola H, Ruskoaho H. Mechanical stretch induced transcriptomic profiles in cardiac myocytes. Scientific reports. 2018 Mar 16;8(1):1-4.

[306] Kesanakurti D, Chetty C, Maddirela DR, Gujrati M, Rao JS. Essential role of cooperative NF-κB and Stat3 recruitment to ICAM-1 intronic consensus elements in the regulation of radiation-induced invasion and migration in glioma. Oncogene. 2013 Oct;32(43):5144-55.

[307] Pulimood NS, dos Santos Rodrigues W, Atkinson DA, Mooney SM, Medina AE. The role of CREB, SRF, and MEF2 in activity-dependent neuronal plasticity in the visual cortex. Journal of Neuroscience. 2017 Jul 12;37(28):6628-37.

[308] Lee AA, McCulloch AD. Multiaxial myocardial mechanics and extracellular matrix remodeling: mechanochemical regulation of cardiac fibroblast function. InAnalytical and Quantitative Cardiology 1997 (pp. 227-240). Springer, Boston, MA.

[309] Vrancken SL, van Heijst AF, de Boode WP. Neonatal hemodynamics: from developmental physiology to comprehensive monitoring. Frontiers in pediatrics. 2018 Apr 5;6:87.

[310] Iwaki K, Sukhatme VP, Shubeita HE, Chien KR. Alpha-and beta-adrenergic stimulation induces distinct patterns of immediate early gene expression in neonatal rat myocardial cells. fos/jun expression is associated with sarcomere assembly; Egr-1 induction is primarily an alpha 1-mediated response. Journal of Biological Chemistry. 1990 Aug 15;265(23):13809-17.

[311] Saadane N, Alpert L, Chalifour LE. Expression of immediate early genes, GATA‐4, and Nkx‐2.5 in adrenergic‐induced cardiac hypertrophy and during regression in adult mice. British journal of pharmacology. 1999 Jul;127(5):1165-76.

[312] Patel A, Sharif-Naeini R, Folgering JR, Bichet D, Duprat F, Honoré E. Canonical TRP channels and mechanotransduction: from physiology to disease states. Pflügers Archiv-European Journal of Physiology. 2010 Aug;460(3):571-81.

[313] Windmueller R, Morrisey EE. Hippo and cardiac hypertrophy: a complex interaction. 2015; 832-834.

[314] Tian Y, Liu Y, Wang T, Zhou N, Kong J, Chen L, Snitow M, Morley M, Li D, Petrenko N, Zhou S. A microRNA-Hippo pathway that promotes cardiomyocyte proliferation and cardiac regeneration in mice. Science translational medicine. 2015 Mar 18;7(279):279ra38-.

[315] Jeyaraj SC, Unger NT, Chotani MA. Rap1 GTPases: an emerging role in the cardiovasculature. Life sciences. 2011 Apr 11;88(15-16):645-52.

[316] Cutler MJ, Jeyaraj D, Rosenbaum DS. Cardiac electrical remodeling in health and disease. Trends in pharmacological sciences. 2011 Mar 1;32(3):174-80.

[317] Yamada K, Green KG, Samarel AM, Saffitz JE. Distinct pathways regulate expression of cardiac electrical and mechanical junction proteins in response to stretch. Circulation research. 2005 Aug 19;97(4):346-53.

[318] Cao S, Aboelkassem Y, Wang A, Valdez-Jasso D, Saucerman JJ, Omens JH, McCulloch AD. Quantification of model and data uncertainty in a network analysis of cardiac myocyte mechanosignalling. Philosophical Transactions of the Royal Society A. 2020 Jun 12;378(2173):20190336.

[319] Wang N, Zhou Z, Liao X, Zhang T. Role of microRNAs in cardiac hypertrophy and heart failure. IUBMB life. 2009 Jun;61(6):566-71.

[320] Wang J, Yang X. The function of miRNA in cardiac hypertrophy. Cellular and molecular life sciences. 2012 Nov;69(21):3561-70.

[321] Herum KM, Choppe J, Kumar A, Engler AJ, McCulloch AD. Mechanical regulation of cardiac fibroblast profibrotic phenotypes. Molecular biology of the cell. 2017 Jul 7;28(14):1871-82.

[322] Grieb M, Burkovski A, Sträng JE, Kraus JM, Groß A, Palm G, Kühl M, Kestler HA. Predicting variabilities in cardiac gene expression with a boolean network incorporating uncertainty. PloS one. 2015 Jul 24;10(7):e0131832.

[323] Boyd R, Rätsep MT, Ding LL, Wang HD. ETA and ETB receptors are expressed in vascular adventitial fibroblasts. American Journal of Physiology-Heart and Circulatory Physiology. 2011 Dec;301(6):H2271-8.

[324] El Kasmi KC, Pugliese SC, Riddle SR, Poth JM, Anderson AL, Frid MG, Li M, Pullamsetti SS, Savai R, Nagel MA, Fini MA. Adventitial fibroblasts induce a distinct proinflammatory/profibrotic macrophage phenotype in pulmonary hypertension. The Journal of Immunology. 2014 Jul 15;193(2):597-609.

[325] Reddy VS, Harskamp RE, Van Ginkel MW, Calhoon J, Baisden CE, Kim IS, Valente AJ, Chandrasekar B. Interleukin‐18 stimulates fibronectin expression in primary human cardiac fibroblasts via PI3K‐Akt‐dependent NF‐κB activation. Journal of cellular physiology. 2008 Jun;215(3):697-707.

[326] Zhang J, Lo CS. Regulation of fibronectin expression by PDGF-BB And IGF-I in cultured rat thoracic aortic adventitial fibroblasts. Cell biology international. 1995 Jun 1;19(6):517-26.

[327] Lin S, Ma S, Lu P, Cai W, Chen Y, Sheng J. Effect of CTRP3 on activation of adventitial fibroblasts induced by TGF-β1 from rat aorta in vitro. International journal of clinical and experimental pathology. 2014;7(5):2199.

[328] Zalewski A, Shi Y. Vascular myofibroblasts: lessons from coronary repair and remodeling. Arteriosclerosis, thrombosis, and vascular biology. 1997 Mar;17(3):417-22.

[329] Zhou HY, Chen WD, Zhu DL, Wu LY, Zhang J, Han WQ, Li JD, Yan C, Gao PJ. The PDE1A-PKCα signaling pathway is involved in the upregulation of α-smooth muscle actin by TGF-β1 in adventitial fibroblasts. Journal of vascular research. 2010;47(1):9-15.

[330] Zhang J, Tang L, Dai F, Qi Y, Yang L, Liu Z, Deng L, Yao W. ROCK inhibitors alleviate myofibroblast transdifferentiation and vascular remodeling via decreasing TGFβ1-mediated RhoGDI expression. General physiology and biophysics. 2019 Jun 20;38(4):271-80.

[331] Wang B, Omar A, Angelovska T, Drobic V, Rattan SG, Jones SC, Dixon IM. Regulation of collagen synthesis by inhibitory Smad7 in cardiac myofibroblasts. American Journal of Physiology-Heart and Circulatory Physiology. 2007 Aug;293(2):H1282-90.

[332] Khalil N, Xu YD, O'Connor R, Duronio V. Proliferation of pulmonary interstitial fibroblasts is mediated by transforming growth factor-β1-induced release of extracellular fibroblast growth factor-2 and phosphorylation of p38 MAPK and JNK. Journal of Biological Chemistry. 2005 Dec 30;280(52):43000-9.

[333] Sullivan DE, Ferris M, Nguyen H, Abboud E, Brody AR. TNF‐α induces TGF‐β1 expression in lung fibroblasts at the transcriptional level via AP‐1 activation. Journal of cellular and molecular medicine. 2009 Aug 2;13(8b):1866-76.

[334] Csányi G, Taylor WR, Pagano PJ. NOX and inflammation in the vascular adventitia. Free Radical Biology and Medicine. 2009 Nov 1;47(9):1254-66.

[335] Budas GR, Boehm M, Kojonazarov B, Viswanathan G, Tian X, Veeroju S, Novoyatleva T, Grimminger F, Hinojosa-Kirschenbaum F, Ghofrani HA, Weissmann N. ASK1 inhibition halts disease progression in preclinical models of pulmonary arterial hypertension. American journal of respiratory and critical care medicine. 2018 Feb 1;197(3):373-85.

[336] Chandel NS, McClintock DS, Feliciano CE, Wood TM, Melendez JA, Rodriguez AM, Schumacker PT. Reactive oxygen species generated at mitochondrial complex III stabilize hypoxia-inducible factor-1α during hypoxia: a mechanism of O2 sensing. Journal of Biological Chemistry. 2000 Aug 18;275(33):25130-8.

[337] Tieu BC, Ju X, Lee C, Sun H, Lejeune W, Recinos III A, Brasier AR, Tilton RG. Aortic adventitial fibroblasts participate in angiotensin-induced vascular wall inflammation and remodeling. Journal of vascular research. 2011;48(3):261-72.

[338] He RQ, Tang XF, Zhang BL, Li XD, Hong MN, Chen QZ, Han WQ, Gao PJ. Protease-activated receptor 1 and 2 contribute to angiotensin II-induced activation of adventitial fibroblasts from rat aorta. Biochemical and biophysical research communications. 2016 Apr 29;473(2):517-23.

[339] Fei J, Viedt C, Soto U, Elsing C, Jahn L, Kreuzer J. Endothelin-1 and smooth muscle cells: induction of jun amino-terminal kinase through an oxygen radical–sensitive mechanism. Arteriosclerosis, thrombosis, and vascular biology. 2000 May;20(5):1244-9.

[340] Wu J, Thabet SR, Kirabo A, Trott DW, Saleh MA, Xiao L, Madhur MS, Chen W, Harrison DG. Inflammation and mechanical stretch promote aortic stiffening in hypertension through activation of p38 mitogen-activated protein kinase. Circulation research. 2014 Feb 14;114(4):616-25.

[341] Fleenor BS, Marshall KD, Durrant JR, Lesniewski LA, Seals DR. Arterial stiffening with ageing is associated with transforming growth factor‐β1‐related changes in adventitial collagen: reversal by aerobic exercise. The Journal of physiology. 2010 Oct 15;588(20):3971-82.

[342] Chen J, Wu J, Li L, Zou YZ, Zhu DL, Gao PJ. Effect of an acute mechanical stimulus on aortic structure in the transverse aortic constriction mouse model. Clinical and Experimental Pharmacology and Physiology. 2011 Sep;38(9):570-6.

[343] Li G, Chen YF, Kelpke SS, Oparil S, Thompson JA. Estrogen attenuates integrin-β3–dependent adventitial fibroblast migration after inhibition of osteopontin production in vascular smooth muscle cells. Circulation. 2000 Jun 27;101(25):2949-55.

[344] Li L, Couse TL, DeLeon H, Xu CP, Wilcox JN, Chaikof EL. Regulation of syndecan-4 expression with mechanical stress during the development of angioplasty-induced intimal thickening. Journal of vascular surgery. 2002 Aug 1;36(2):361-70.

[345] Gerasimovskaya EV, Tucker DA, Stenmark KR. Activation of phosphatidylinositol 3-kinase, Akt, and mammalian target of rapamycin is necessary for hypoxia-induced pulmonary artery adventitial fibroblast proliferation. Journal of Applied Physiology. 2005 Feb;98(2):722-31.

[346] Dupont S, Morsut L, Aragona M, Enzo E, Giulitti S, Cordenonsi M, Zanconato F, Le Digabel J, Forcato M, Bicciato S, Elvassore N. Role of YAP/TAZ in mechanotransduction. Nature. 2011 Jun;474(7350):179-83.

[347] Schulze-Bauer CA, Regitnig P, Holzapfel GA. Mechanics of the human femoral adventitia including the high-pressure response. American Journal of Physiology-Heart and Circulatory Physiology. 2002 Jun 1;282(6):H2427-40.

[348] Chai X, Sun D, Han Q, Yi L, Wu Y, Liu X. Hypoxia induces pulmonary arterial fibroblast proliferation, migration, differentiation and vascular remodeling via the PI3K/Akt/p70S6K signaling pathway. International journal of molecular medicine. 2018 May 1;41(5):2461-72.

[349] Brasier AR. The nuclear factor-κB–interleukin-6 signalling pathway mediating vascular inflammation. Cardiovascular research. 2010 May 1;86(2):211-8.

[350] Hemnes AR, Humbert M. Pathobiology of pulmonary arterial hypertension: understanding the roads less travelled. European Respiratory Review. 2017 Dec 31;26(146).

[351] Bertero T, Handen AL, Chan SY. Factors associated with heritable pulmonary arterial hypertension exert convergent actions on the miR-130/301-vascular matrix feedback loop. International journal of molecular sciences. 2018 Aug;19(8):2289.

[352] Liu X, Kelm Jr RJ, Strauch AR. Transforming growth factor β1-mediated activation of the smooth muscle α-actin gene in human pulmonary myofibroblasts is inhibited by tumor necrosis factor-α via mitogen-activated protein kinase kinase 1-dependent induction of the Egr-1 transcriptional repressor. Molecular biology of the cell. 2009 Apr 15;20(8):2174-85.

[353] Scott RA, Kharkar PM, Kiick KL, Akins RE. Aortic adventitial fibroblast sensitivity to mitogen activated protein kinase inhibitors depends on substrate stiffness. Biomaterials. 2017 Aug 1;137:1-0.

[354] Zhang L, Li Y, Liu Y, Wang X, Chen M, Xing Y, Zhu D. STAT3-mediated MMP-2 expression is required for 15-HETE-induced vascular adventitial fibroblast migration. The Journal of steroid biochemistry and molecular biology. 2015 May 1;149:106-17.

[355] Chen WD, Chu YF, Liu JJ, Hong MN, Gao PJ. RhoA-Rho kinase signaling pathway mediates adventitial fibroblasts differentiation to myofibroblasts induced by TGF-β1. Sheng li xue bao:[Acta physiologica Sinica]. 2013 Apr 1;65(2):113-21.

[356] Robinson KG, Nie T, Baldwin AD, Yang EC, Kiick KL, Akins Jr RE. Differential effects of substrate modulus on human vascular endothelial, smooth muscle, and fibroblastic cells. Journal of biomedical materials research Part A. 2012 May;100(5):1356-67.

[357] Eul B, Rose F, Krick S, Savai R, Goyal P, Klepetko W, Grimminger F, Weissmann N, Seeger W, Hänze J. Impact of HIF‐1α and HIF‐2α on proliferation and migration of human pulmonary artery fibroblasts in hypoxia. The FASEB journal. 2006 Jan;20(1):163-5.

[358] Welsh DJ, Scott PH, Peacock AJ. p38 MAP kinase isoform activity and cell cycle regulators in the proliferative response of pulmonary and systemic artery fibroblasts to acute hypoxia. Pulmonary pharmacology & therapeutics. 2006 Apr 1;19(2):128-38.

[359] Frisdal E, Gest V, Vieillard-Baron A, Levame M, Lepetit H, Eddahibi S, Lafuma C, Harf A, Adnot S, d'Ortho P. Gelatinase expression in pulmonary arteries during experimental pulmonary hypertension. European Respiratory Journal. 2001 Nov 1;18(5):838-45.

[360] Krick S, Hänze J, Eul B, Savai R, Seay U, Grimminger F, Lohmeyer J, Klepetko W, Seeger W, Rose F. Hypoxia‐driven proliferation of human pulmonary artery fibroblasts: cross‐talk between HIF‐1α and an autocrine angiotensin system. The FASEB journal. 2005 May;19(7):1-26.

[361] Mallawaarachchi CM, Weissberg PL, Siow RC. Antagonism of platelet‐derived growth factor by perivascular gene transfer attenuates adventitial cell migration after vascular injury: new tricks for old dogs?. The FASEB journal. 2006 Aug;20(10):1686-8.

[362] Sauvage M, Hinglais N, Mandet C, Badier C, Deslandes F, Michel JB, Jacob MP. Localization of elastin mRNA and TGF-β1 in rat aorta and caudal artery as a function of age. Cell and tissue research. 1998 Jan;291(2):305-14.

[363] An SJ, Liu P, Shao TM, Wang ZJ, Lu HG, Jiao Z, Li X, Fu JQ. Characterization and functions of vascular adventitial fibroblast subpopulations. Cellular Physiology and Biochemistry. 2015;35(3):1137-50.

[364] Haurani MJ, Cifuentes ME, Shepard AD, Pagano PJ. Nox4 oxidase overexpression specifically decreases endogenous Nox4 mRNA and inhibits angiotensin II–induced adventitial myofibroblast migration. Hypertension. 2008 Jul 1;52(1):143-9.

[365] Smith JD, Bryant SR, Couper LL, Vary CP, Gotwals PJ, Koteliansky VE, Lindner V. Soluble transforming growth factor-β type II receptor inhibits negative remodeling, fibroblast transdifferentiation, and intimal lesion formation but not endothelial growth. Circulation research. 1999 May 28;84(10):1212-22.

[366] Zhang L, Li Y, Chen M, Su X, Yi D, Lu P, Zhu D. 15‐LO/15‐HETE Mediated Vascular Adventitia Fibrosis via p38 MAPK‐Dependent TGF‐β. Journal of cellular physiology. 2014 Feb;229(2):245-57.

[367] He Y, Xiao Y, Yang X, Li Y, Wang B, Yao F, Shang C, Jin Z, Wang W, Lin R. SIRT6 inhibits TNF-α-induced inflammation of vascular adventitial fibroblasts through ROS and Akt signaling pathway. Experimental cell research. 2017 Aug 1;357(1):88-97.

[368] Zhang L, Chen Y, Li G, Chen M, Huang W, Liu Y, Li Y. TGF-β1/FGF-2 signaling mediates the 15-HETE-induced differentiation of adventitial fibroblasts into myofibroblasts. Lipids in health and disease. 2016 Dec;15(1):1-8.

[369] Li S, Tabar SS, Malec V, Eul BG, Klepetko W, Weissmann N, Grimminger F, Seeger W, Rose F, Hänze J. NOX4 regulates ROS levels under normoxic and hypoxic conditions, triggers proliferation, and inhibits apoptosis in pulmonary artery adventitial fibroblasts. Antioxidants & redox signaling. 2008 Oct 1;10(10):1687-98.

[370] Nave AH, Mižíková I, Niess G, Steenbock H, Reichenberger F, Talavera ML, Veit F, Herold S, Mayer K, Vadász I, Weissmann N. Lysyl oxidases play a causal role in vascular remodeling in clinical and experimental pulmonary arterial hypertension. Arteriosclerosis, thrombosis, and vascular biology. 2014 Jul;34(7):1446-58.

[371] Marino S, Hogue IB, Ray CJ, Kirschner DE. A methodology for performing global uncertainty and sensitivity analysis in systems biology. Journal of theoretical biology. 2008 Sep 7;254(1):178-96.

[372] Cohen TS, Gray Lawrence G, Khasgiwala A, Margulies SS. MAPK activation modulates permeability of isolated rat alveolar epithelial cell monolayers following cyclic stretch. PloS one. 2010 Apr 28;5(4):e10385.

[373] Cuenda A, Rouse J, Doza YN, Meier R, Cohen P, Gallagher TF, Young PR, Lee JC. SB 203580 is a specific inhibitor of a MAP kinase homologue which is stimulated by cellular stresses and interleukin-1. FEBS letters. 1995 May 8;364(2):229-33.

[374] Sun W, Chan SY. Pulmonary arterial stiffness: an early and pervasive driver of pulmonary arterial hypertension. Frontiers in medicine. 2018 Jul 18;5:204.

[375] Dieffenbach PB, Maracle M, Tschumperlin DJ, Fredenburgh LE. Mechanobiological feedback in pulmonary vascular disease. Frontiers in physiology. 2018 Jul 25;9:951.

[376] Dieffenbach PB, Haeger CM, Coronata AM, Choi KM, Varelas X, Tschumperlin DJ, Fredenburgh LE. Arterial stiffness induces remodeling phenotypes in pulmonary artery smooth muscle cells via YAP/TAZ-mediated repression of cyclooxygenase-2. American Journal of Physiology-Lung Cellular and Molecular Physiology. 2017 Sep 1;313(3):L628-47.

[377] Kolpakov V, Rekhter MD, Gordon D, Wang WH, Kulik TJ. Effect of mechanical forces on growth and matrix protein synthesis in the in vitro pulmonary artery: analysis of the role of individual cell types. Circulation research. 1995 Oct 1;77(4):823-31.

[378] Scott NA, Cipolla GD, Ross CE, Dunn B, Martin FH, Simonet L, Wilcox JN. Identification of a potential role for the adventitia in vascular lesion formation after balloon overstretch injury of porcine coronary arteries. Circulation. 1996 Jun 15;93(12):2178-87.

[379] Wang A, Cao S, Aboelkassem Y, Valdez-Jasso D. Quantification of uncertainty in a new network model of pulmonary arterial adventitial fibroblast pro-fibrotic signalling. Philosophical Transactions of the Royal Society A. 2020 Jun 12;378(2173):20190338.

[380] Liu F, Haeger CM, Dieffenbach PB, Sicard D, Chrobak I, Coronata AM, Velandia MM, Vitali S, Colas RA, Norris PC, Marinković A. Distal vessel stiffening is an early and pivotal mechanobiological regulator of vascular remodeling and pulmonary hypertension. JCI insight. 2016 Jun 2;1(8).

[381] Tse JR, Engler AJ. Preparation of hydrogel substrates with tunable mechanical properties. Current protocols in cell biology. 2010 Jun;47(1):10-6.

[382] Simmons CS, Ribeiro AJ, Pruitt BL. Formation of composite polyacrylamide and silicone substrates for independent control of stiffness and strain. Lab on a Chip. 2013;13(4):646-9.

[383] Kim DK, Huh JE, Lee SH, Hong KP, Park JE, Seo JD, Lee WR. Angiotensin II stimulates proliferation of adventitial fibroblasts cultured from rat aortic explants. Journal of Korean medical science. 1999 Oct 1;14(5):487-96.

[384] Rakugi H, Jacob HJ, Krieger JE, Ingelfinger JR, Pratt RE. Vascular injury induces angiotensinogen gene expression in the media and neointima. Circulation. 1993 Jan;87(1):283-90.

[385] Blatti SP, Foster DN, Ranganathan G, Moses HL, Getz MJ. Induction of fibronectin gene transcription and mRNA is a primary response to growth-factor stimulation of AKR-2B cells. Proceedings of the National Academy of Sciences. 1988 Feb 1;85(4):1119-23.

[386] Liu S, Parameswaran H, Young SM, Varisco BM. JNK suppresses pulmonary fibroblast elastogenesis during alveolar development. Respiratory research. 2014 Dec;15(1):1-1.

[387] Layland JO, Young IS, Altringham JD. The effect of cycle frequency on the power output of rat papillary muscles in vitro. The Journal of experimental biology. 1995 Apr;198(4):1035-43.

[388] Froese AR, Shimbori C, Bellaye PS, Inman M, Obex S, Fatima S, Jenkins G, Gauldie J, Ask K, Kolb M. Stretch-induced activation of transforming growth factor-β1 in pulmonary fibrosis. American journal of respiratory and critical care medicine. 2016 Jul 1;194(1):84-96.

[389] Lee AA, Dillmann WH, McCulloch AD, Villarreal FJ. Angiotensin II stimulates the autocrine production of transforming growth factor-β1 in adult rat cardiac fibroblasts. Journal of molecular and cellular cardiology. 1995 Oct 1;27(10):2347-57.

[390] Fisher SA, Absher MA. Norepinephrine and ANG II stimulate secretion of TGF-beta by neonatal rat cardiac fibroblasts in vitro. American Journal of Physiology-Cell Physiology. 1995 Apr 1;268(4):C910-7.

[391] Galie PA, Russell MW, Westfall MV, Stegemann JP. Interstitial fluid flow and cyclic strain differentially regulate cardiac fibroblast activation via AT1R and TGF-β1. Experimental cell research. 2012 Jan 1;318(1):75-84.

[392] Hamzeh MT, Sridhara R, Alexander LD. Cyclic stretch-induced TGF-β1 and fibronectin expression is mediated by β1-integrin through c-Src-and STAT3-dependent pathways in renal epithelial cells. American Journal of Physiology-Renal Physiology. 2015 Mar 1;308(5):F425-36.

[393] Shimano H, Sato R. SREBP-regulated lipid metabolism: convergent physiology—divergent pathophysiology. Nature Reviews Endocrinology. 2017 Dec;13(12):710-30.

[394] Wang X, Berry E, Hernandez-Anzaldo S, Takawale A, Kassiri Z, Fernandez-Patron C. Matrix Metalloproteinase-2 Mediates a Mechanism of Metabolic Cardioprotection Consisting of Negative Regulation of the Sterol Regulatory Element–Binding Protein-2/3-Hydroxy-3-Methylglutaryl-CoA Reductase Pathway in the Heart. Hypertension. 2015 Apr;65(4):882-8.

[395] Han H, Cho JW, Lee S, Yun A, Kim H, Bae D, Yang S, Kim CY, Lee M, Kim E, Lee S. TRRUST v2: an expanded reference database of human and mouse transcriptional regulatory interactions. Nucleic acids research. 2018 Jan 4;46(D1):D380-6.

[396] Wang J, Xu N, Feng X, Hou N, Zhang J, Cheng X, Chen Y, Zhang Y, Yang X. Targeted disruption of Smad4 in cardiomyocytes results in cardiac hypertrophy and heart failure. Circulation research. 2005 Oct 14;97(8):821-8.

[397] Umbarkar P, Singh AP, Gupte M, Verma VK, Galindo CL, Guo Y, Zhang Q, McNamara JW, Force T, Lal H. Cardiomyocyte SMAD4-dependent TGF-β signaling is essential to maintain adult heart homeostasis. JACC: Basic to Translational Science. 2019 Feb 1;4(1):41-53.

[398] Jankowski M, Broderick TL, Gutkowska J. The Role of oxytocin in cardiovascular protection. Frontiers in Psychology. 2020;11.

[399] Menaouar A, Florian M, Wang D, Danalache B, Jankowski M, Gutkowska J. Anti-hypertrophic effects of oxytocin in rat ventricular myocytes. International journal of cardiology. 2014 Jul 15;175(1):38-49.

[400] Sysa-Shah P, Xu Y, Guo X, Belmonte F, Kang B, Bedja D, Pin S, Tsuchiya N, Gabrielson K. Cardiac-specific over-expression of epidermal growth factor receptor 2 (ErbB2) induces pro-survival pathways and hypertrophic cardiomyopathy in mice. 2012 : e42805.

[401] Sanchez-Soria P, Camenisch TD. ErbB signaling in cardiac development and disease. InSeminars in cell & developmental biology 2010 Dec 1 (Vol. 21, No. 9, pp. 929-935). Academic Press.

[402] Souders CA, Borg TK, Banerjee I, Baudino TA. Pressure overload induces early morphological changes in the heart. The American journal of pathology. 2012 Oct 1;181(4):1226-35.

[403] Chen Y, Luo HQ, Sun LL, Xu MT, Yu J, Liu LL, Zhang JY, Wang YQ, Wang HX, Bao XF, Meng GL. Dihydromyricetin attenuates myocardial hypertrophy induced by transverse aortic constriction via oxidative stress inhibition and SIRT3 pathway enhancement. International journal of molecular sciences. 2018 Sep;19(9):2592.

[404] Richards DA, Aronovitz MJ, Calamaras TD, Tam K, Martin GL, Liu P, Bowditch HK, Zhang P, Huggins GS, Blanton RM. Distinct phenotypes induced by three degrees of transverse aortic constriction in mice. Scientific reports. 2019 Apr 10;9(1):1-5.

[405] Furihata T, Kinugawa S, Takada S, Fukushima A, Takahashi M, Homma T, Masaki Y, Tsuda M, Matsumoto J, Mizushima W, Matsushima S. The experimental model of transition from compensated cardiac hypertrophy to failure created by transverse aortic constriction in mice. IJC Heart & Vasculature. 2016 Jun 1;11:24-8.

[406] Meems LM, Cannon MV, Mahmud H, Voors AA, van Gilst WH, Silljé HH, Ruifrok WP, de Boer RA. The vitamin D receptor activator paricalcitol prevents fibrosis and diastolic

dysfunction in a murine model of pressure overload. The Journal of steroid biochemistry and molecular biology. 2012 Nov 1;132(3-5):282-9.

[407] Nakamura A, Rokosh DG, Paccanaro M, Yee RR, Simpson PC, Grossman W, Foster E. LV systolic performance improves with development of hypertrophy after transverse aortic constriction in mice. American Journal of Physiology-Heart and Circulatory Physiology. 2001 Sep 1;281(3):H1104-12.

[408] Melenovsky V. Cardiac adaptation to volume overload. InCardiac adaptations 2013 (pp. 167-199). Springer, New York, NY.

[409] Toischer K, Zhu W, Hünlich M, Mohamed BA, Khadjeh S, Reuter SP, Schäfer K, Ramanujam D, Engelhardt S, Field LJ, Hasenfuss G. Cardiomyocyte proliferation prevents failure in pressure overload but not volume overload. The Journal of clinical investigation. 2017 Dec 1;127(12):4285-96.